UNIVERSIDAD DE CHILE
FACULTAD DE CIENCIAS FÍSICAS Y MATEMÁTICAS
DEPARTAMENTO DE INGENIERÍA ELÉCTRICA

DESIGN, SIMULATION AND COMPARISON OF TWO ULTRA-WIDEBAND DUAL-POL COMPACT HETERODYNE FRONT END PIXELS

TESIS PARA OPTAR AL GRADO DE MAGISTER EN CIENCIAS DE LA INGENIERÍA, MENCIÓN ELÉCTRICA

MEMORIA PARA OPTAR AL TÍTULO DE INGENIERO CIVIL ELÉCTRICO

CAMILO JOSÉ SALDAÑA ESPINOZA

PROFESOR GUÍA:
RICARDO ALBERTO FINGER CAMUS

MIEMBROS DE LA COMISIÓN:
FAUSTO PATRICIO MENA MENA
RODRIGO ANDRÉS REEVES DÍAZ

Este trabajo ha sido parcialmente financiado por la Comisión Nacional de Investigación Científica y Tecnológica (CONICYT-ANID) a través de sus fondos Basal AFB-170002 y ALMA 31180005

SANTIAGO DE CHILE
2021

RESUMEN DE LA MEMORIA PARA OPTAR
AL TÍTULO DE MAGÍSTER EN CIENCIAS DE LA INGENIERÍA, MENCIÓN ELÉCTRICA
POR: CAMILO JOSÉ SALDAÑA ESPINOZA
FECHA: 2021
PROF. GUÍA: RICARDO ALBERTO FINGER CAMUS

DESIGN, SIMULATION AND COMPARISON OF TWO ULTRA-WIDEBAND DUAL-POL COMPACT HETERODYNE FRONT END PIXELS

Los arreglos de plano focal heterodinos han adquirido importancia para observaciones astronómicas dada su alta sensibilidad, resolución espectral y gran campo de visión. No obstante, los módulos que componen estos arreglos requieren una complicada y costosa construcción. Normalmente no contienen un dispositivo de análisis polarimétrico, llamado transductor ortomodal (OMT), debido a su estructura en guía de ondas difícil de integrar y de amplia sección. En este trabajo, se diseñan, simulan y comparan dos pixeles de *Front End* compuestos por un OMT planar y mezcladores IQ para frecuencias entre 67 - 116 GHz. Se propone realizar recombinación de señales por polarización y calibración de polarización cruzada en el *Back End* del instrumento. Se considera operar mezcladores MMIC a temperatura ambiente para simplificar el proceso de caracterización. En la banda de frecuencias, ambos diseños ofrecen pérdidas por reflexiones <-20 dB, transmisiones de polarización cruzada <-45 dB y aislación <-50 dB, además de reducir al 51.4% el tamaño de un OMT de guía de ondas para las mismas frecuencias. La comparación entre diseños muestra un intercambio entre rendimiento y complejidad mecánica del instrumento. Ambos receptores diseñados son aptos para desarrollar arreglos de plano focal heterodinos de simple fabricación considerando rendimiento y compactación simulados.

Abstract

Heterodyne focal-plane array receivers are of growing importance in astronomical observations as they offer high-sensitivity, and high-resolution spectroscopy with a broad field of view. However, the single-pixel modules that build up these arrays are expensive and difficult to build. Normally they do not contain a polarimetry analysis device, called orthomodal transducer (OMT), since the OMTs are difficult-to-integrate waveguide structures with large footprints. In this work, two front end pixels, composed of planar OMTs and MMIC IQ mixers are designed, simulated, and compared for the 67 – 116 GHz frequency band. Signal recombination per polarization and cross-polar calibration are proposed to be performed by the Back End of the instrument. Room-temperature-operating MMIC mixers are considered to simplify the characterization process. Over the entire frequency band, both designs offer the required reflection-losses <-20 dB, cross-polarization transmissions <-45 dB and isolation <-50 dB, in addition to reducing to 51.4% the size of a waveguide OMT for the same frequency band. The comparison between designs shows that there is a trade-off between performance and mechanical complexity of the instrument. The designed receivers are feasible for developing heterodyne focal plane arrays of simpler fabrication considering simulated compactness and performance.

To Raúl and Pistacho

Acknowledgements

In the first place I want to thank my mother, who gave me my life and all her caring and support to achieve my goals, academic or personal.

I am very thankful to have studied under the tutelage of my commission, composed by Ricardo Finger, Fausto P. Mena and David Monasterio. They were always open to sharing their knowledge and supporting my research in the most constructive way I could have expected. Thanks to Ignacio Barrueto, who provided the models of the OMT that served as the starting point for one version of the designed instruments of this thesis. Thanks to José Pizarro who helped me invision the way the designs I made could be fabricated and develop a mechanical plane for the studied receivers. Thanks to all the team of the MWL: Camilo, Catalina, both Daniel'es, David, Diana, Diego, Franco, Pablo, Rocío and Sebastián, all who shared a word of encouragement and advice along my research. Thank you all.

Thanks to my friends Francisco and Sebastian, whose research motivated me to do my best and always shared their wisdom with me, but most importantly their friendship.

Thanks to the people who were part of this process from the beginning or before. To Gianluca and Marco, friends since kids. To the swimming team of Universidad de Chile, especially to my coaches Álvaro, Cristián and Cristóbal who always believed in me. To my first year friends Daniela, Danilo, Diego, Maggi, Nacho and Pelao. To my friends from the electrical program Claudio, Constantino, Medivh, Pepper and René. To my former team and class mates Carlos, Felipe, José Ignacio and Joaquín. To you and many more.

This stage of my life would not be coming to an end without all the people that put a pebble on the road, one day at a time, and the opportunities they gave me.

This work was supported by the Chilean National Commission for Scientific and Technological Research (CONICYT-ANID) through its grants Basal AFB-170002 and ALMA 31180005.

Thank you so much.

Contents

List of Tables

List of Figures

Chapter 1

Background and Motivation

1.1 Introduction

The world's largest interferometer, the Atacama Large Millimeter/Submillimeter Array (ALMA), covers a broadband frequency spectrum. It observes every atmospheric window from 35 to 950 GHz, which are separated in ten frequency bands. All these frequency bands are implemented, except band 2 (67 - 90 GHz) which is under development [1]. Currently, different approaches are being developed to cover both bands 2 and 3 simultaneously (67 - 116 GHz, commonly referred to as band 2+3) in a collaboration of European institutes (ESO, INAF), Japanese (NAOJ) and Universidad de Chile (MWL). Among the technologies under development to cover band 2+3, components to perform polarimetry analyses are being designed; the design of these elements of an instrument motivate the research in this thesis.

A new generation of radio astronomy instruments to be developed require front end receivers to operate on a double polarization configuration. This configuration includes coherent detectors with unprecedented levels of sensibility and dynamic range [2]. One useful technique for this purpose is polarimetry, which is used in astronomy to observe different structures such as supernovae, interstellar medium dust, star formation or cosmic microwave background [3]. Polarimetry consists of analyzing elliptically polarized signals as a combination of orthogonal linear polarizations. The level of polarization of signals coming from the sky is characterized by the Stokes parameters. They relate the amplitude of the perpendicular components E_x and E_y of the received electric field [4]. The Stokes parameters characterize the ellipticity of the observed signal's polarization.

The polarimetric analysis is done by including a polarization splitter into the receiver, also called Ortho-Mode Transducer (OMT). It is connected right after the front end's horn antenna and before the low noise amplifier (LNA) or mixers of the receiver. Regarding its astronomical relevance, polarimetric analysis yields information about the source of a signal such as privileged directions of radiation due to magnetic fields. Additionally, by adding both linear polarizations after they are split, the signal to noise ratio is improved by the square root of two. This phenomena implies a reduction of the observation time to one half as compared to a non-polarimetric radio telescope [5].

An OMT can be implemented itself as a transition between transmission media, usually transitioning from a waveguide structure to other lines (e.g. microstrip or stripline). This way, amplifiers, mixers and/or ADCs can be directly connected in order to obtain signals and apply an arbitrary phase shift to perform digital aliasing correction by the means of digital sideband separating technique [6, 7]. Such correction is performed by a digital calibration of the analog imbalances [8].

The main problems with polarimetry analysis lie in the mechanical aspects of the OMT. At the frequencies of this study, this instrument usually consists of a metallic block comprising wave guides, type-T junctions, 90 and/or 180-degree bends and transitions between different shape of wave guides. Fabrication of an OMT requires the dedication of a technician for days in order to make one unit. A single unit is made of many pieces that need to match perfectly. Furthermore, this unit must be characterized. This process means a considerable cost in fabrication time and equipment. If the process needs to be iterated, costs increase even further. Additionally, waveguide OMTs have a large footprint and impede their implementation as a collection of identical blocks or pixels of a focal plane array, thus missing the possibility of making measurements at the standard required for modern astronomical observations [2, 9].

By simplifying the mechanical development of a waveguide OMT, two easily reproducible radio astronomy instruments are proposed in this thesis for the ALMA 2+3 band. The OMT and additional transitions are made up of planar structures, which reduce the overall size of the designed front ends. Therefore, planar OMTs are the main element of study of the proposed receivers. Two different designs of planar OMTs are studied and compared with the expectation to be competitive with reported OMTs, while having a simplified fabrication and reduced footprint. Implementation as digital OMTs is proposed as in [8] in order to simplify fabrication and to make the planar OMT performance competitive with other designs of a more complex structure.

1.2 Operation of an OMT

A micro wave OMT is a passive device made out of waveguides and other metallic structures. It splits the orthogonal polarizations of the incoming astronomical signal. Each polarization is split between two branches of waveguides or less commonly other transmission lines. OMTs can actually be implemented in microstrip but is not practical at millimeter wavelengths. Hence, the device contains 4 transmission lines plus the structures required in order to split the polarizations. Both branches of each polarization merge after the split, so that two signals are obtained, each containing the power of one polarization orthogonal to one another.

One of the main figures of merit of an OMT is its frequency bandwidth. It tells, to a large extent, the band at which it operates and also tells whether it is suitable for a radio astronomy application given its reflection losses level. How much power leaks from one polarization branch to the other, called cross-polarization, is the second figure of merit to consider for an OMT. Cross-polarization indicates the capacity of the OMT to discriminate or to truly split the orthogonal polarizations of the input signal. A third figure of merit is called isolation or cross-talk, which indicates how much power can be transferred from one recombinated polarization branch to the other. Isolation can be inferred from the cross-polarization level, since their electromagnetic meaning is similar, but not the same. A fourth figure of merit,

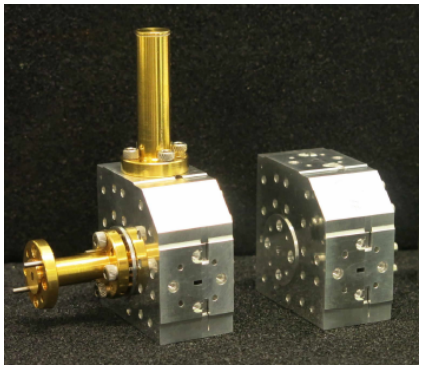

(a) Waveguide (platelet) [10].

(b) Waveguide [11].

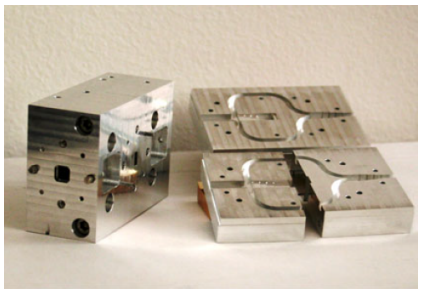

(c) Dual Ridge [12].

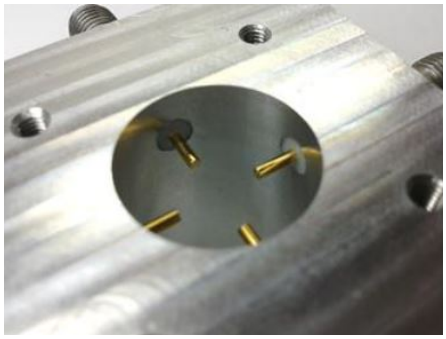

(d) Coaxial probes [8].

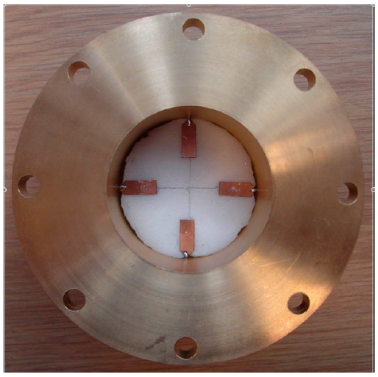

(e) Microstrip (planar) [13].

Figure 1.1: Illustration of different types of OMT. (a) A waveguide-based OMT, which is built by joining plates where the structures of the device are etched. (b) Another waveguide based OMT that contains a turnstile at the center of its main junction. Even though it is smaller than the OMT in 1.1a, fabrication is clearly complex due to the joints and bends. (c) A waveguide OMT whose separation of polarizations is carried out by a structure of ridges, which gives it the name of *Dual Ridge*. It accomplishes notable figures of merit at the cost of including complicated structures inside. (d) A design based on coaxial probes as a proof of concept for digital calibration of an OMT. (e) Photograph of a planar OMT, implemented and measured. It is built out of microstrip probes and transmission lines. It is called planar because the polarization split and guide exist in one plane and substrate, different to the previously shown OMTs.

OMT Type	Central Freq. [GHz]	%BW sim.	%BW meas.	Xpol sim. [dB]	Xpol meas. [dB]	Isol sim. [dB]	Isol meas. [dB]	Ref.
Coaxial probes	15.3	32.7	-	-40	-	-	-	[8]
Waveguide	24.5	20.4	20.4	-	-	-100	-	[14]
Waveguide	15.0	66.7	60.0	-	-45	-	-45	[15]
Waveguide	39.5	53.1	53.1	-60	-40	-60	-40	[16]
Waveguide	93.0	49.4	46.0	-75	-40	-80	-50	[10]
Waveguide	91.5	53.5	28.8	-45	-35	-52	-50	[17]
Waveguide	100.0	32.0	32.0	-	-30	-	-45	[18]
Waveguide	94.0	29.8	29.8	-	-	-	-	[19]
Waveguide	94.0	29.8	31.1	-	-30	-	-45	[20]
Waveguide	92.5	37.8	37.8	-	-	-	-40	[11]
Waveguide	31.0	17.1	17.1	-	-50	-	-60	[21]
Dual Ridge	95.0	44.2	44.2	-30	-30	-	-	[22]
Dual Ridge	39.0	46.1	37.8	-80	-50	-60	-60	[12]
Microstrip (planar)	153.0	35.2	-	-	-40	-	-30	[23]
Microstrip (planar)	5.4	14.8	17.8	-60	-55	-	-	[13]
Microstrip (planar)	144.0	26.3	-	-	-	-	-	[24]

Table 1.1: Comparative table of different designs of OMT, characterized by their polarization-separation strategy and figures of merit distinguished according to simulations and measurements. A box filled with a dash means that there are no reported results for that particular figure of merit.

rarely reported, is the co-polar transmission of power, which is the transmission of desired power and indicates how lossy an OMT is.

1.3 Designs of OMTs

Different types of OMT are reported in the literature and some are shown in figure 1.1. They can differ in the transmission lines used and the polarization-split strategy. In table 1.1 their figures of merit are compared. The type of the OMT refers to the main structures that make it. Central frequency (Freq.) gives an idea of the operation band of the device. Frequency bandwidth (%BW) is considered for a continuous frequency band with reflection losses equal or better than -20 dB. Cross-polarization levels (Xpol) are included, as well as isolation (Isol.) between output ports of the OMTs. Figures of merit are reported for simulations (sim.) and measurements (meas.) whenever data is available. Note that not all the cited works report the same figures of merit.

Most of the designs reported in table 1.1 are waveguide-based. Two examples are shown in figure 1.1a and 1.1b. The *platelet* term refers to the technique of joining plates in order to build the OMT. Polarization split is done by a structure at the center of the OMT called *turnstile*. Note that the overall structure is considerably bigger than the flange of the waveguide, which serves as a reference for its size. The dual ridge OMT of figure 1.1c is also waveguide-based but includes even more complicated to manufacture structures inside. All the previously mentioned strategies imply an electrically large component and of complex fabrication, which makes them unlikely to be implemented as part of a pixel for a focal plane array.

Regarding focal plane arrays, the separation between its pixels determines the width of the array's beam. Beamwidths of each individual pixel should cover half the array's beamwidth.

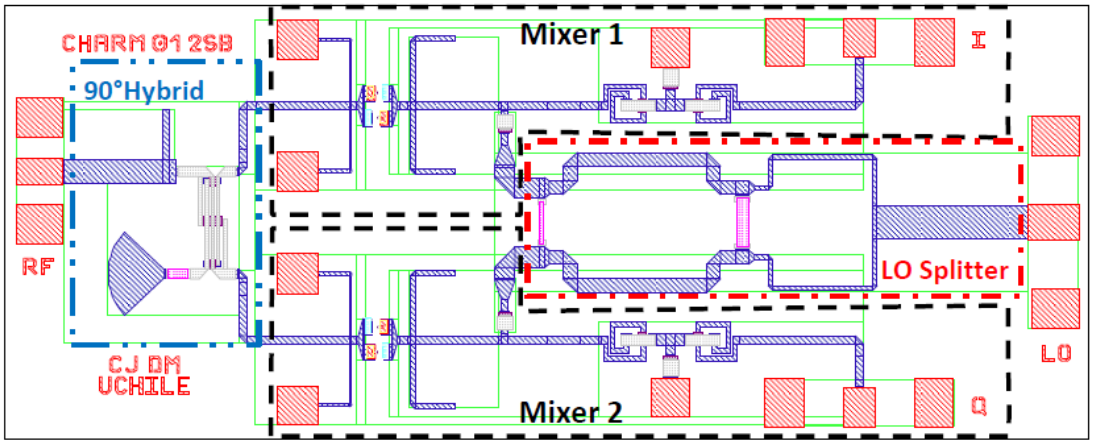

(a) Layout of the considered MMIC mixer for this work, being developed in [25].

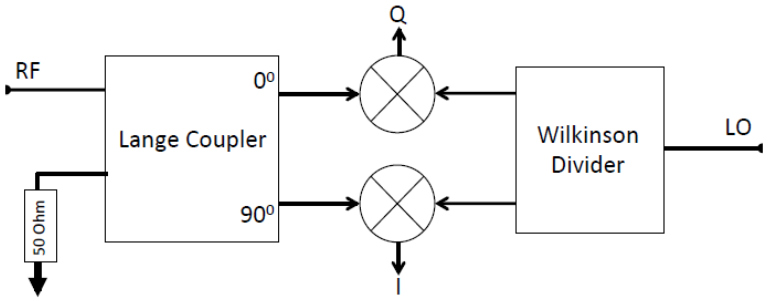

(b) Topology of the considered MMIC, studied first in [26].

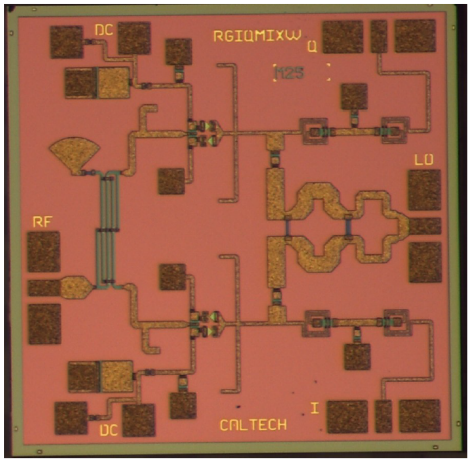

(c) Photograph of a manufactured MMIC mixer in [26].

Figure 1.2: Layout of the considered MMIC for this work, and topology and photograph of previously reported MMIC mixers.

This way, sampling at half beamwidth is achieved by design and the focal plane array observes the sky with full Nyquist performance. This feature of the array is achieved by placing its pixels near each other. In the case of the array reported in [9], only a few wavelengths of the central frequency of the band separate each pixel. None of the OMT designs from figures 1.1a, 1.1b and 1.1c, satisfy the conditions to be included into a focal plane array. This is due to the section of the component, in the case of the OMT from 1.1a, and because all of them have output waveguides parallel to the focal plane. This would inevitably separate them by a considerable margin due to mechanical constraints if they would be implemented as pixels of an array.

Additionally to the waveguide OMT designs, there are reported OMTs based directly on media transitions, which are the coaxial and planar designs. Both the coaxial and planar OMTs (figures 1.1d and 1.1e respectively) perform the coupling of the orthogonal polarizations via probes. This appears as a solution to reduce the footprint of the OMT, especially in the case of the microstrip-based OMT. Furthermore, if the OMT is implemented as the digitally-aided-OMT in [8], recombination of signals of each polarization is performed at the Back End of the receiver and the footprint could be reduced even further.

However, there are differences between the reported planar OMTs and those proposed in this work. The differences lie in the frequency bands they cover and the considered electronics. The widest fractional bandwidth among the reported planar OMTs is of 37%. To completely cover the 2+3 band of ALMA implies a bandwidth of 53%. There are only three reported OMTs from table 1.1 that have a fractional bandwidth of more than 50%. As compared to reported designs, operation at this frequency band implies the use of bigger waveguides for reception of the signal than in [23] and [24]. Regarding the planar structures, a thicker substrate to support the microstrip lines would be also required, or of smaller dielectric constant. These conditions modify the overall design of the OMT as compared to the reported planar designs [23, 13, 24].

The OMT in [24] considers the use of cryogenic-operating SIS mixers, which is also different to the proposal of this research. The considered Monolithic Microwave Integrated Circuits (MMIC) mixers are operated at room temperature to ease, accelerate and reduce costs of the characterization process of the designed OMTs. However, to operate in a future stage as part of a competitive radio astronomy receiver, all the analog electronics must be operated in cryogenics. An additional difference between the proposed OMT designs in this work and the OMT in [24] is related to the signal recombination per polarization. The reported OMT recombines the signals from each polarization in the same PCB that contains the OMT, which is achieved by using a multi-layer substrate. Such property is neglected in this research. Since the OMTs to be designed in this work are proposed to be implemented as digital OMTs, the recombination of signals is done off-board [8].

1.4 Heterodyne Mixers Suitable for this Work

The MMIC mixers considered for this work are under development [25]. This MMIC consists of a 90 degree hybrid at its input, two heterodyne mixers at each output of such hybrid and a Wilkinson divider to feed both mixers from a single local oscillator (LO) input. By having two heterodyne mixers whose outputs are phase shifted in 90 degrees, called I and Q signals,

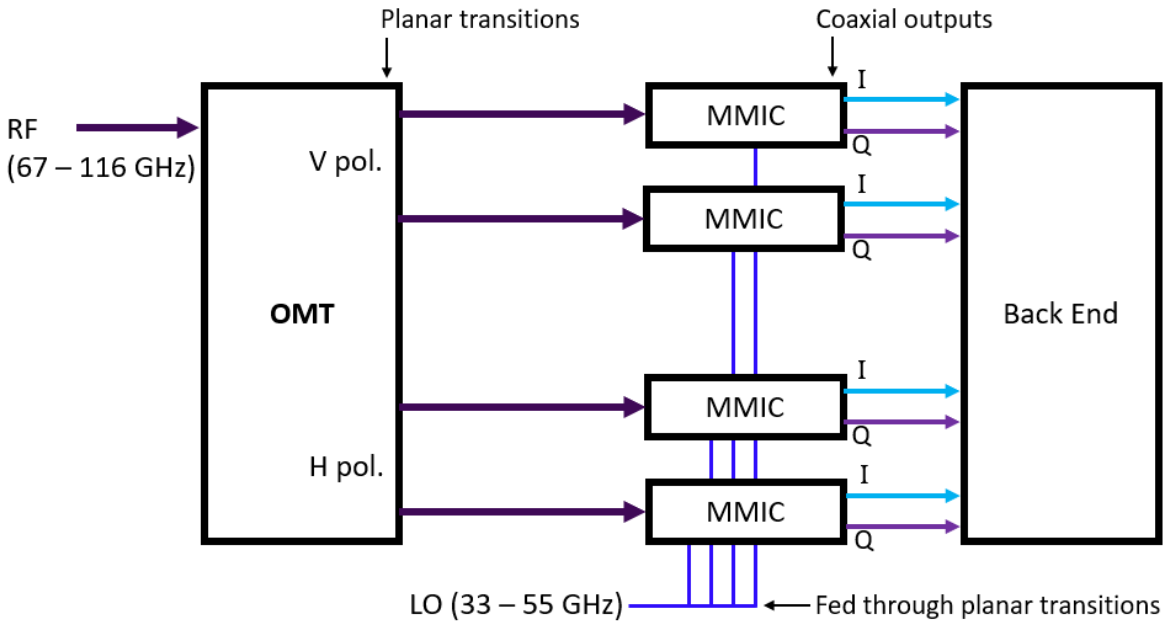

Figure 1.3: Block diagram of the proposed front ends' architecture.

image rejection can be performed at the back end of the receiver [6, 7]. These MMIC mixers are chosen for this design since this proposal consists of digitally implementing an OMT as in [8]. The considered MMIC mixers can be operated at room temperature, which eases the characterization of the instrument that integrates it before operating it for radio astronomy. The layout of the considered MMIC mixers is shown in figure 1.2a. This MMIC follows a topology already studied in [26]. The topology of these MMICs is shown in figure 1.2b and a photograph of a manufactured MMIC mixer following this topology is shown in figure 1.2c.

In the OMT designs to be developed in this work, cavities must be left to place and hold the considered MMIC mixers. The dimensions of such cavities are designed to hold the MMIC mixer of figure 1.2a. However, it is important to point out that in a future iteration of this work, such cavities could hold different electronics. For instance, an integrated circuit containing a low noise amplifier (LNA) should be considered for a final version of this instrument, or even SIS electronics.

1.5 General Problem

The general problem to be solved in this project is to simplify construction and reduce size of an OMT-containing-front-end. It must be small and simple enough to be used as a pixel for a focal plane array. Thus, a novel approach to develop the Front End for a polarimetric radio astronomy receiver is proposed for the 67 - 116 GHz, corresponding to the bandwidth covered by the original ALMA bands 2 and 3 simultaneously.

A block diagram showing the architecture of the proposal to solve the general problem is shown in figure 1.3. Simplification of manufacturing and footprint reduction of the OMT is solved through the design of transitions from waveguide to microstrip, using planar probes to make up the OMT. MMIC mixers are connected to these transitions, which perform

heterodyne down conversion and yield two output signals (I/Q) each. The considered MMIC mixers follow the topology shown in figure 1.2b. Integrated electronics operate at room temperature, easing the characterization of the device before its cryogenic operation as a radio astronomy receiver.

Interface to the back end of the receiver is designed via coaxial connectors. In this proposal, the signal recombination per polarization is left to the back end so that the analog electronics are simplified. Image rejection is performed in the back end by retrieving the mixers' I/Q signals, also improving the figures of merit of cross-polarization and isolation of the OMT [7].

1.6 Objectives

1.6.1 General Objective

To design, simulate and compare two front ends for polarimetry analysis. Front ends must contain an OMT, as the main component, and local oscillator (LO) splitters and transitions to feed sub-harmonic mixers. Level of success of each design is quantified by the following figures of merit, evaluated across the 67 - 116 GHz frequency band or ALMA 2+3 Band. They are sorted in descending order according to its relevance:

1. Reflection losses $<$ -20 dB over the entire frequency band.
2. Cross-polarization transmissions $<$ -40 dB.
3. Isolation between polarization ports $<$ -40 dB.
4. Insertion gain $>$ -2 dB.

Digital recombination is also simulated by post processing the simulation results previously obtained.

1.6.2 Specific Objectives

- Study transitions from waveguide to microstrip transmission lines.
- Design of OMTs and PCBs to integrate MMIC mixers.
- Design of a splitter for local oscillator plus a transition to microstrip to feed the MMIC mixers.
- Design of mechanical blocks that would shape and contain the structures conforming the receivers, for a future fabrication.
- Compare both designs according to their electromagnetic figures of merit.
- Compare both designs according to their mechanical constraints, size of footprint, costs of fabrication and error tolerance.

1.7 Hypothesis

- Designed mechanical pieces and structures can be fabricated in the Millimeter Wave Laboratory of Universidad de Chile. Designs are made considering the resolution of

the fabrication equipment given by their manufacturers.

- Planar probes and antennas allow the implementation of transitions with a fractional bandwidth of 53%, the required to cover ALMA band 2+3.
- Digital integration of the planar OMT makes it competitive with other designs of OMTs, which have a more complex and expensive fabrication.
- Compactness or size reduction of the OMT by using planar structures is enough to implement it as a pixel for a focal plane array.

1.8 Thesis Outline

This thesis began with an explanation of the motivations and the context in which this research is carried out. The following chapters are:

- **Literature Review**: This chapter summarizes he theoretical concepts useful to understand the work of this thesis.
- **Methodology**: An explanation of the tasks developed along this work following a chronological order.
- **Planar Version of OMT and Front End**: The design and results of the first version of the OMT and front end are presented in this chapter. This version is referred to as Planar Version (PV). Observations on its performance and mechanical design motivate the design of a second version of the front end.
- **Semi-Turnstile Version of OMT and Front End**: The second version of OMT and Front End is studied in this chapter.
- **Analysis of Results**: The results of the Planar and Semi-Turnstile OMTs are further studied through post-processing of the simulation data. The cross-polarization of the OMTs, their isolation between output ports and the current distribution on their microstrip probes are analyzed. The fabrication tolerance analysis is also addressed.
- **Comparison of Results**: Electromagnetic results are compared according to the main figures of merit of the OMTs and local oscillator splitters. The mechanical aspects of the Alpha and Beta designs are also compared in a more qualitative manner.
- **Conclusion**: A final word is given about all the previously stated topics of this research, summarizing remarkable results and indicating the guidelines that future work should follow after this study.

Chapter 2

Literature Review

In this chapter, the theoretical background needed to understand the operation of the designed components in this thesis is presented. Related electromagnetic phenomena are reviewed as well. First, the scattering matrix and electromagnetic wave theory is studied. Polarization of a wave is fundamental to understand the relevance of the implementation of an orthomode transducer (OMT), key element of this research. Since the developed designs use different transmission media, wave propagation in waveguides and microstrips is reviewed. Even though the proposed designs consist of planar OMTs, waveguides are inevitably used to accomplish certain functions in the receiver. Lastly, due to the broadband application that the components in this thesis are designed for, broadband antennas and related metamaterials principles are reviewed.

2.1 Scattering Matrix

The scattering matrix is a representation of an N-port network. The scattering matrix relates the incident voltage waves on the ports to those reflected from the ports. It provides a complete description of the network including implicitly the ideas of incident, reflected and transmitted waves for each of the network's ports. Figure 2.1 shows a graphic example of how the scattering matrix is defined for an arbitrary network [27].

The scattering matrix S is an array of S_{ij} parameters. Each element of the matrix is defined as a voltage ratio between the incident wave V^+ in port i and reflected wave V^- at port j, while incident waves are zero at all other ports. Thus, a specific element of the matrix [S] is determined as

$$S_{ij} = \left.\frac{V_i^-}{V_j^+}\right|_{V_k^+=0, k\neq j} \tag{2.1}$$

and the overall matrix has the form of

$$\begin{bmatrix} V_1^- \\ V_2^- \\ \vdots \\ V_n^- \end{bmatrix} = \begin{bmatrix} S_{11} & S_{12} & \cdots & S_{1n} \\ S_{21} & \ddots & & S_{2n} \\ \vdots & & \ddots & \vdots \\ S_{n1} & \cdots & \cdots & S_{nn} \end{bmatrix} \begin{bmatrix} V_1^+ \\ V_2^+ \\ \vdots \\ V_n^+ \end{bmatrix} \tag{2.2}$$

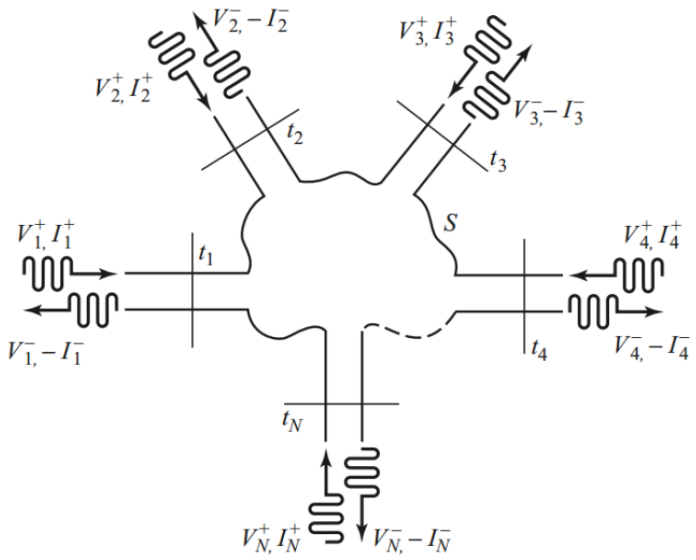

Figure 2.1: Scheme of an arbitrary N-port network. V_{i}^{+} stands for the magnitude of an incident wave at port i, while V_j^{-} is the magnitude of a reflected wave at port j (Source: *Microwave Engineering, David M. Pozar*).

or

$$[V^{-}] = [S][V^{+}] \tag{2.3}$$

Cases of particular importance are the elements of S_{ii} which represent the reflections at port i. Other important cases are those elements of form S_{j1}, where an input signal will usually come from port 1 to port j. The last example represents the transmission of a signal which, depending on the case, would be desirable to be either very low or very high.

2.2 Electromagnetic Waves

An electromagnetic wave is an oscillation, transporting energy and propagating through spacetime. James Clerk Maxwell first enunciated the behaviour of electromagnetic fields in twelve equations [28]. Oliver Heaviside reduced those equations what is nowadays Maxwell's equations [29]. The formulation disengages electrical and magnetic fields, characterizing the waves in terms of the fields. The formulation also considers the wave travelling through a linear, isotropic, and homogeneous region. In phasor form, the equations are

$$\nabla \times \vec{E}(\vec{r}) = -j\omega\vec{B}(\vec{r}) \tag{2.4}$$

$$\nabla \times \vec{H}(\vec{r}) = \vec{J}(\vec{r}) + j\omega\vec{D}(\vec{r}) \tag{2.5}$$

$$\nabla \cdot \vec{D}(\vec{r}) = \rho(\vec{r}) \tag{2.6}$$

$$\nabla \cdot \vec{B}(\vec{r}) = 0. \tag{2.7}$$

Phasor form is convenient because it assumes a monochromatic oscillation of the system, allowing phasorial analysis in terms of space. $\vec{E}$ is the electrical field, $\vec{B}$ is the magnetic field,

$\vec{H}$ is the magnetic field intensity, $\vec{J}$ is the electrical current density and ρ is the volumetric charge density. Source-free implies that $\rho(\vec{r}) = 0$, and lossless medium implies $\sigma = 0$, thus $\vec{J}(\vec{r}) = 0$. Therefore, under these assumptions, equations 2.4 and 2.5 reduce to

$$\nabla^2 \vec{E} + \omega^2 \mu\varepsilon \vec{E} = 0. \tag{2.8}$$

Equation 2.8 is the *wave equation* or *Helmholtz's equation*. An analogous equation can be obtained for $\vec{H}$

$$\nabla^2 \vec{H} + \omega^2 \mu\varepsilon \vec{H} = 0. \tag{2.9}$$

At this point it is convenient to define the constant $k = \omega\sqrt{\mu\varepsilon}$ called the *propagation constant of the medium*, also known as *wave number*. In free space, $k = k_0 = \omega\sqrt{\mu_0\varepsilon_0}$. Expanding rectangular components of the laplacian of equation 2.8, we obtain

$$\frac{\partial^2 \vec{E}}{\partial x^2} + \frac{\partial^2 \vec{E}}{\partial y^2} + \frac{\partial^2 \vec{E}}{\partial z^2} + k_0 \vec{E} = 0, \tag{2.10}$$

which is true for every rectangular component of $\vec{E}$. Therefore,

$$\frac{\partial^2 E_\mathrm{i}}{\partial x^2} + \frac{\partial^2 E_\mathrm{i}}{\partial y^2} + \frac{\partial^2 E_\mathrm{i}}{\partial z^2} + k_0 E_\mathrm{i} = 0 \tag{2.11}$$

where E_i is the magnitude of the electric field in either the x, y or z direction. Equation 2.11 is satisfied by a field propagation mode which is called the *Transerse Electromagnetic Mode* (TEM). It has the particularity of having no fields components in the direction of propagation: $\vec{E}$ is orthogonal to $\vec{H}$, and both are in turn orthogonal, to the direction of propagation ($\pm z$). Fields exist in a plane, and if there are geometrical places of uniform phase which are flat and parallel to each other, the wave is called a *plane wave*. If the fields are invariant in these planes of constant phase, the wave is called *uniform plane wave*.

A wave propagating in the z direction reduces equation 2.11 to

$$\frac{\partial^2 E_x}{\partial z^2} + k_0^2 = 0 \tag{2.12}$$

which is an homogeneous differential equation. It has two independent solutions, found by substitution, of the form

$$E_x(z) = E^+ \mathrm{e}^{-jkz} + E^- \mathrm{e}^{jkz}, \tag{2.13}$$

where E^+ and E^- are arbitrary amplitude constants of waves propagating in the $+z$ and $-z$ directions respectively. Equation 2.13 presents the expression for the electric field vector of a uniform plane wave propagating in the z axis.

2.3 Polarization of a wave

Polarization of a wave is defined as the shape performed by the tip of the electric field vector in time at a given point in space [30]. If it is a plane wave, it has no field component in the direction of propagation, while fields on perpendicular planes to the propagation direction change their orientation in time describing different shapes.

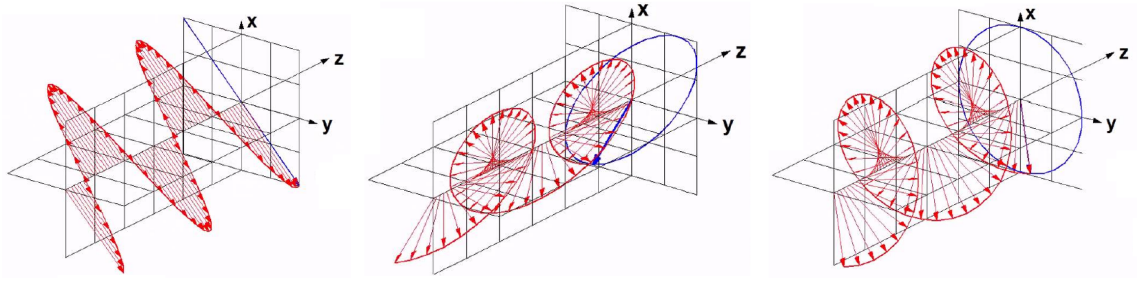

(a) Linear polarization. (b) Eliptical polarization. (c) Circular polarization.

Figure 2.2: Plane waves of different types of polarization propagating in space (*Source: Ms. C. Thesis, I. Barrueto*).

Without loss of generality, let us consider a wave propagating in the $+z$ direction. Mathematically, an arbitrary electromagnetic wave can always be expressed as a linear combination of two orthogonal waves. Considering its electric field, it has the form of

$$\vec{E} = E_{\parallel} \mathrm{e}^{-jkz} \hat{\mathrm{e}_{\parallel}} + E_{\perp} \mathrm{e}^{-jkz} \mathrm{e}^{-j\Delta\phi} \hat{\mathrm{e}_{\perp}}, \tag{2.14}$$

where perpendicular components have magnitudes of $E_{\parallel}$ and $E_{\perp}$, and maintain a phase offset of $\Delta\phi$. Polarization is determined by these three terms. Figure 2.2 shows different types of polarization [17].

If phase offset is zero or π, polarization is linear (figure 2.2a). If phase offset is different than zero, polarization is elliptical (figure 2.2b). A particular case is when $\Delta\phi = \pm\frac{\pi}{2}$ and $E_{\parallel} = E_{\perp}$, then polarization is circular (figure 2.2c). Sense of rotation is given by the sign of the offset $\Delta\phi$.

2.3.1 Polarization Ellipse

In equation 2.14, orthogonal components could be depicted in terms of x and y axis

$$\vec{E} = |E_x| \mathrm{e}^{j\theta_x} \hat{x} + |E_y| \mathrm{e}^{j\theta_y} \hat{y}. \tag{2.15}$$

However, in spite that components of the electric field might be misaligned with the x and y axis on time, polarization can be described by an ellipse as a general case. This ellipse is characterized by two angles, the tilt angle (polarization angle) α and the ellipticity angle ε. In the case of figure 2.2a, the wave has a linear polarization ($\varepsilon = 0$) and is tilted $\alpha = \frac{\pi}{4}$ from the reference frame.

A more general case would consider projections of the ellipse on the x and y axis. Phasor representation of projected fields would be

$$E_x = |A_x| \mathrm{e}^{j\theta_x}, E_y = |A_y| \mathrm{e}^{j\theta_y}. \tag{2.16}$$

The ellipse is described by three parameters: magnitudes A_x, A_y and the phase difference between components $\delta = \theta_x - \theta_y$. If either A_x or A_y are zero, the wave is linearly polarized. If both A_x and A_y are non-zero and $A_x \neq A_y$, the wave is elliptically polarized rotating

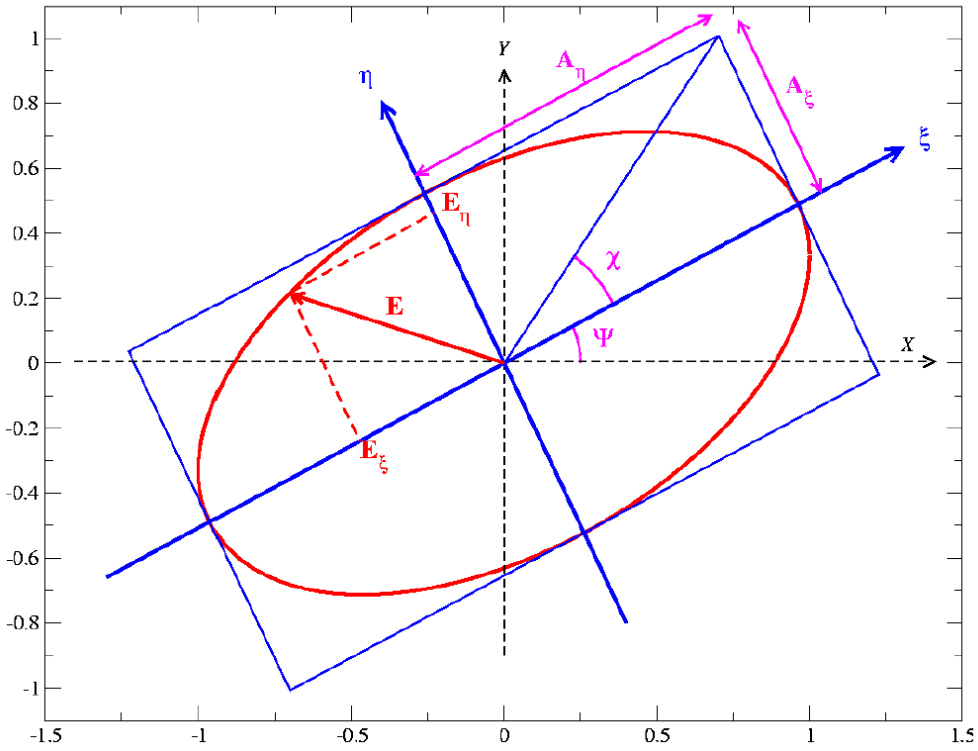

Figure 2.3: An intuitive approach to understand the polarization ellipse (Source: *Ph.D. Thesis, A. Alvear*).

clockwise if $\delta > 0$ or counter-clockwise if $\delta < 0$. If $A_x = A_y$ and $\delta = \pm\frac{\pi}{2}$, the wave is circularly polarized. Polarization angle is calculated as

$$\alpha = \arctan \frac{A_y}{A_x}. \tag{2.17}$$

A more intuitive description would be given by a reference frame rotated so that its axis would be parallel to the major and minor axis of the ellipse, as in figure 2.3 [8]. The projections of the ellipse on the new ξ and η axis correspond to the major and minor elliptical axis, of magnitude A_ξ and A_η respectively. There are new angles to characterize the ellipse, the tilt angle ψ and the ellipticity angle χ. These angles maintain trigonometric relations with the previously defined α and δ angles:

- $\tan(2\psi) = \tan(2\alpha)\cos(\delta)$
- $\sin(2\chi) = \sin(2\alpha)\sin(\delta)$

The ellipticity angle χ determines the spinning direction of the polarization and its shape:

- $\chi > 0$, right-hand elliptical polarization
- $\chi < 0$, left-hand elliptical polarization
- $\chi = 0$ or $\frac{\pi}{2}$, linear polarization (equals to $\delta = 0$ or π)
- $\chi = \pm\frac{\pi}{4}$, circular polarization (equals to $\delta = \pm\frac{\pi}{2}$)

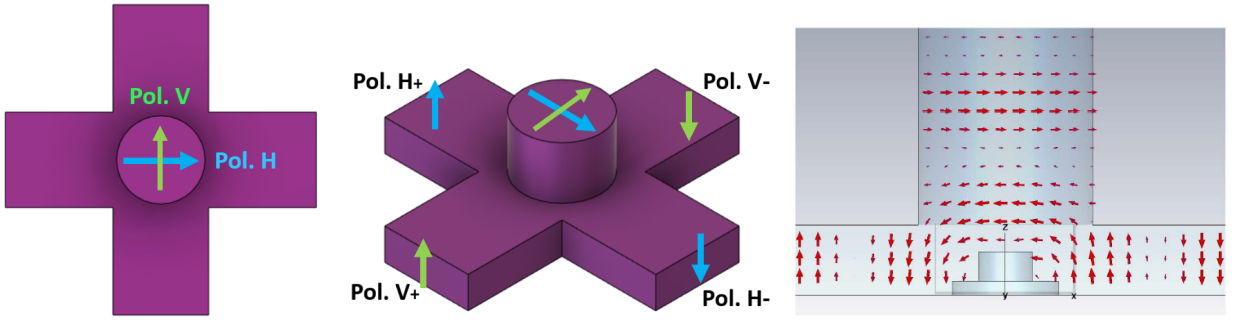

(a) Top view of a turnstile junction.

(b) Isometric view of a turnstile junction.

(c) Phase delay between branches of common polarization [10].

Figure 2.4: Scheme of a *turnstile junction* waveguide OMT. It serves as a simple example of an OMT, yet being a very performant design among those reported. (a): Superior view with polarization split designation. V stands for vertical, while H means horizontal. (b): Isometric view with polarization split designation. The phase difference between branches of a same polarization is indicated with arrows in opposite direction. (c): Detail of the phase delay between branches of one polarization, shown with arrows as a wave propagates into the turnstile junction of an OMT.

Note that the previously mentioned ways to describe the polarization ellipse are arbitrary. Regardless of the orientation from where the polarization of a wave is seen, two orthogonal components can be linearly combined as in equation 2.14 to describe the wave. This is of utmost importance to understand that the orthomode transducer will split the polarizations of an incoming signal regardless of its orientation in space and yield information in order to reconstruct it.

2.4 Orthomode Transducer

An orthomode transducer (OMT) is a passive device that receives, in general, an elliptically polarized signal as an input and yields as outputs the two linear orthogonal components that make up the former signal. The output signals have linear polarization and are paired per polarization. Polarizations are commonly referred to as V and H (vertical and horizontal). It is an intuitive designation to differentiate one polarization from the other while seeing the OMT from the input (figure 2.4a). The two signals belonging to each polarization are out of phase by 180^o as shown in figures 2.4b and 2.4c.

The OMT is placed parallel to the incoming wave fronts and is not necessary to be aligned with the semi-axis of the polarization ellipse to perform polarization split. The OMT operates as a power splitter if a linear polarized wave comes through. The amount of power delivered to each branch of the OMT depends on the wave's tilt angle referred to the symmetry axes of the OMT.

There are several architectures of OMT, which are reported in table 1.1 and figure 1.1. The *turnstile junction waveguide OMT* serves as a simple structure to explain the functioning of the instrument. It also has notable figures of merit in all the designs that consider this polarization-split strategy. However, it implies a complicated fabrication and is electrically

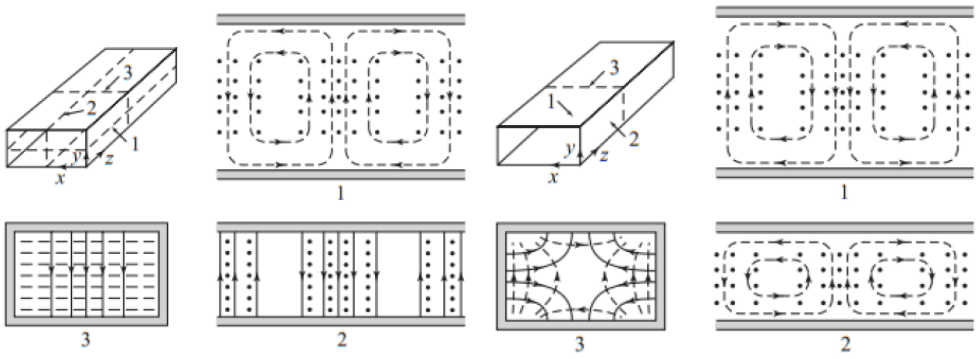

(a) TE_{10} mode. (b) TE_{11} mode.

Figure 2.5: TE modes of propagation. (Source: *Microwave Engineering, David M. Pozar*).

big, having paths long as several wavelengths.

When referring to a desired power transmission to a desired branch of the OMT (*i.e.* at an instant when the input electric field is parallel to a pair of branches of the OMT), it is often referred to as *co-polar* transmission. In the same scenario, the *cross-polarization transmissions* or simply *cross-polar* or even *cross-pol*, refers to the power transmitted to the orthogonal branch. The latter transmissions are undesired: the lower the cross-polarization levels, the purest are the obtained orthogonal polarizations from the input signal.

OMTs are evaluated regarding four figures of merit:

1. Reflection losses: how much power at the input is reflected back (to the sky, in a radio astronomy application). It gives, at a large extent, information about the operating bandwidth of the OMT.
2. Cross-polarization transmissions: how much power from the input, that should be transmitted to one polarization, is actually transmitted to the orthogonal. Cross-polarization completes the information about the operating bandwidth of the OMT and is the main figure of merit regarding the purity of the polarization split.
3. Isolation: the amount of power that can be transmitted from the output of one polarization all the way to the output of the orthogonal.
4. Insertion gain: transmissions of power to a desired branch of the OMT.

2.5 Electromagnetic Propagation in Waveguides

Even if the proposed OMTs of this thesis are based in planar structures, waveguides are inevitably part of the designs. This is because horn antennas are considered to build up the focal plane arrays that would contain the OMTs designed in this thesis, which integrate directly with waveguides. Waveguides are a type of transmission line consisting of a hollow cavity enclosed by a conductor. Most used shapes of the cavity section are rectangular and circular. Depending on the application, waveguides can have negligible losses and waves can propagate inside them describing different shapes in space, called propagation modes.

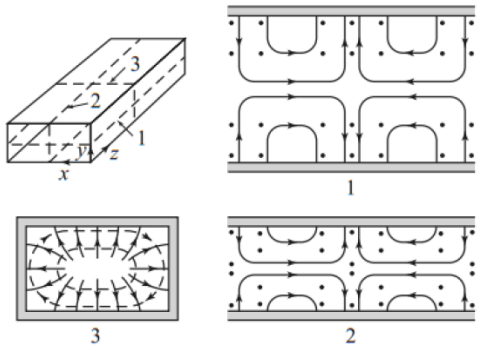

Figure 2.6: TM_{11} mode (Source: *Microwave Engineering, David M. Pozar*).

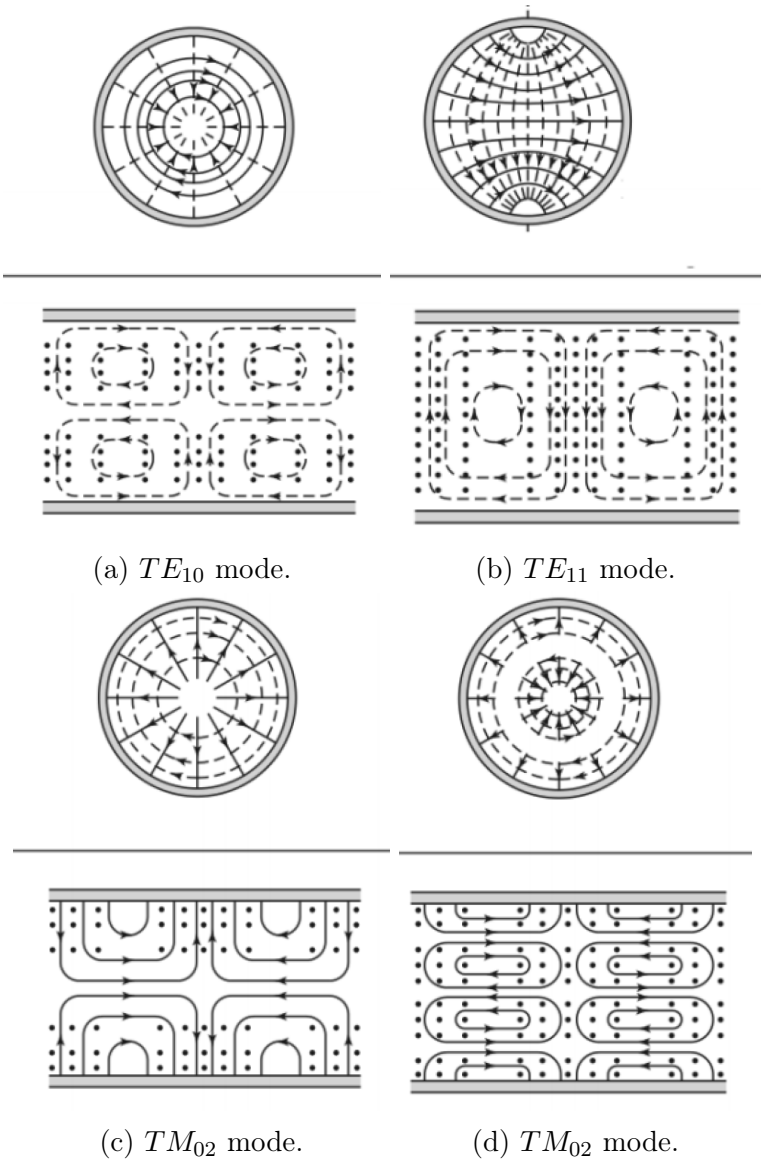

(a) TE_{10} mode.

(b) TE_{11} mode.

(c) TM_{02} mode.

(d) TM_{02} mode.

Figure 2.7: Circular waveguide modes of propagation (Source: *Microwave Engineering, David M. Pozar*).

2.5.1 Rectangular Waveguides

Rectangular waveguides have one side large as twice as the short one (a and b respectively in WR standard). They allow the propagation of TE and TM modes, but not TEM waves since only one conductor is used. Impedance of a rectangular waveguide is given by

$$Z_{wg} = 2\frac{\eta}{\sqrt{\varepsilon_r}}\frac{b}{a} \tag{2.18}$$

where a and b are the length of each side of the rectangular waveguide, ε_r is the relative permittivity of the waveguide filling medium, usually air, and $\eta = \sqrt{\frac{\mu_0}{\varepsilon_0}}$ is the free-space wave-impedance equal to 377 Ω [31].

TE Modes

TE modes are characterized by electric fields with $E_z = 0$, which means that the electric field only has transversal components. H_z must satisfy the reduced wave equation

$$\left(\frac{\partial^2}{\partial x^2} + \frac{\partial^2}{\partial y^2} + k_c^2\right) h_z(x, y) = 0, \tag{2.19}$$

with $H_z(x, y, z) = h_z(x, y, z)\mathrm{e}^{-j\beta z}$ and where $k_c^2 = k^2 - \beta^2$ is the cutoff wavenumber [27]. Higher order modes imply a propagation at a higher frequency. Figure 2.5 shows graphic examples of TE propagation modes of interest in this research [27].

Propagation mode TE_{11} (figure 2.5b) is the least desirable mode to propagate into the OMT since it would transport power to every branch of it, forcing a cross-pol level to exist.

TM Modes

TM modes are the analog of the TE modes for the magnetic field. Magnetic fields only have transversal components, then $H_z = 0$. E_z must satisfy the equation

$$\left(\frac{\partial^2}{\partial x^2} + \frac{\partial^2}{\partial y^2} + k_c^2\right) \mathrm{e}_z(x, y) = 0, \tag{2.20}$$

with $E_z(x, y, z) = \mathrm{e}_z(x, y, z)\mathrm{e}^{-j\beta z}$ and where $k_c^2 = k^2 - \beta^2$ is the cutoff wavenumber [27]. Figure 2.6 shows a graphic example of a TM mode that can propagate in waveguides. Note that it propagates with a radial distribution into the waveguide, thus it is an undesirable mode to propagate into the OMT just as the previously mentioned TE_{11} mode.

2.5.2 Circular Waveguides

Circular waveguides are cylindrical hollow pipes that support the propagation of TE and TM modes. Again, TEM modes are not supported due to the use of a single conductor.

TE Modes

Just like in the rectangular waveguide case, $E_z = 0$. H_z solves the equation

$$\nabla^2 H_z + k^2 H_z = 0, \tag{2.21}$$

with $H_z(\rho, \phi, z) = h_z(\rho, \phi)\mathrm{e}^{-j\beta z}$ in cylindrical coordinates. Figures 2.7a and 2.7b show TE modes that could propagate into a circular waveguide [27].

TM Modes

The analog case for the magnetic field is also true for circular waveguides. $H_z = 0$ and E_z solves the equation

$$\nabla^2 E_z + k^2 E_z = 0 \tag{2.22}$$

with $E_z(\rho, \phi, z) = \mathrm{e}_z(\rho, \phi)\mathrm{e}^{-j\beta z}$ in cylindrical coordinates. Figures 2.7c and 2.7d show the two lowest-frequency propagating TM modes in circular waveguides [27].

2.6 Microstrip Lines

Microstrip lines are the media in which the planar structures designed in this thesis are based on, and related key concepts are reviewed ahead. The microstrip line is a transmission line geometry with a single conductor trace on one side of a dielectric substrate and a single ground plane on the other side. It is by default an open structure, but can be enclosed by a conductor achieving electromagnetic improvements. The guided wavelength Λ is given by

$$\Lambda = \frac{\lambda}{\sqrt{\varepsilon_{eff}}}, \tag{2.23}$$

where λ is the free-space wavelength and ε_{eff} is the effective dielectric constant. The latter depends on the substrate dielectric constant and physical dimensions of the microstrip line. It is a weighted average between air and the substrate material calculated as

$$\varepsilon_{eff} = \frac{\varepsilon + 1}{2} + \frac{\varepsilon - 1}{2}\frac{1}{\sqrt{1 + 12h/W}} \tag{2.24}$$

since the electromagnetic fields exist partly in the air above the dielectric substrate and partly within the substrate itself. W is the width of the microstrip line and h is its height [32]

Microstrips are largely TEM transmission lines. Propagation is not TEM due to the combination of open air and substrate media, which means that microstrips are dispersive. Both the wave velocity and the characteristic impedance of the line vary with frequency rather than remaining constant. Even though dispersive effects are more likely to be evident by using narrow lines with a low dielectric constant substrate, dispersion is usually negligible [32].

2.6.1 Characteristic Impedance of the Microstrip Line

The characteristic impedance of the microstrip line can be approximated by assuming that the propagated electromagnetic field in the line is quasi TEM. The impedance of a microstrip can be calculated as

$$Z_0 = \begin{cases} \frac{60}{\sqrt{\varepsilon_{eff}}} ln\left(\frac{8h}{W} + \frac{W}{4h}\right)[\Omega] & \text{for } \frac{W}{h} \leq 1; \\ \frac{120\pi}{\sqrt{\varepsilon_{eff}}\left(\frac{W}{h} + 1.393 + 0.667 \cdot ln\left(\frac{W}{h} + 1.444\right)\right)}[\Omega] & \text{for } \frac{W}{h} > 1. \end{cases} \tag{2.25}$$

The width of the line is chosen depending on the desired impedance and application. The height is given by the manufacturer. However, it can vary marginally if other conductors are electrodeposited upon the conductors of the microstrip, such as nickel and gold.

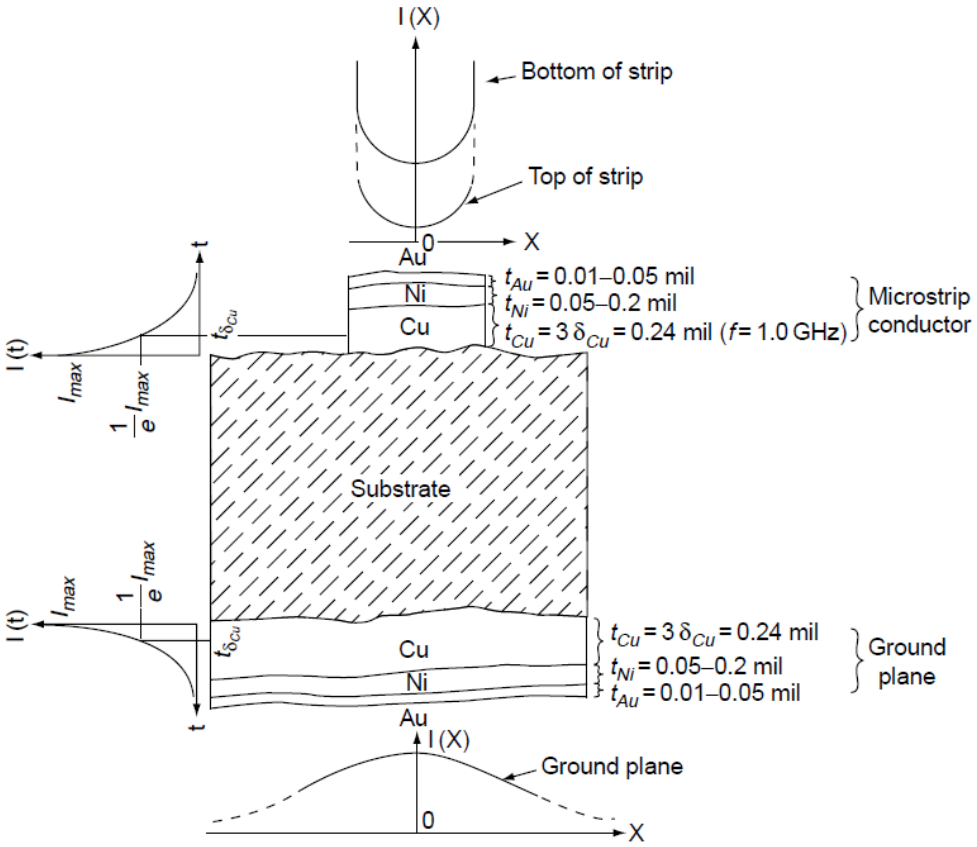

Figure 2.8: Current distribution across a microstrip conductors, modelling the skin effect. Note that the conductors are indicated with different layers of elements of the periodic table. This is done by electrodeposition, an electrochemical procedure to bond molecules of different conductive elements. Intermediate elements might be needed in order to deposit a specific conductor on the surface. In this case, the manufacturers' conductor (copper) is covered with nickel and then gold. Gold is used in circuits to prevent rust (Source: *Passive RF & Microwave Integrated Circuits, Leo G. Maloratsky*).

2.6.2 Attenuation in Microstrip Lines

Lossy effects that could attenuate a signal in a microstrip are of three types [32]

1. Radiation losses
2. Conductor (ohmic) losses
3. Dielectric losses

Radiation Losses

A microstrip line open to a semi-infinite air space can act as an antenna and radiate energy. Any current unbalance in the line may cause radiation. Radiation losses are more considerable for open microstrips with low dielectric constants ($\varepsilon < 5$) since a small part of the electric field is concentrated in the substrate region. However, radiation losses are negligible in closed microstrips, covered by a conducting cavity.

Conductor Losses

Conductor losses are a result of several factors related to the metallic material composing the microstrip, which are conductivity, skin depth and surface roughness.

The fabrication process of a microstrip creates scratches and bumps on the metal surfaces. The inner surfaces of the microstrip and the ground plane facing the substrate repeat the shape of the substrate, which might be flat and smooth or might have engraved stripped patterns, for instance. The current, concentrated in the metal surface next to the substrate, follows the uneven surface of the substrate and encounters greater resistance as compared with the case of a smooth substrate. As the roughness of the substrate surface increases, the length of the current path increases. Thus, the losses increase.

An idealized conductor has infinite conductivity. In the other hand, with finite conductivity, there is a nonuniform current density starting at the surface and exponentially decaying towards the substrate of the microstrip. This effect is called *skin effect* or skin depth. An approximation to its effect consists of a uniform current density flowing in a layer near the surface of the metallic elements to a uniform skin depth δ (figure 2.8 [32]). Skin depth is calculated as

$$\delta = \sqrt{\frac{1}{f\pi\mu\sigma}}, \tag{2.26}$$

where f is the frequency, σ is the conductivity of the metal at the surface of the microstrip line, and μ is the magnetic permeability of the metal (μ_0 for non ferromagnetic materials).

Dielectric Losses

The bulk of the substrate can also cause losses. Dielectric losses are usually quantified by the *loss tangent* ($tan\delta$). It is a dimensionless quantity related to the polarization effect that an electromagnetic wave causes in the substrate. When an electric field propagates through the microstrip, polarization occurs in the substrate and charges are displaced relative to the electric field. Dielectric losses cause a reduction in the overall electric field.

The loss tangent is the phase angle between the resistive and reactive components of a system with permittivity, calculated as

$$\tan\delta = \frac{1}{2\pi f R_p C_p}, \tag{2.27}$$

where δ is the loss angle, f the frequency, R_p and C_p the equivalent parallel resistance and capacitance of the microstrip, respectively.

Dielectric losses are associated with the quality of the substrate material. High quality low-loss dielectric substrates like alumina, quartz and sapphire are examples of good materials [32]. However, they may imply manufacturing constraints. For instance, quartz is a crystalline material that can only be cut in straight lines across a blank sheet, limiting the shapes that can be used to create a PCB.

2.7 Wide Bandwidth Antennas

The planar structures designed in this thesis to build up the OMTs act as coupling probes in a media transition. These probes must couple frequencies from a waveguide to a mcirostrip line in a broad bandwidth. Therefore, wide band operating antennas are studied regarding their types, advantages and drawbacks, and techniques to achieve wide frequency bands of operation. Operating bandwidth is one of the most important parameters of an antenna, specially for radio astronomy applications. Some methods have been exploited to achieve bandwidth enhancement for different types of antennas [33].

2.7.1 Resonant antennas: an overview

Resonant antennas are not really likely to achieve broadband performance. They are also always limited by adequate impedance match [34]. Some examples of resonant antennas are the straight wire dipole and microstrip patch antennas. However, there are some related concepts that are helpful to be reviewed before introducing further theory about antennas.

Resonant antennas operate at a single resonance mode, which is related to the electrical size of the antenna. The wave travelling outward from the feed point to the end of the antenna is reflected, setting up a standing-wave-type current distribution on the antenna surface. These antennas are also referred to as standing wave antennas.

The operating bandwidth of the antenna is related to the antenna quality factor Q and the radiation efficiency e_{rad}, which is in turn proportional to the antenna gain. The following equation states the inverse relation between bandwidth and quality factor

$$BW = 2\frac{\triangle f_H}{f_0} = \frac{1}{Q}, \tag{2.28}$$

where $\triangle f_H$ is the half-power-bandwidth surrounding the resonant frequency f_0.

The quality factor Q of an antenna is defined as $2\pi f$ times the energy stored over the power radiated and the ohmic losses. It can be calculated through the equivalent circuit of an antenna:

$$Q = \frac{1}{2\pi f_0 R_r C} \cdot \frac{R_r}{R_r + R_L} = Q_{lossless} \cdot \mathrm{e}_{rad}, \tag{2.29}$$

where $Q_{lossless}$ is the quality factor assuming no ohmic losses ($R_L = 0$), $\mathrm{e}_{\mathrm{rad}}$ is the radiation efficiency, R_r is the radiation resistance and C is the equivallent capacitance of the antenna [33].

There are fundamental limitations for electrically small antennas [35, 36]. An electrically small antenna is the one whose largest linear dimension $2r$ satisfies the condition $kr < 1$, where k is the wave number equal to $2\pi/\lambda$.

When $kr < 1$, the quality factor Q of a small antenna can be expressed as [37]:

$$Q = \frac{1 + 3(kr)^2}{(kr)^3[1 + (kr)^2]} \cdot \mathrm{e}_{rad}. \tag{2.30}$$

Therefore, the quality factor Q and the antenna size as well as the radiation efficiency are related in one single equation.

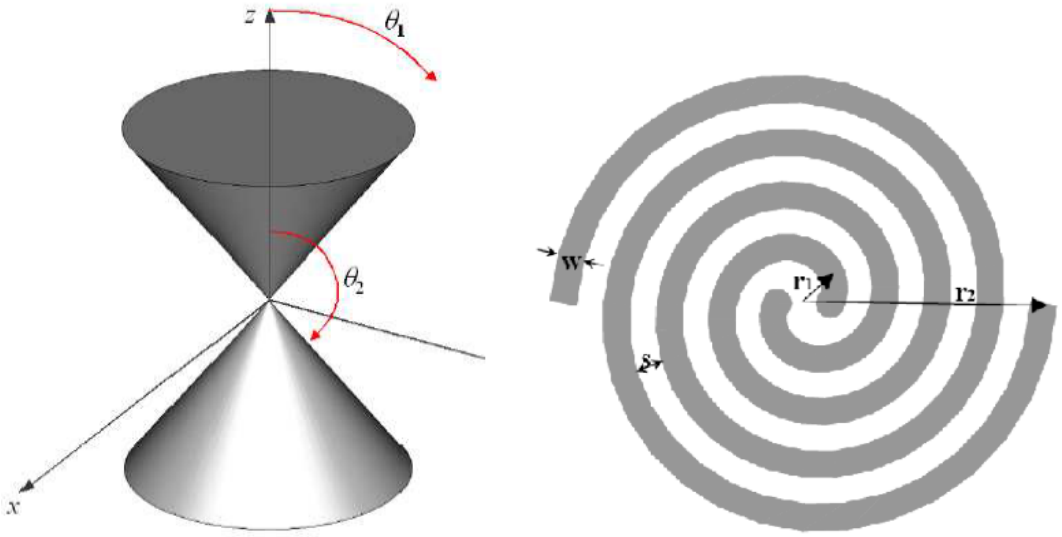

(a) Biconical antenna scheme. (b) Spiral antenna scheme.

Figure 2.9: Antennas whose shapes achieve angle-only-specification or self-complementarity principles (Source: *Antenna Study and Design for Ultra Wideband Communication Applications, J. Liang*).

Since the Q-factor rises rapidly as antenna size decreases, the result relates the lowest achievable Q to the maximum dimension of an electrically small antenna. Because the antenna bandwidth is the reciprocity of Q, the increasing Q with reducing size r indeed implies a limitation on the widest achievable bandwidth. Thus, there is always a trade off between them to obtain an optimal antenna performance and there is no complete freedom to independently optimize each one [33].

2.7.2 Resonance overlapping type of antennas

Normally, the bandwidth of a resonant antenna is not very broad because it has only one resonance. However, if there are two or more resonant parts available with each one operating at its own resonance, the overlapping of these multiple resonances may lead to multi-band or broadband performance. Theoretically, an ultra wide bandwidth can be obtained if there are a sufficient number of resonant parts and their resonances can overlap each other well.

However, in practice it is difficult to achieve impedance matching over the entire frequency range when there are more resonant parts. That means, it is difficult to achieve constant radiation paatterns if there are more different radiating elements, which is the main drawback of these kinds of antennas [33].

2.7.3 Travelling Wave Antennas

Contrary to the case of resonant antennas, or standing wave antennas, an antenna can act as a guiding structure for a travelling wave. The standing wave pattern on its surface is negligible and the energy of the travelling wave is radiated. Travelling wave antennas can be created by using a matched load at the ends of the antenna to prevent reflections. Long

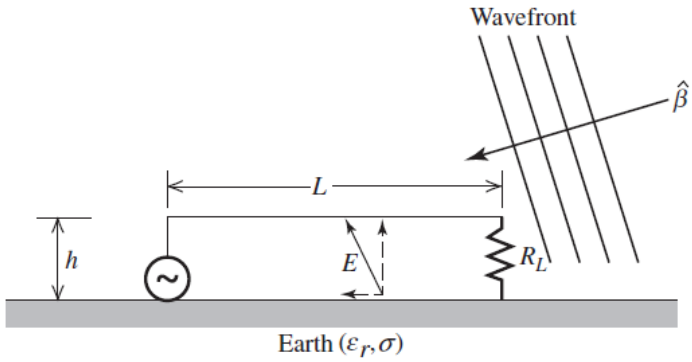

Figure 2.10: Diagram of a Beverage antenna of length L and separation h from the ground plane, receiving an incoming wavefront (Source: *Antenna Theory and Design, Warren L. Stutzman*).

antennas also act as travelling wave antennas because most of the power is dissipated, leading to small reflected waves. A long antenna or long wire is one that is greater than one-half wavelength long ($l > \lambda/2$) [34].

The input impedance of a traveling-wave antenna is always predominantly real. The impedance of a pure traveling wave on a low-loss transmission line is equal to the real part of the characteristic impedance of the transmission line that propagates it. Antennas that support traveling waves operate in a similar manner. The traveling wave feature not only improves the pattern but also produces wider impedance bandwidth. The radiation resistance of a traveling-wave long wire antenna is 200 to 300 Ω. Well-designed traveling-wave antennas have input impedances that have little reactance since there is little or no reflected power [34].

Other than electrically long antennas, examples of travelling wave antennas are the biconical, spiral and log-periodic antennas. These designs and some others satisfy three principles to achieve *frequency independent characteristics* [33, 34]:

1. The antenna shape is specified only in terms of angles (*e.g.* biconical antenna, figure 2.9a).

2. The antenna shape is self-complementary, *i.e.* the metal and the air regions of the antenna are equal (*e.g.* spiral antenna, figure 2.9b).

3. The antenna is made out of thick conductors, differing from an antenna made from wires. Increasing the thickness usually widens the bandwidth. Both antennas of figure 2.9 are examples of "fat" antennas.

One further example of a travelling wave antenna is the Beverage Antenna. It consists of a long wire operating in the presence of an imperfect ground plane as shown in figure 2.10 [34]. The incoming plane wave produces a component parallel to the length of the antenna, which is not totally shorted out by the imperfect connection to earth. Thus, an unbalanced current is induced on the antenna, then it can radiate.

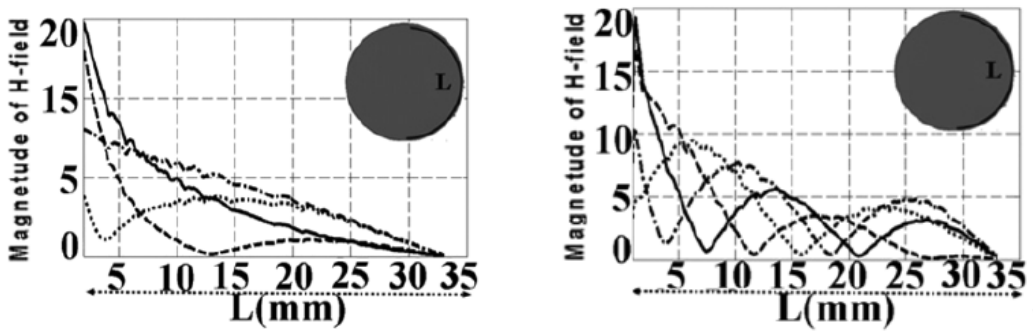

(a) Standing wave current distribution. (b) Travelling wave current distribution.

Figure 2.11: Magnetic field distributions along a line L of the circumference from a circular planar monopole for different frequencies. (a) Standing wave magnetic field distribution at 3 GHz. (b) A travelling wave distribution is excited at 10 GHz. (Source: *Systematic Design of UWB Monopole Antennas With Stable Omnidirectional Radiation Pattern, Fereidoony et. al.*).

2.7.4 "Fat" monopoles

Conventional monopoles have a straight wire configuration against a ground element (not necessarily a plane). They are widely used for communication systems since they have isotropic radiation pattern, are simple to fabricate, cheap and easily match 50 Ω ports. They do not offer a broad bandwidth, but it has been studied that a thicker or "fatter" structure for the main conductor will lead to a broader bandwidth [38]. An increased current area implies an increased radiation resistance. The term fat is used in [33] and in [34] to differentiate a thick structure from a wire when constructing an antenna.

The main drawback from thickening a monopole is that there could be a significant impedance mismatch between the antenna and the transmission line in use, so that the bandwidth could not be improved further.

Dipoles also benefit from thickening their conductors. The biconical antenna of figure 2.9a is a good example of a three-dimensional dipole. A thick planar dipole example is the bow tie antenna. Fat planar monopoles also exist and are similar in shape to microstrip patch antennas, although without a ground plane completely covering the back of the substrate [33].

2.7.5 Mixed antennas

If an antenna operates in a broad bandwidth, it might accomplish or not the small antenna criterion $kr < 1$ depending on the frequency of the stimulus. A standing wave current distribution can be excited if the propagated wavelength is larger than the antenna, where regions concentrate current density for any phase shift of the propagating wave. Otherwise, a travelling wave current distribution can be found on the antenna, where maxima and null propagate as the phase varies. In other words, depending on the frequency of operation, current distributions on the antenna surface can vary their patterns as the waves propagate. It is reported in [39] that a planar monopole can have such a behaviour studied from the

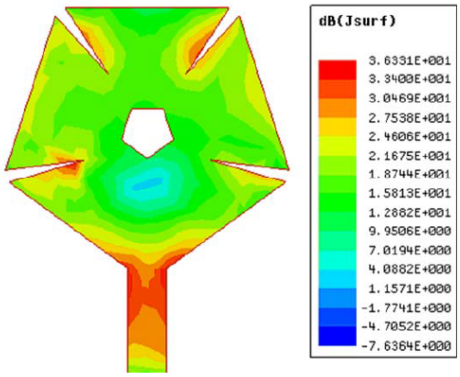

Figure 2.12: Simulated current distribution on an engraved patch antenna surface (Source: *V-Shaped Slits and a Slot Loaded Pentagonal Boundary Patch Antennas for Wideband Applications, Rajasekhar et. al.*).

magnetic field distribution along a line across a monopole antenna. Note that figure 2.11 shows magnetic field distributions, which are directly related to the current distribution. On a surface, the tangential magnetic field H_{tan} is related to the surface current J_s by

$$H_{tan} = J_s, \tag{2.31}$$

assuming a perfect conductor surface [34]. A standing wave current distributions (figure 2.11a) is shown on the antenna surface for low frequencies and a travelling wave current distribution (figure 2.11b) for high frequencies. Therefore, the antenna behaves as a resonant antenna and a travelling wave antenna depending on the propagating frequency.

2.7.6 One further technique: slits for bandwidth enhancement

The current distribution of an antenna can be modified to achieve desired effects on the bandwidth. For instance, stop band effects can be achieved by properly placing an asymmetrical slit on the main conductor of the antenna [40]. Such effect is desirable for telecommunications applications, where an antenna must radiate in a discontinuous bandwidth.

In [41], a portion of the operation frequency band is reportedly suppressed by the inclusion of slits and a central slot on a patch antenna. In contrast, a bandwidth improvement is also attributed to a slit addition. This enhancement is attributed to a surface current accumulated near the slits on the notched frequency band as shown in figure 2.12, while the flow of current on the surface is enhanced for the rest of the frequency band. Thus, the overall bandwidth as well as gain are improved. In [39, 40, 41], a defective or irregular ground structure is also mentioned to have implications in band widening.

In [42], a comparison is made between structures that could improve bandwidth of a microstrip antenna. A plain antenna is compared to one of the same dimensions but with notched corners, one with symmetrical slits and one with a centered slot on the radiating surface. All the engraved antennas show less gain and more bandwidth than the plain antenna. Current distributions are modified in different ways. What they have in common is that the surface current concentrates around the antenna engravings and the microstrip line

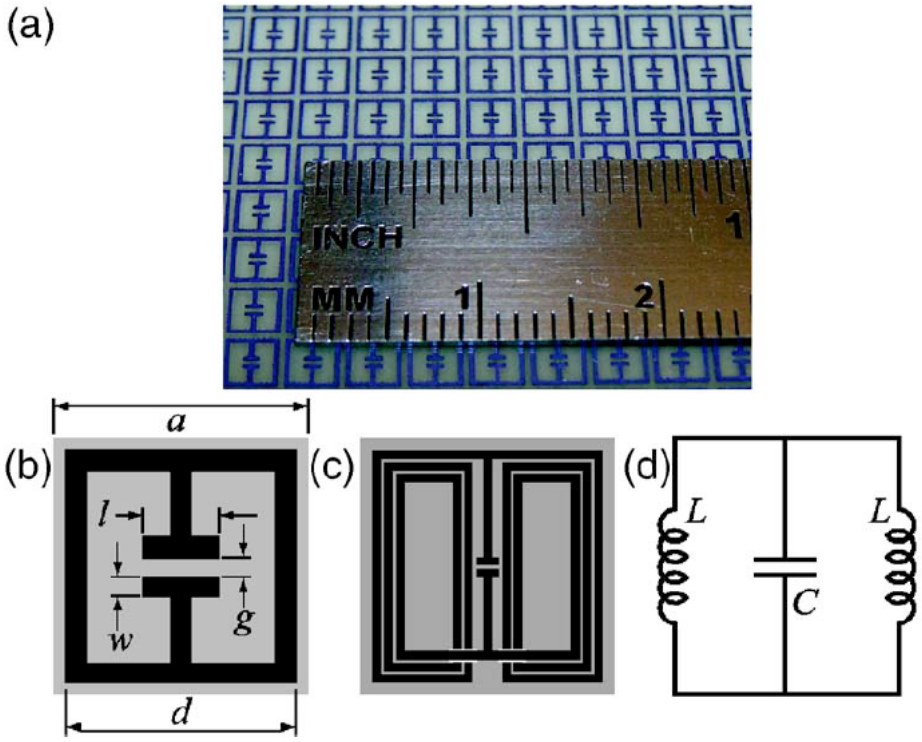

Figure 2.13: A fabricated metamaterial. (a) Fabricated sample with scale. (b) Geometric design of each element of the fabricated metamaterial. (c) A proposed design for the same purpose with different properties, such as a lower resonant frequency. (d) Equivalent circuit of each block of the material (Source: *Electric-field-coupled resonators for negative permittivity metamaterials, Schurig et. al.*).

out of the antenna. Even though the current is distributed around these features and in the transmission line, it does not necessarily mean that a stationary current distribution is been excited on the surface of the antenna.

2.8 Metamaterials

Some types of antennas, some reported in the literature and one in particular studied in this thesis, are claimed to be based on metamaterials. A metamaterial is an artificially manufactured material that has properties not found in its constituents [43]. A metamaterial is a structure made from periodically replicated blocks across a surface. These blocks can be physically discontinuous. If a microwave propagates through a metamaterial whose blocks are smaller than its wavelength, the wave can interact with it as if the structure was electrically continuous [44]. In some cases, the blocks describe a fractal form, self-defining a bigger structure.

Metamaterials achieve different beneficial properties. The most studied property is that they can offer regions with positive and/or negative permittivity and permeability (ε_r and μ_r). A wave propagating through a conventional material with $\varepsilon_r > 0$ and $\mu_r > 0$ undergoes a phase delay. If a wave propagates through a material with $\varepsilon_r < 0$ and $\mu_r < 0$, a phase advance

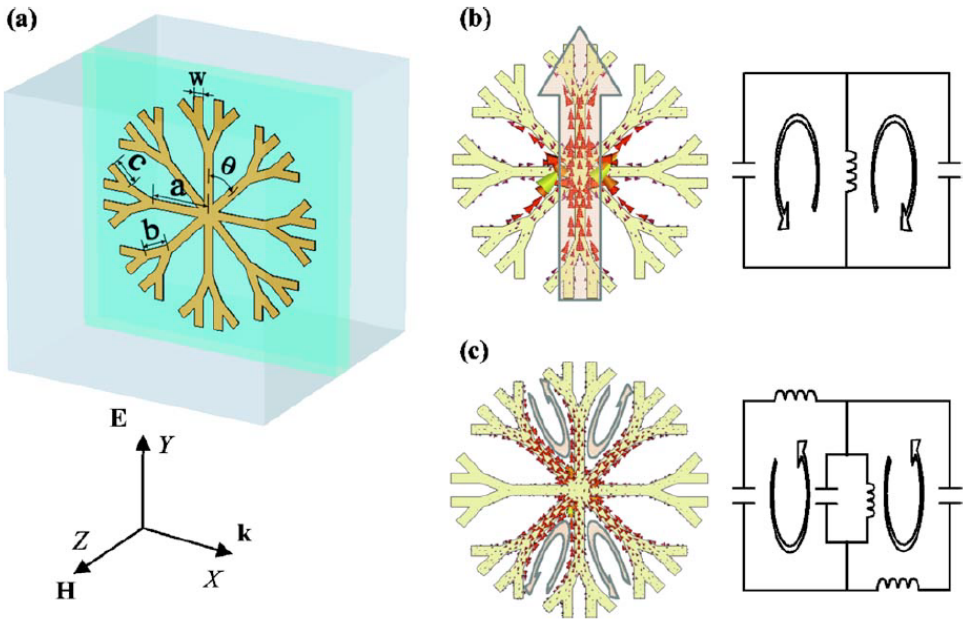

Figure 2.14: Modelling of a unit cell from a metamaterial and its surface current. (a) Scheme in 3D. (b) Surface current distribution in the first resonant mode with equivalent LC circuit of the unit. (c) Surface current distribution in the second resonant mode with equivalent LC circuit. Note that circuits are not equal depending on the resonant mode. Arrows indicate the instantaneous current direction, which also varies with the frequency mode (Source: *Resonant condition of unitary dendritic structure with overlapping negative permittivity and permeability, Zhou et. al.*).

occurs. This property among others occur in certain regions and for certain frequencies, since the interaction of waves with the overall structure of a metamaterial changes with the variation of wavelength.

Some metamaterials are made by structures similar to inductances or capacitances. Equivalent circuits can be modeled as in figure 2.13 [45]. As a general rule, elements similar to parallel plates are considered as capacitors. Those similar to wires are inductors. Since the metamaterial interacts differently with the microwaves depending on their wavelength, different circuital models can represent a single structure. In figure 2.14, two different equivalent circuits represent a single metamaterial structure depending on the order of the resonant mode being excited [46].

2.9 Summary

In this chapter, important topics have been reviewed to understand the work in this thesis. Fundamentals of electromagnetism led to the study of the polarization of a wave, a key concept. The orthomode transducer was introduced, being the central topic of study in this work. Theory of transmission lines was presented together with the theory of broadband antennas to understand some choices of design. Lastly, an introduction to metamaterials is shown since these structures will be used along the course of this study.

Chapter 3

Methodology

In this chapter, the methodology followed during this work is separated into three stages, which are Design and Simulation, Analysis of Results, and Comparison of Results. A conclusion is stated at the end of the research, pointing out the most important findings and the future work to be carried out in the same line of this research. Ahead follows an explanation for each stage of this work.

3.1 Design and Simulation

The first step consists of designing the two proposed front ends, and optimize the shapes and dimensions of their components in an iterative process. The components are the OMT, main element of each front end, and the transitions from waveguide to microstrip probes for the local oscillator (LO) for the heterodyne mixers, including a waveguide splitter network. These components are indicated as *planar transitions* in figure 1.3. The simulations and re-designs are iterated until the objectives are met or surpassed regarding the main electromagnetic figures of merit of the front ends, stated at section 1.6. The design and simulations are carried out in ANSYS HFSS software, using the finite element method (FEM). This procedure is preferred over the method of moments (MoM) because the FEM solves better electromagnetic phenomena inside three-dimensional structures than MoM. Despite the proposed orthomode transducers of this thesis are planar, they are simulated inside a three-dimensional structure.

One front end is designed and simulated at a time. The first front end to be designed is the Planar Version (PV), named Planar because its OMT is made by a continuous planar structure containing microstrip probes, as shown in figure 3.1. Even if the transitions from waveguide to microstrip for the LO splitter are made from planar structures as well, they are not made from a single substrate. An isometric view of both the PV OMT nad PV LO splitter is also shown in figure 3.1, aligned as they would be implemented. Note that the OMT is concentric to the LO splitter transitions and is considerably smaller. Between the OMT and each LO transition, the MMIC from figure 1.2a is considered to be placed but is not included in the simulations of this thesis.

After the simulations of the Planar version OMT and LO splitter meet the objectives, the

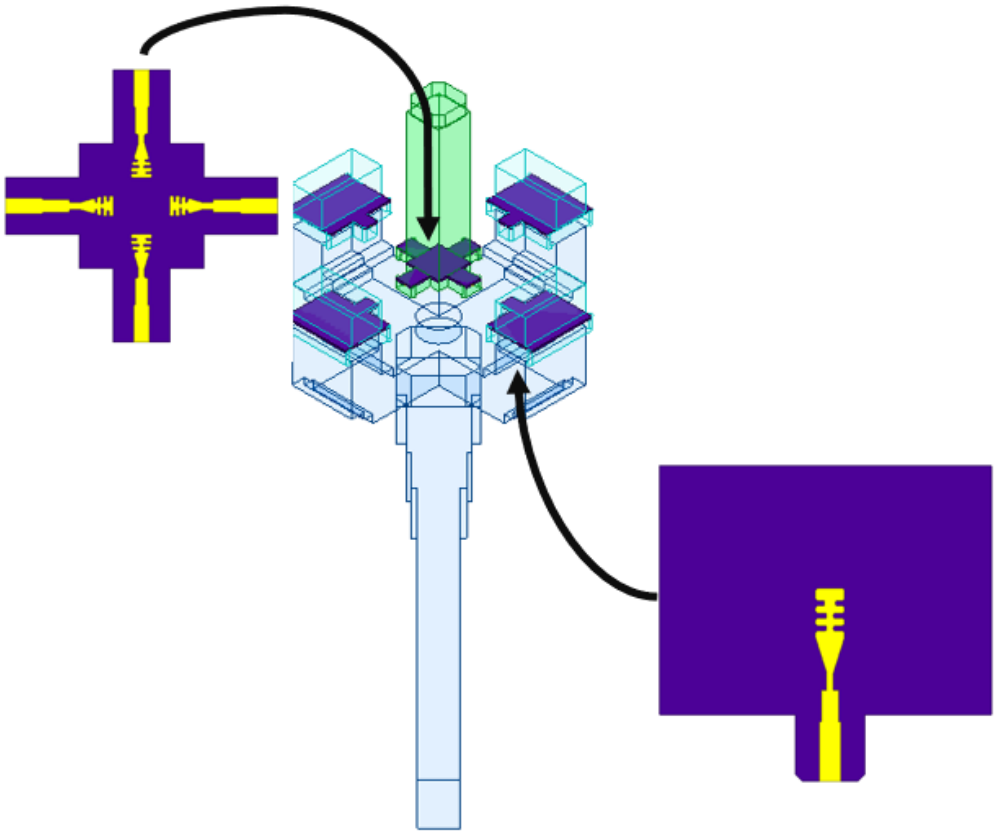

Figure 3.1: View of the different components designed in this thesis for the Planar Version (PV) of the front end. In the center, an isometric view of the PV OMT and LO splitter network. To the left, a top view of the PV OMT with an arrow showing its position in the isometric view of the components. To the right, a top view of a single microstrip transition used for the LO splitter with an arrow indicating its position into the splitter. Note that substrates are flipped in the isometric view, so probes are hidden. Substrates are shown in purple, waveguide cavities in light blue and green, and gold probes are yellow.

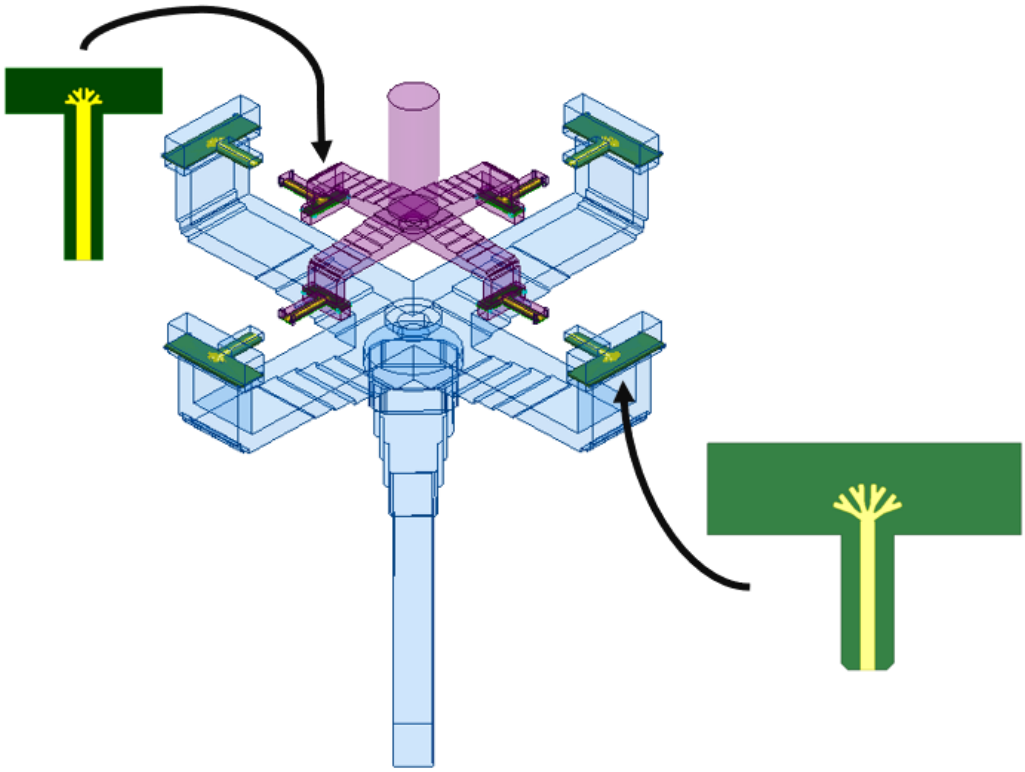

Figure 3.2: View of the different components designed in this thesis for the Semi-Turnstile Version (STV) of the front end. In the center, an isometric view of the STV OMT and LO splitter network. To the left, a top view of a single STV probe for the OMT, and an arrow showing its placement into the OMT. To the right, a top view of a single LO splitter microstrip transition used for the LO splitter, with an arrow indicating its position into the splitter. Substrates are shown in green, waveguide cavities in light blue and purple, and probes are yellow.

design of the second front end starts with the objective to improve the Planar version by trying another architecture. The second version is called Semi-Turnstile Version (STV) because is made from a waveguide turnstile OMT cut at half and merged with planar structures as media transitions. Figure 3.2 shows an isometric view of the designed OMT and LO splitter including the required microstrip probes. Arrow show where each probe is placed. As for the Planar version, between each microstrip transition from the STV OMT and LO splitter, an MMIC mixer containing the circuit from figure 1.2a is considered to be placed but neglected from these simulations. The design and simulation process ends when the Semi-Turnstile OMT and LO splitter meet the previously set objectives.

3.2 Analysis of Results

After the Planar and Semi-Turnstile front ends' designs are considered to be ready, further analysis of the simulation results is carried out. A fabrication analysis is performed using ANSYS HFSS, iterating a parametric analysis over a certain amount of design parameters. The objective of this analysis is to determine those lengths, depths or widths of the designs that are critical to the overall performance and those that tolerate some error when the front ends are fabricated.

The levels of cross-polarization are given particular attention to, because cross-polarization transmissions are the main figure of merit that characterizes the purity of the polarization split performed by the OMT. The designed OMTs are compared to reported OMTs regarding fractional bandwidth and cross-polarization, considering simulation results. Additionally, results from Ansys HFSS of both versions' OMTs are exported to be post processed using National Instruments AWR software. This export is done because of AWR's additional functionalities as compared to HFSS to perform the proposed analyses. Using AWR, the detriment on the cross-polarization figure of merit is studied by simulating realistic scenarios of operation for the OMTs. The connection of different loads were simulated, such as mixers or low noise amplifiers of different quality, resembling different circuits connected right after the OMT ports. An additional analysis on the isolation tolerance for physical set up mismatches is carried out using AWR.

Lastly, an analysis of the current distribution on the microstrip probes for both designed OMTs is also carried out using Ansys HFSS. This analysis tries to explain what kind of antennas can the designed microstrip probes be classified into, and how they work. Additionally, the effect of deformations or engravements on the radiating surface of an antenna are expected to be identified, since ambiguous or misleading answers were found in the literature.

3.3 Comparison of results

Once the analysis of the results is done, a comparison is made between the Planar Version and the Semi-Turnstile Version front ends. Comparison is done regarding the electromagnetic figures of merit and the mechanical aspects of the manufacturing of both front ends. The electromagnetic comparison is rather direct from comparing the figures of merit. The mechanical comparison is carried out considering the objective to design a front end that would integrate a focal plane array, and that an instrument of simple fabrication is expected.

This comparison considers the required level of detail to fabricate each front end, the ease of assembly of the different parts, and errors associated with the overall manufacturing process for both the PV and STV versions. Therefore, the mechanical comparison is not as direct as the electromagnetic comparison. It is a multi-variable problem of choice, rather than a magnitude-comparing exercise.

As a conclusion of this work, the convenient front end version to be further developed or manufactured is chosen. Relevant findings are pointed out and the guidelines for future work are stated.

3.4 Summary

In this chapter, the different stages of the study for this research are reviewed. One front end is designed and simulated at a time, and the main component of study is the OMT of each front end. The first version developed is based on an OMT with a continuous planar structure that splits the polarizations. The second front end is based on a truncated turnstile-junction OMT. After the simulations are performed, the data is further analyzed and additional tests are performed to better study each front end. A conclusion stating which design better accomplishes the objectives is stated at the end of the research, and guidelines to future work are given.

Chapter 4

Planar Version of OMT and Front End

In this chapter, the design and results of the first version of the front end are shown. From now on, any structure related to this version will be called *Planar Version* or just *PV* as an acronym. It is called Planar because the OMT of this version is made from a continuous planar structure. First, the design and simulation results are shown for the OMT, which is the most critical structure of the front end. Secondly, the LO splitter design is shown with its results. The overall mechanical block that would contain the OMT with the splitter and other required components is also reviewed. At the end of this chapter, observations of this version are made leading to the next version of design.

4.1 PV OMT

Design and simulation results of the PV OMT are reviewed.

4.1.1 PV OMT Design

The design of the PV OMT is shown in figure 4.1. Astronomical signal enters through the top of the model (figure 4.1a), and the probes can be seen from the bottom (figure 4.1b). This is done this way to align the probes from the OMT, the MMIC mixer and the probes for the LO splitter in a single plane when constructing the receiver.

The OMT is based on a planar substrate confined by a waveguide cavity. The considered substrate is **Rogers RT/duroid 6202**, which has a dielectric constant of $\varepsilon = 2.94$ and is $0.127\ mm$ thick. It must allow modes to propagate inside while splitting the polarizations. The air below the substrate seen in figure 4.1c is a backshort which has at its centre a tuning metallic stub. The height of the backshort, and both the radius and height of this stub are among the most critical variables of this design. Other crucial parameters of this design are the widths and lengths of the impedance matching section of the probes. They had influence on the reflection losses of the OMT and also on its operating bandwidth. Critical parameters are studied in more depth later in this thesis.

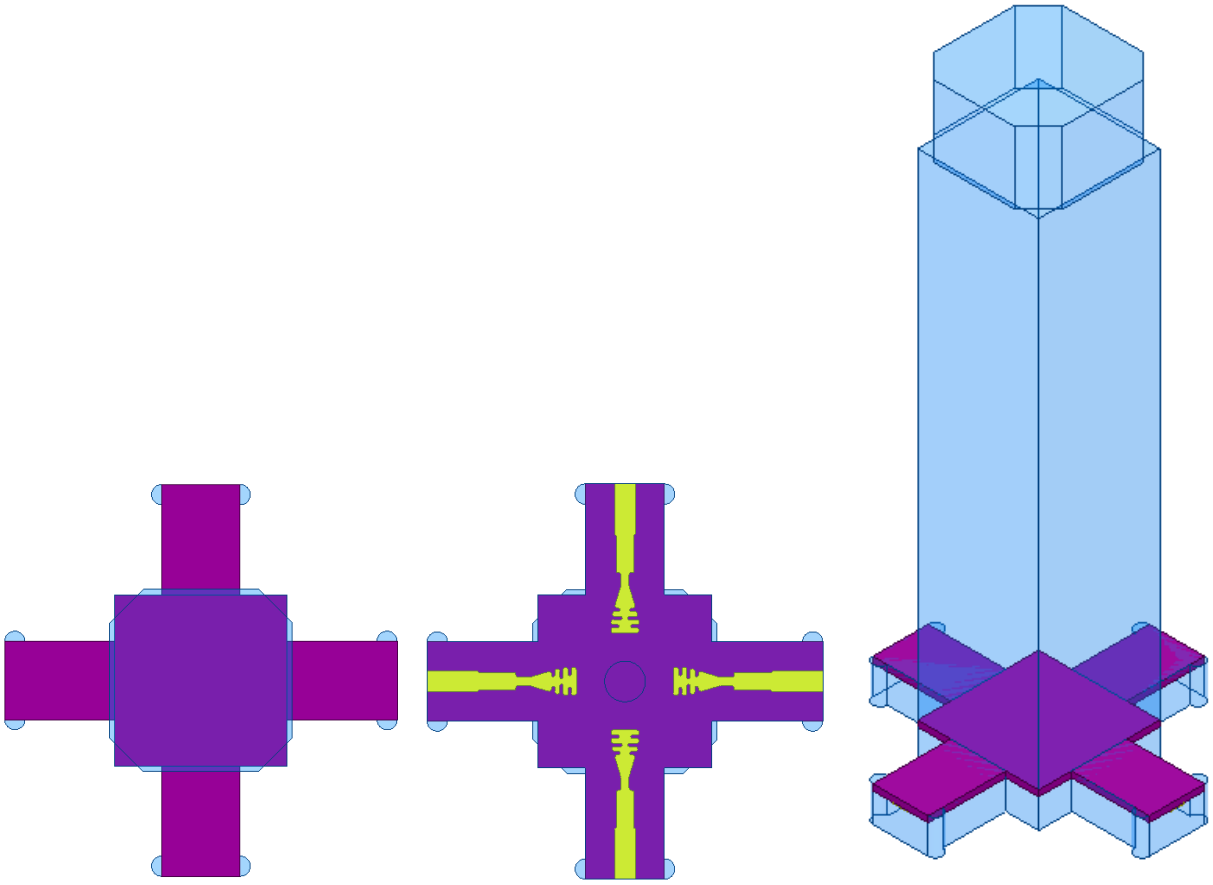

(a) Top View. (b) Bottom view. (c) Isometric view.

Figure 4.1: Different views of the PV OMT. Air regions confined by waveguides are rendered in light blue. The substrate is purple, and microstrip probes are yellow. (a) Top view. The astronomical signal enters the OMT towards the purple substrate. (b) Bottom view. Probes are seen from the bottom due to a choice of design to ease the overall receiver's assembly. (c) Isometric view of the OMT.

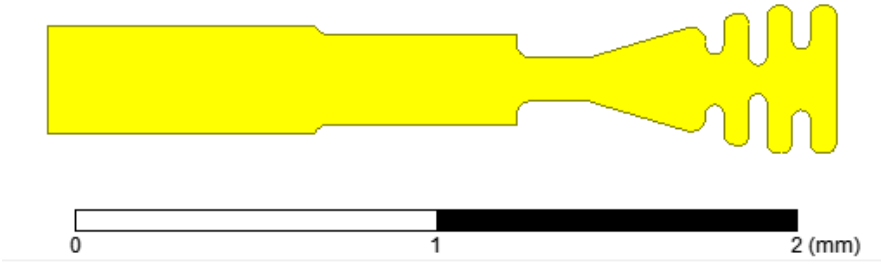

Figure 4.2: Detail of the probe designed for the PV OMT. A metric scale is included.

A detailed view of the designed probe is shown in figure 4.2. Its shape started from a radial probe, to a palette shape, which was then slitted symmetrically from each side. The antenna connects to the microstrip line through an adaptation section, which thickens in a staggered way. It is optimized to match a 50 Ω microstrip line.

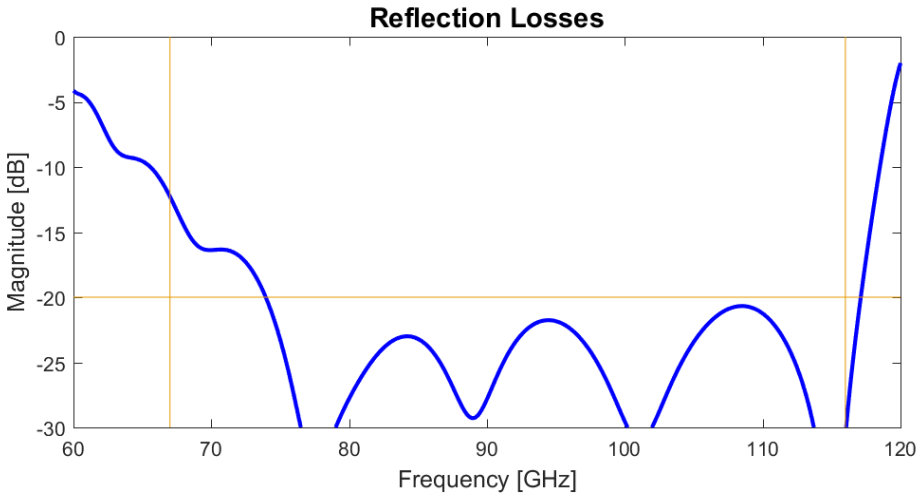

Figure 4.3: Reflections at the input of the PV OMT.

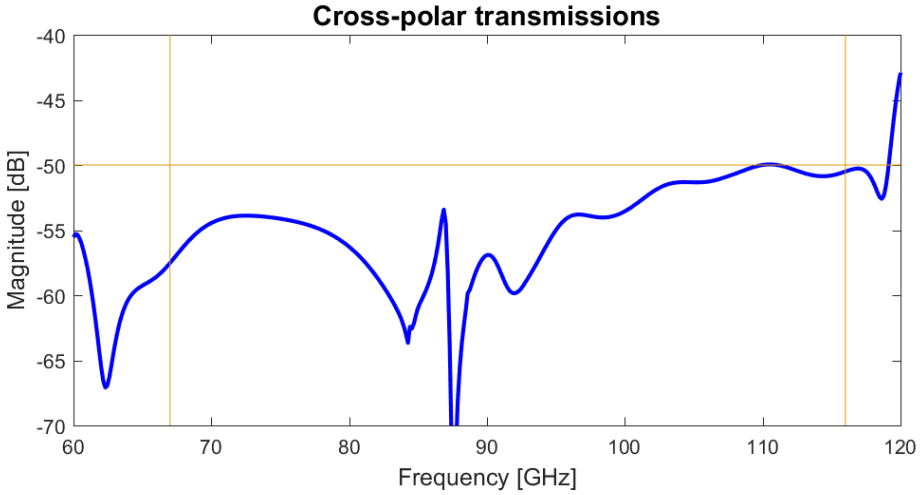

Figure 4.4: Cross-polar transmissions of the PV OMT.

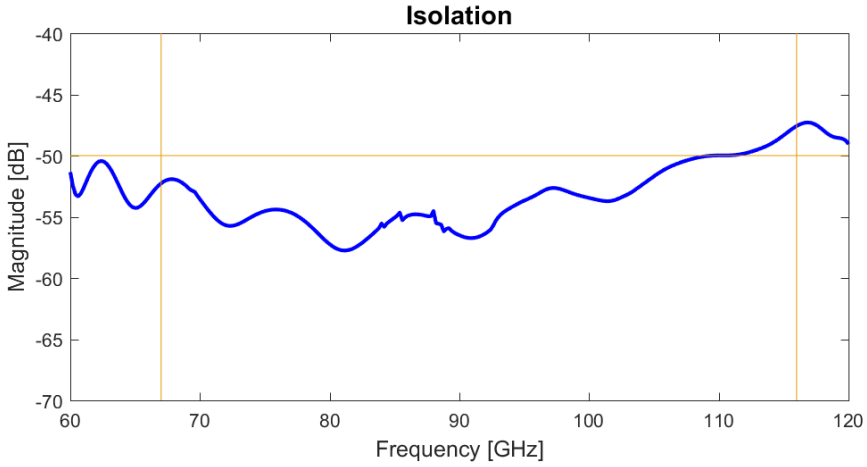

Figure 4.5: Isolation between polarization output ports of the PV OMT.

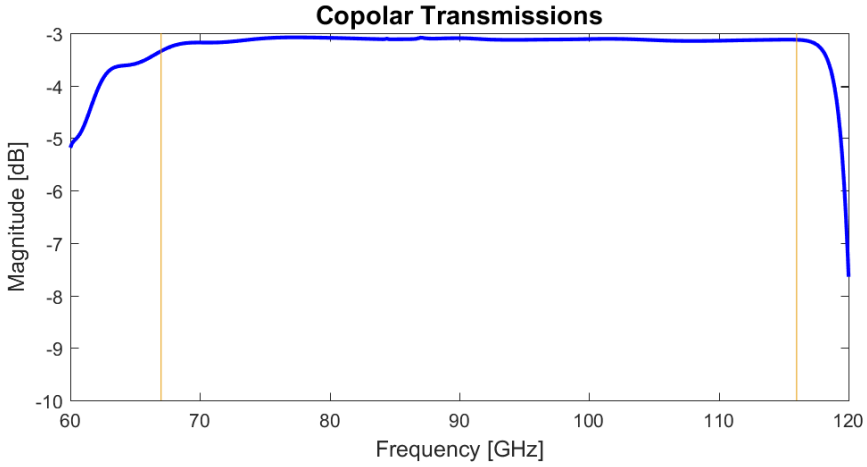

Figure 4.6: Co-polar transmissions of the PV OMT.

4.1.2 PV OMT simulation results

Simulations are performed using Ansys HFSS software. Operating fractional bandwidth is equal to a 44.5% (figure 4.3). Cross-polar transmissions are better than -50 dB for the complete ALMA band 2+3 (figure 4.4). Isolation between ports is less than -47 dB for the band (figure 4.5). These two figures of merit are related and have similar meaning, but cross-polar transmissions give more complete information about the OMTs performance. Co-polar transmissions are shown in figure 4.6 and are better than -3.5 dB for the entire band. This is close enough to the theory limit of -3 dB, since the power is split into two by entering the OMT.

Note that in both figures 4.4 and 4.5, resonant points appear between 80 an 90 GHz. According to [47], OMTs are structures likely to show resonances and, for a resonance to propagate, three conditions must be satisfied. These conditions are that a spurious mode must propagate, the mode must be trapped and that the size of the trap must be sufficient for the mode to be resonant. Most of the resonances require discontinuities or asymmetries to couple to dominant modes. Resonances appeared throughout the entire process of optimiza-

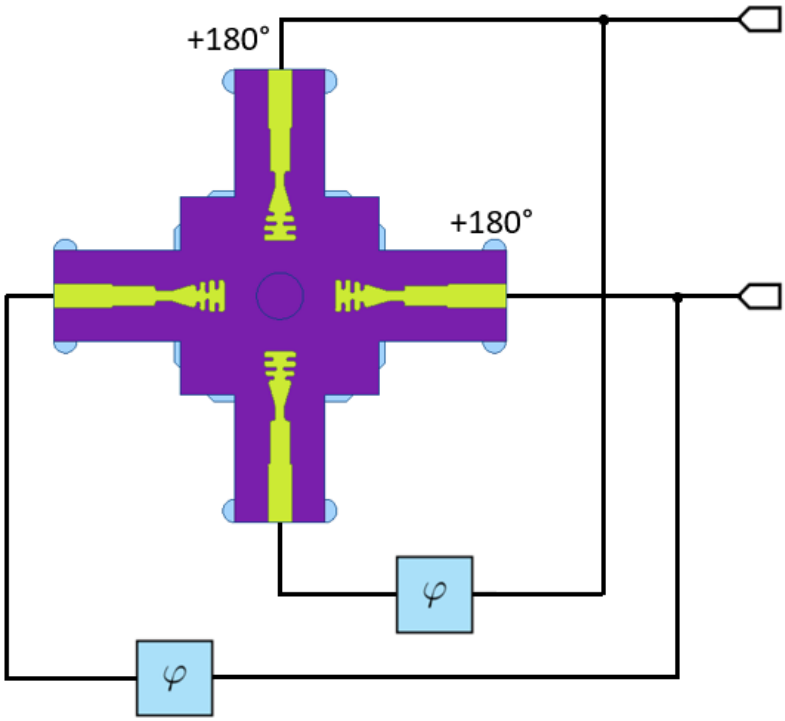

Figure 4.7: Scheme of the signals-per-polarization-recombination model, performed using AWR. One branch for each polarization is phase shifted by 180 degrees. The other branch has a variable phase shift of φ degrees, which is set to zero for all the results in this chapter.

tion in every figure of merit, and diminish them was part of the criteria considered during optimization. Resonant modes are claimed to be trapped near the tuning stub of this design and similar reported structures [16]. Resonances are also attributed to asymmetries in the design, but it would only be relevant to this design once it is manufactured [18]. Resonances can be harmful because, depending their incidence to cross-polarization, the digital back end might not be able to calibrate them [8].

The previous simulations were made considering the model of figure 4.1. These simulations do not consider the recombination of signals per polarization. Signal recombination has to be done by post processing the data obtained from HFSS. To do so, the scattering matrix for each simulated point in frequency is exported to National Instruments AWR software. Then, a recombination of signals is forced by connecting the outputs from each polarization to a single port, adding a phase shift of 180 degrees to one branch. This is necessary to constructively sum the signals. Otherwise they would cancel each other, since they exit the OMT's polarization splitter with a phase delay of 180 degrees between them. This recombination of signals exemplifies the best case scenario of the digital OMT performance, or *ideal OMT implementation* [8]. Figure 4.7 shows a diagram of how the recombined signals analyses were made.

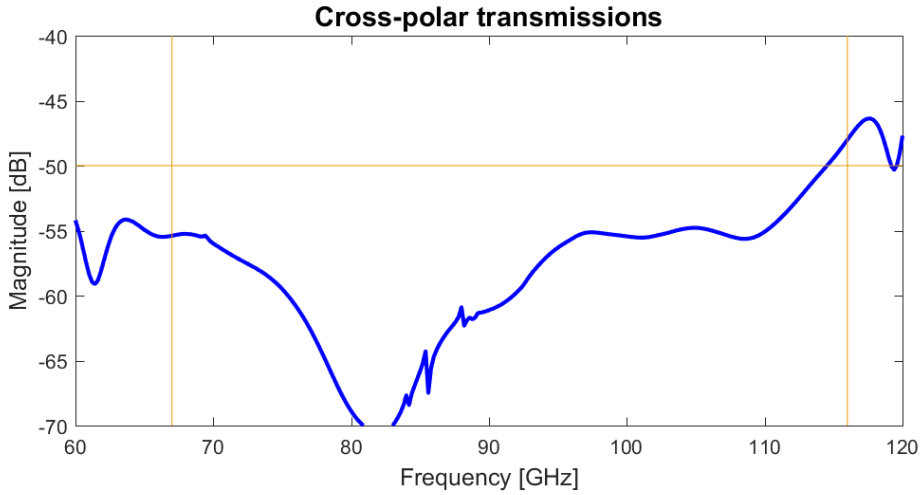

Figure 4.8: Cross-polar transmissions of the PV OMT with signal recombination.

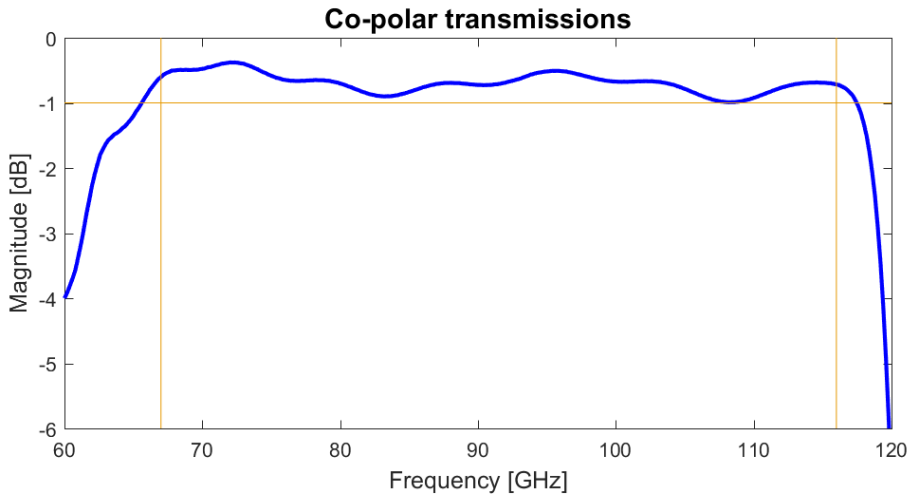

Figure 4.9: Co-polar transmissions of the PV OMT with signal recombination.

The isolation simulation of figure 4.5 was obtained by the previously stated procedure, following the scheme in figure 4.7. Simulations of cross-polar and co-polar transmissions are also repeated following the signal-recombination-procedure. Figure 4.8 shows the recombined-cross-polarization results and figure 4.9 shows the analogous results for co-polarization transmissions. With these figures of merit, a fair comparison regarding cross-polarization and desired transmissions can now be established between the PV OMT and other reported designs. Cross-polar transmissions are now worse than -50 dB only above 114 GHz. Co-polar transmissions after recombination are better than -1 dB.

4.2 PV LO Splitter

The simulated LO splitter model for the Planar Version is shown in figure 4.10. Probes are again seen from the bottom of the model (figure 4.10a), so that they lie on the same plane as the OMT probes once assembled together. From the isometric view of the model (figure 4.10b), the adaptation section from WR19 waveguide to the splitter is seen. The splitter, as

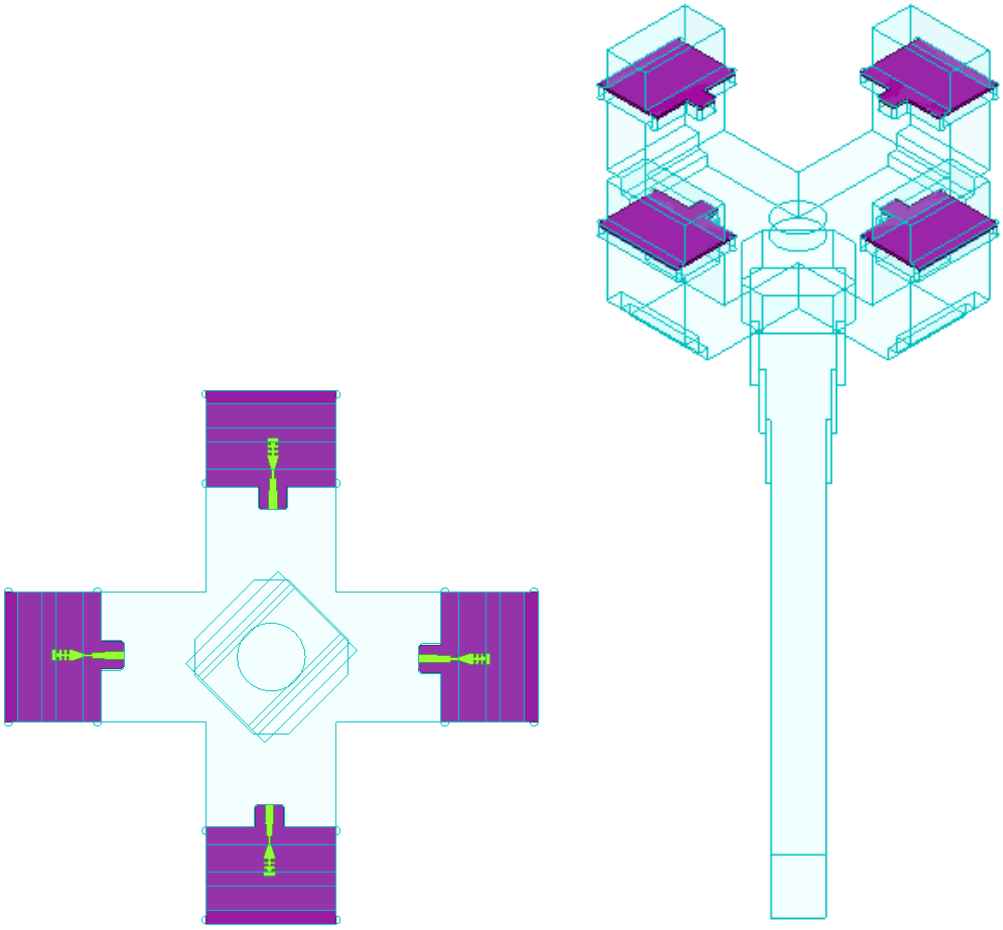

(a) Bottom View. (b) Isometric view.

Figure 4.10: Views of the designed local oscillator splitter for the Planar Version. (a) Probes are seen from the bottom of the model. This choice is made to ease the assembly of the receiver. (b) Dimensions are based on the WR19 standard for waveguides, except for the adapting section between the input waveguide and the turnstile junction of the splitter.

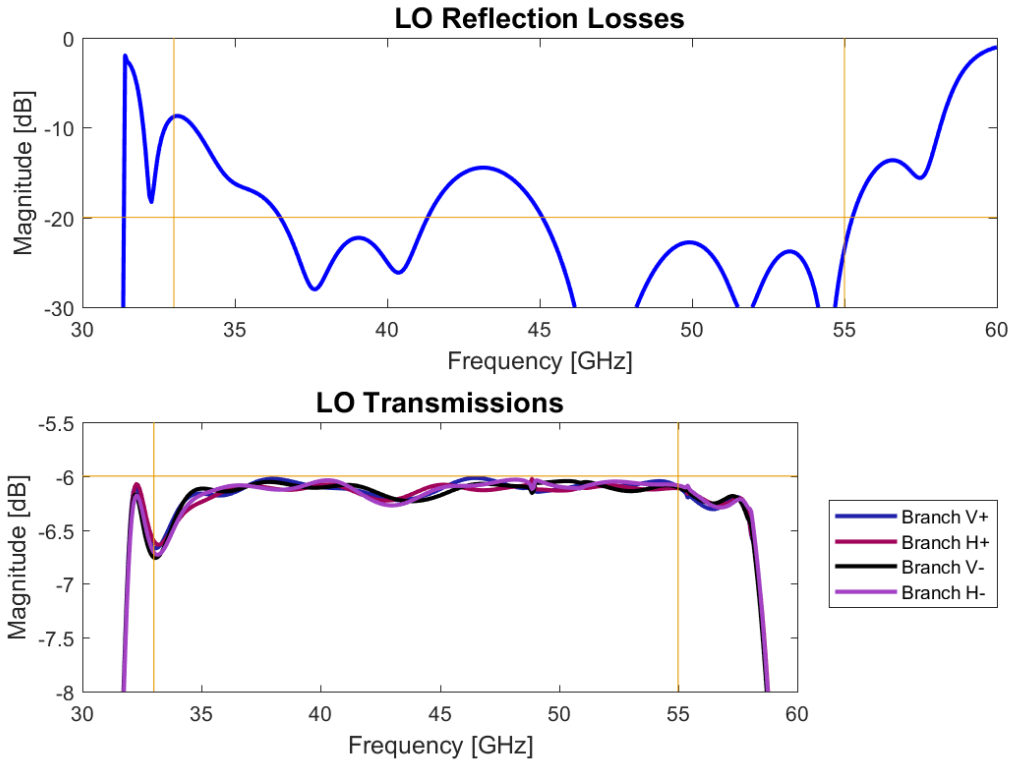

Figure 4.11: Reflection losses at the input and transmissions to every branch of the PV LO splitter.

well as the OMT, has a tuning stub on its center. The frequency band of interest for this design is the 33 - 55 GHz. However, it is to consider that the lower portion of the frequency band is close to the WR19 waveguide cutoff frequency.

Reflections at the input and transmissions to every branch of the PV splitter are shown in figure 4.11. Regarding the reflections, there are peaks that surpass the -20 dB reference line, reaching -15 dB at 44 GHz and -10 dB at 33 GHz. Transmissions are better than -7 dB along the band. Power is divided into four, so transmissions cannot be better than -6 dB as a theoretical limit, marked with a reference line.

4.3 PV Front End

A complete view of the receiver is shown in figure 4.12. From the bottom of the model (figure 4.12a), OMT and splitter probes can be seen at each side of the MMIC mixers. Additional microstrip lines connect the I/Q outputs from the mixers to MCX coaxial connectors, through which the receiver is meant to be connected with the back end. An isometric view (figure 4.12b) is useful to show the depth of the MCX connectors as compared to the OMT and splitter. Connectors mean a big portion of the overall front end's footprint. A detail of the coaxial connectors is shown in figures 4.12c and 4.12d. These are panel connectors, so they are screwed into the block that contains the electronics. Physical contact must be assured between the tip of the connector and the microstrip line once mounted together.

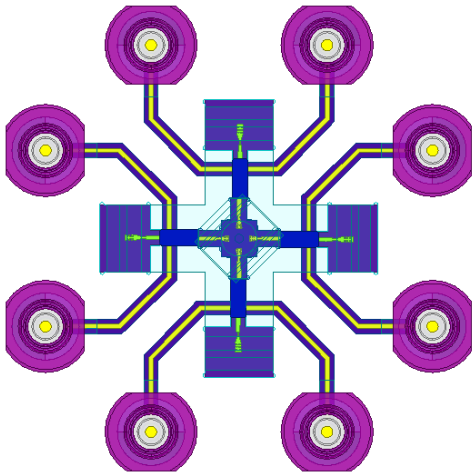

(a) Bottom view.

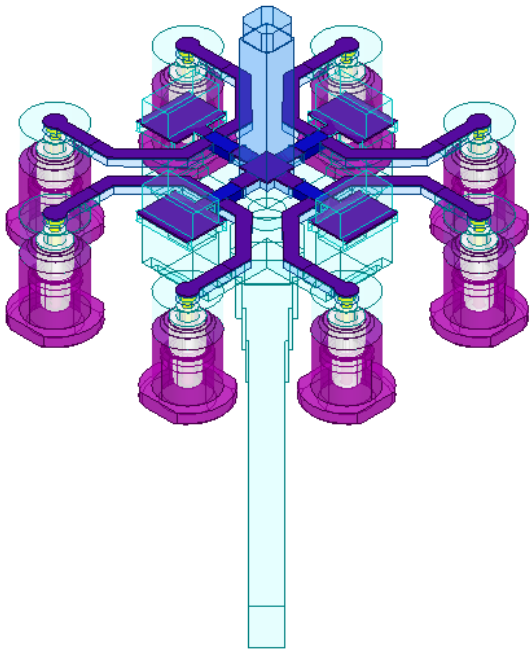

(b) Isometric view.

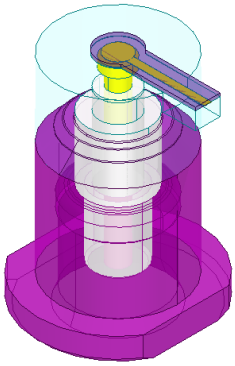

(c) 3D model of MCX connector. Obtained from manufacturer.

(d) Photograph of the considered coaxial connector.

Figure 4.12: Views of the front end electronics for the Planar Version. It contains the OMT, local oscillator splitter, MMIC mixers, MCX coaxial connectors and microstrips for I/Q signals. Air confined by waveguides is shown in blue transparent tones. Substrates are purple, probes and coaxial pins are yellow. Cavities for MMIC mixers are represented in solid blue. MCX connectors' mount is shown in transparent violet, and the teflon substrates are white. (a) Bottom view is shown so that probes and microstrips can be seen. They lie aligned on one plane. (b) Isometric view of the receiver. From this angle of the model it can be seen how conduction between I/Q microstrip lines and MCX connectors is achieved. The connector is meant to be screwed from the bottom of the mechanical block that will contain this front end towards the microstrip lines. This way, the pin of the connector will push the microstrip line against the substrate, ensuring a good electrical contact. (c) MCX connector model with a fragment of microstrip line. (d) MCX connector photograph. Source: *https://cl.rsdelivers.com/product/radiall/r113553000w/conector-coaxial-radiall-r113553000w-hembra-recta/3071128.*

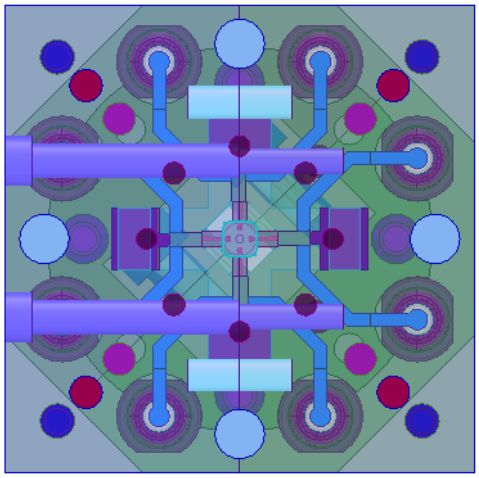

(a) Top view.

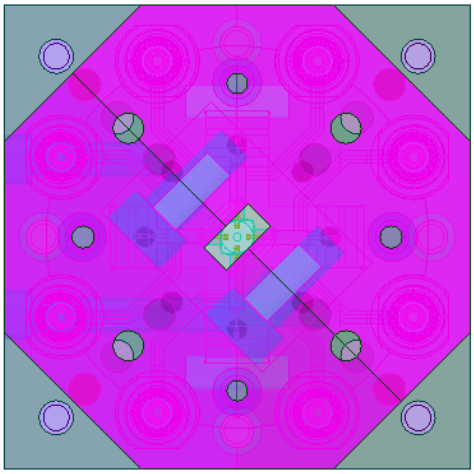

(b) Bottom view.

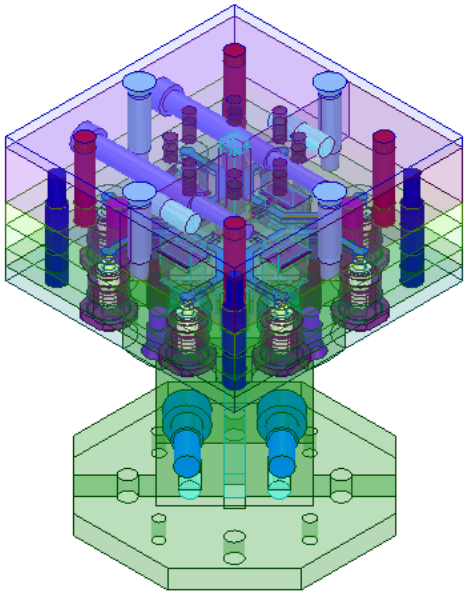

(c) Isometric View.

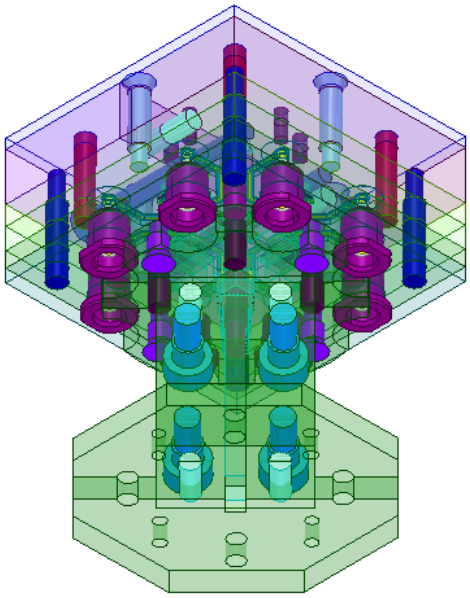

(d) Bottom-Isometric View.

Figure 4.13: Mechanical design of the PV receiver. All the electronics are enclosed by metallic sheets and blocks that are assembled together with screws together with alignment bolts. (a) Top view of the mechanical design. The profile is square with edges long 36 mm. Circles across the diagonals represent alignment bolts, while circles across the centres of the edges are mostly screws. (b) Bottom view of the model. The octagonal pink shape is the WR19 waveguide flange, which is a major size restriction to this design. The footprint could not be smaller than this flange because it is a piece of standard dimension and is required for the operation of the front end. (c) Isometric view. (d) Isometric view from the bottom of the front end. Most of the parts that build this receiver are metallic sheets, among fewer blocks of different shapes.

4.4 Mechanical design

The mechanical model for the plan of this receiver is shown in figure 4.13. Its footprint is a 36×36 mm square. Its section is as large as the WR19 waveguide flange required for the LO splitter. The receiver's footprint, as seen from figures 4.13a and 4.13b, is the most important dimension of this design as a mechanical block. The depth or height of the receiver, inferred from figures 4.13c and 4.13d, is not determining whether or not the receiver is suitable to be implemented as a focal plane array.

4.5 Discussion

The simulation results for this version of the OMT (figures 4.3 to 4.9) meet the objectives set in section 1.6, except for the reflection losses at the input. Operational bandwidth is 7 GHz short at the lower end to completely cover the 67 - 116 GHz band. It would be desirable a better performance at lower frequencies for the LO splitter, reaching reflections closer to -20 dB near the cutoff frequency of the WR19 waveguide. However, the designed electronic structures for this front end are simpler to fabricate as compared to those of figure 1.1. The footprint of this receiver makes it feasible for being implemented as a focal plane array.

Size and fabrication-complexity reduction are achieved in this design. From this point on, a new hypothesis emerges, particularly with regard to the OMT. It should be possible to improve electromagnetic performance in exchange for a more complex mechanical design. Additionally, moving the probes away from the turnstile should improve the cross-polar figure of merit for the OMT. These hypotheses lead to the design of another version of the front end, considering potentially more complex structures.

4.6 Summary and Conclusions

The first version of the OMT design is presented together with other required elements to build a front end for a radio astronomy receiver. Simulation results are shown for the main figures of merit. Fractional bandwidth is of 44.5%, cross-polarization transmissions as well as isolation lie under the -50 dB threshold, and co-polar transmissions are better than -1 dB. A procedure to obtain figures of merit comparable with those of other OMT via post-processing is explained. The mechanical design is introduced. Electromagnetic results together with the resulting mechanical design point out that the design is perfectible at the cost of some trade-offs. To develop another front end, fabrication complexity is expected to increase if the electromagnetic performance is to be improved.

Chapter 5

Semi-Turnstile Version of OMT and Front End

Observations made to the Planar Version of the designed front end, and particularly on the PV OMT, motivate the design of a second version. The main objective of this second design is to improve the electromagnetic performance of the Planar Version, especially the reflection losses at the input. Reflections of the PV OMT were insufficient to completely cover the ALMA Band 2+3. In this version, it is assumed that the fabrication complexity will increase, but the objective of making it feasible for developing a focal plane array is maintained. As well as in the previous chapter, structures of this second design will be referred to as *Semi-Turnstile Version* or just *STV*. Even if planar structures are considered in this design as well, the term planar is not used in its name to differentiate it from the previous design.

5.1 STV OMT

Design and simulation results of the Semi-Turnstile Version of the OMT are reviewed in this section.

5.1.1 OMT Design

The design for the STV OMT originates from the waveguide OMT designed in [17]. The three dimensional model is shown in figure 5.1, courtesy of Ignacio Barrueto who provided his model and allowed its edition to create a new OMT.

The OMTs to be designed in this thesis do not perform signal recombination, leaving that operation to the back end [8]. This way, the OMT of figure 5.1 can be truncated, and the power combiners for each polarization are removed from this the design. Only one waveguide bend was considered to be required to make a planar OMT, reducing as much as possible its footprint. The resulting model is shown in figure 5.2. Transitions to microstrip are placed at the end of each waveguide branch and lie on an parallel plane to the input astronomical signal. Waveguides in this design are custom-sized and are narrower than the

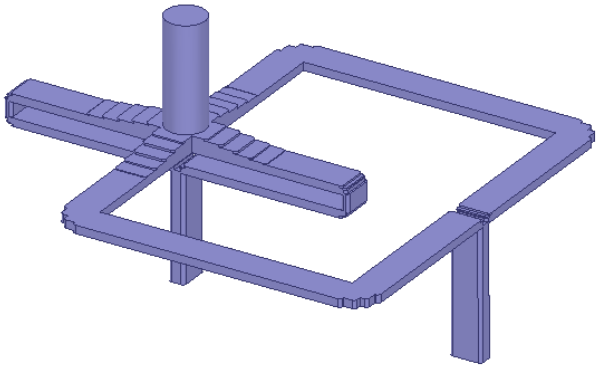

Figure 5.1: Waveguide OMT operating in the 67 - 116 GHz band. Source: *Ms. C. Thesis, Ignacio Barrueto.*

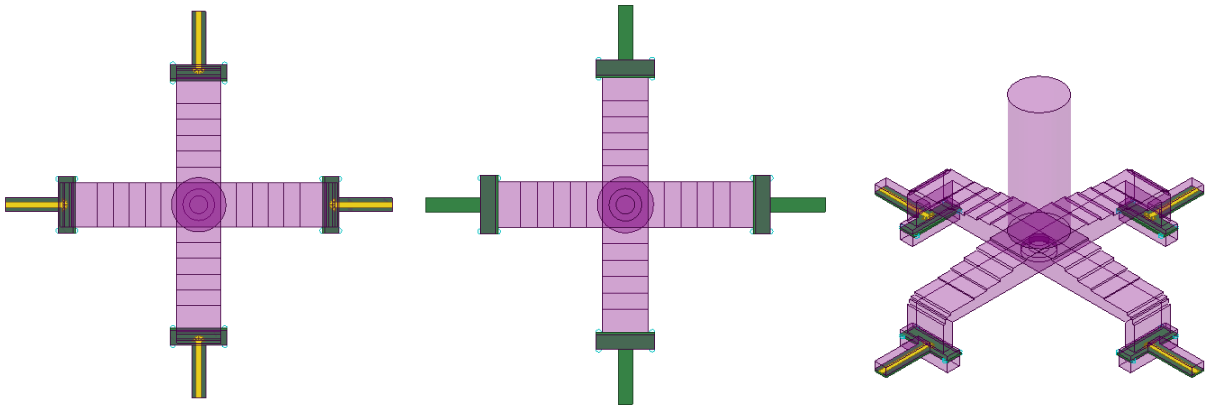

(a) Top View. (b) Bottom view. (c) Isometric view.

Figure 5.2: Different views of the Semi-Turnstile Version of the OMT. Air regions confined by waveguides are rendered in purple. The substrates are green, and microstrip probes are yellow. (a) Top view. The astronomical signal enters the OMT through the purple circular waveguide. Probes are seen from the top of the model. (b) Bottom view. (c) Isometric view of the OMT.

WR10 standard, yielding a lower impedance of the lines.

The microstrip probe designed for this OMT is shown in figure 5.3. Its dendritic shape is based on the probe reported in [48]. It is based on metamaterial structures and is proved to provide wideband performance in media transitions. Different to the probe shown in figure 4.2 for the PV OMT, this probe required no impedance matching section.

5.1.2 STV OMT simulation results

Simulations are performed using Ansys HFSS. Reflection losses are shown in figure 5.4. Operational bandwidth is equal to 54% and the ALMA Band 2+3 is completely covered. Cross-polar transmissions (figure 5.5) are lower than -110 dB, exceeding by orders of magnitude the goal set in section 1.6. Isolation results are shown in figure 5.6, showing resonances around

Figure 5.3: Detail of the probe designed for the Semi-Turnstile Version of the OMT. A metric scale is included.

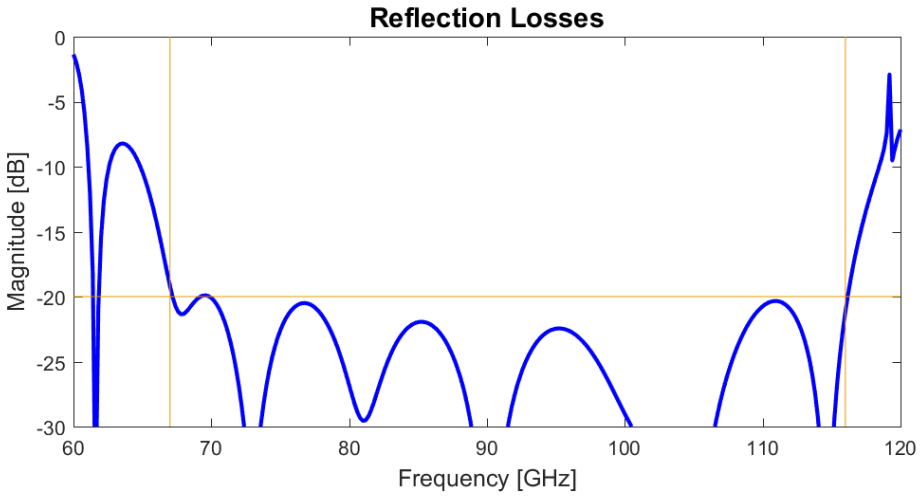

Figure 5.4: Reflections at the input of the STV OMT.

75 GHz and 110 GHz, as well as the cross-polar graph. Co-polar transmissions, shown in figure 5.7, are better than -4 dB for all the band of interest. Transmissions cannot be better than -3 dB due to power splitting into two branches of the OMT for each polarization.

The figure of isolation was obtained by following the same scheme of figure 4.7. Simulations of cross-polar and co-polar transmissions are repeated after signal recombination via post-processing using National Instruments AWR software. This is done with the objective to make fair comparisons between this design and reported OMTs that physically perform signal recombination. Recombined cross-polar transmissions (figure 5.8) are now better than -120 dB for the entire band, while recombined co-polar transmissions are better than -1.2 dB.

5.2 STV LO Splitter

The designed LO splitter for the Semi-Turnstile Version is shown in figure 5.10. Microstrip probes are seen from the top of the model (figure 5.10a). Probes are the same used for the STV OMT and shown in figure 5.3, with dimensions adjusted to operate at the 33 - 55 GHz frequency band. The splitter design is also based on the OMT in figure 5.1 designed by Ignacio Barrueto. From the isometric view of the designed model (figure 5.10b), a turnstile

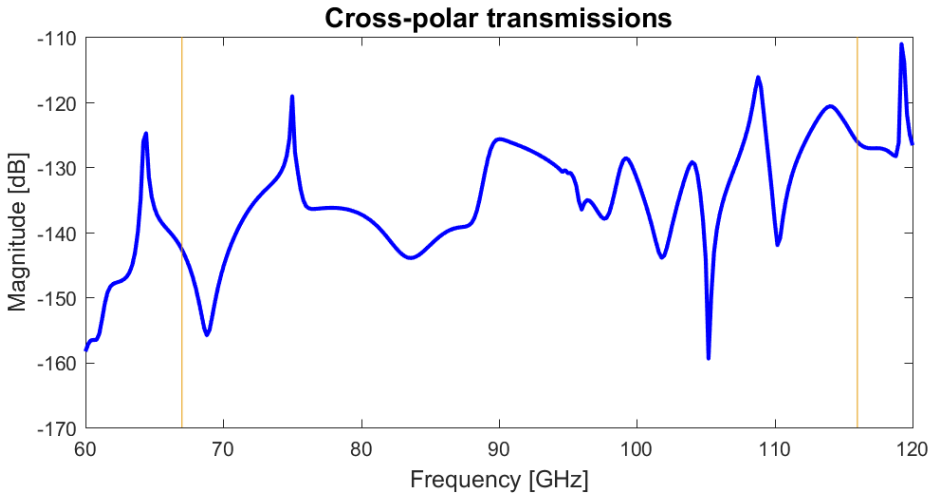

Figure 5.5: Cross-polar transmissions of the STV OMT.

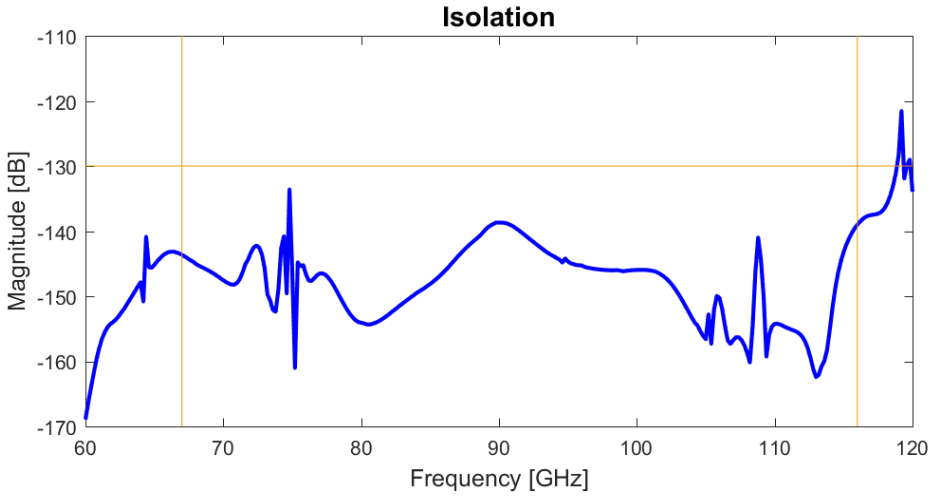

Figure 5.6: Isolation between polarization output ports of the STV OMT.

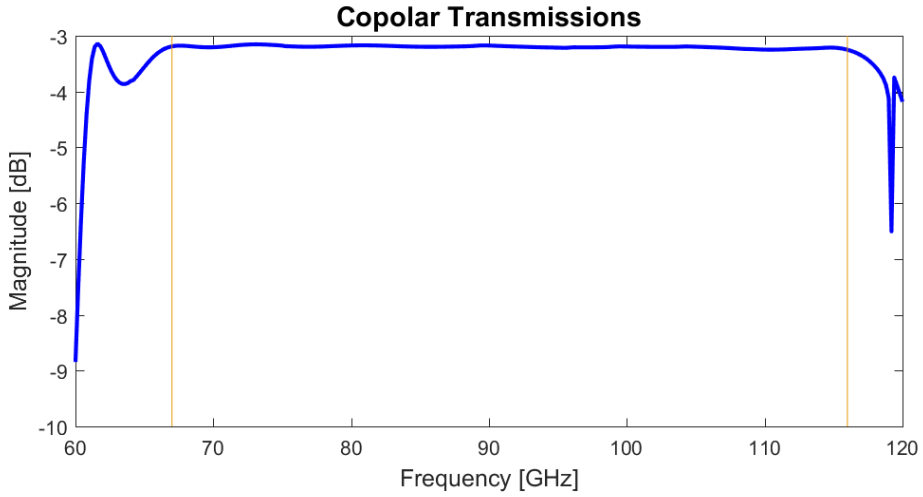

Figure 5.7: Co-polar transmissions of the STV OMT.

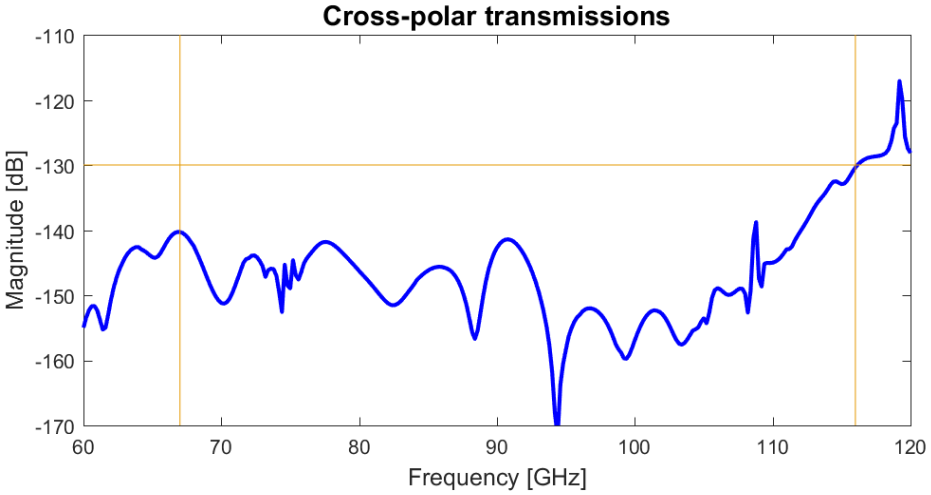

Figure 5.8: Cross-polar transmissions of the STV OMT after signal recombination.

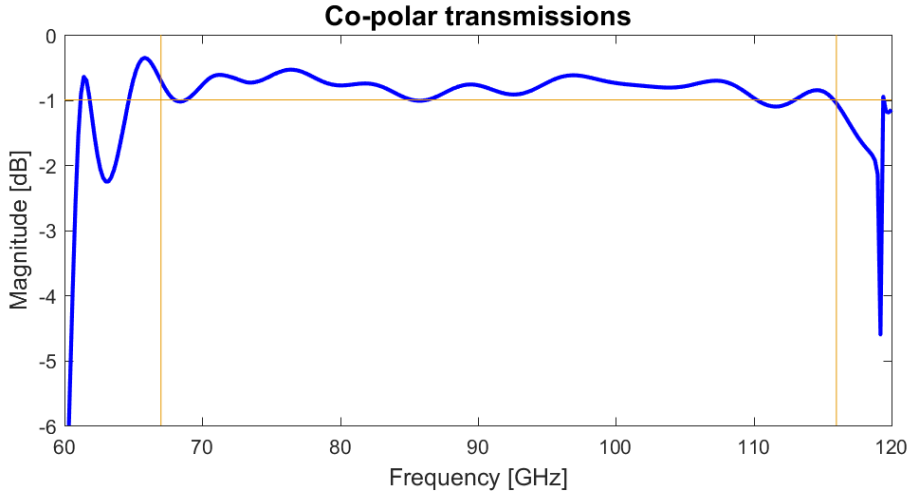

Figure 5.9: Co-polar transmissions of the STV OMT after signal recombination.

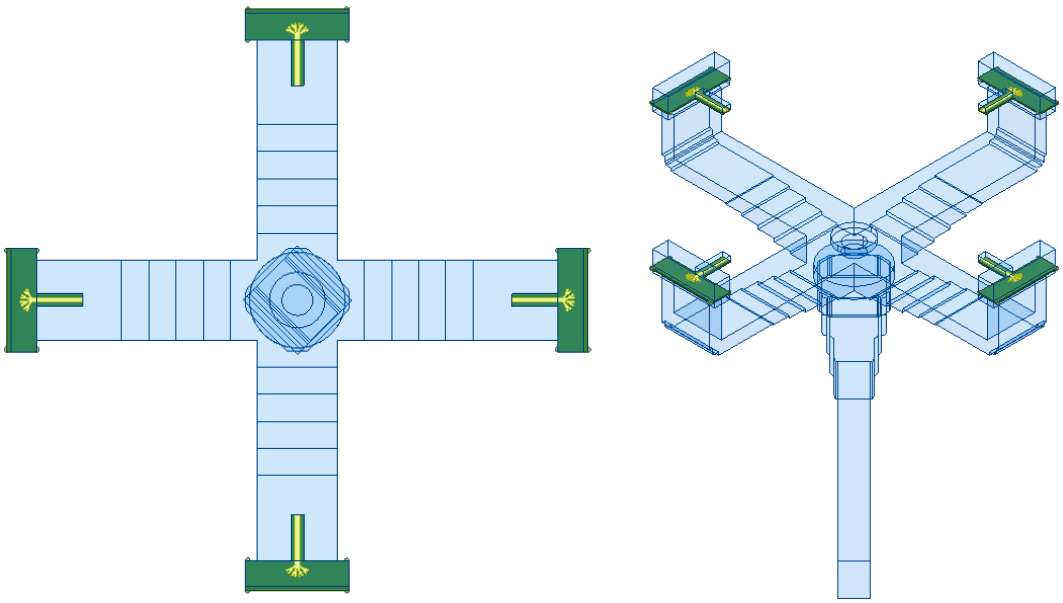

(a) Top View. (b) Isometric view.

Figure 5.10: Views of the designed local oscillator splitter for the Semi-Turnstile Version. (a) Probes are seen from the top of the model. (b) The input waveguide for the local oscillator tone is a standard WR19 waveguide. The rest of the waveguides of this model are custom sized.

junction is seen at the center of the model. A staggered transition from rectangular waveguide to the turnstile junction is included.

Reflections at the input of the splitter are shown in figure 5.11, together with the transmissions to each microstrip probe. Reflections have peaks that surpass the -20 dB reference line across the 35 - 55 GHz band, but do not reach -15 dB. RHowever, reflections at 33 GHz are of -10 dB. Transmissions are better than -6.5 dB between 35 and 55 GHz, and closer to -7 dB towards 33 GHz. Power is divided into four, thus the theoretical limit for these transmissions is -6 dB.

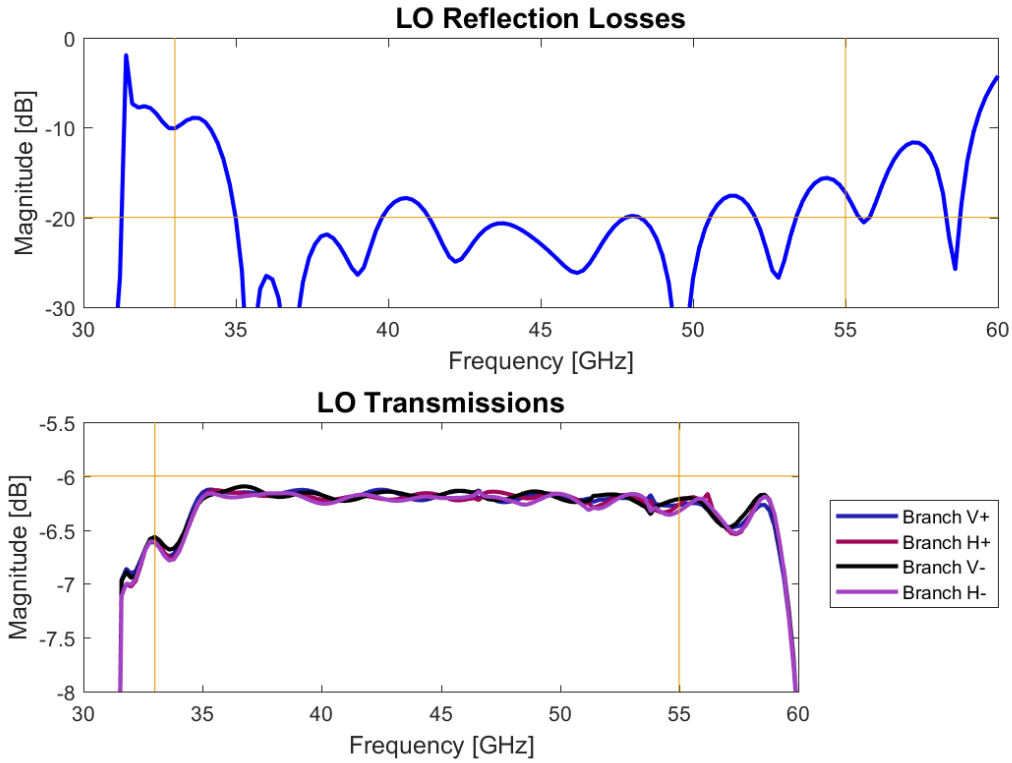

Figure 5.11: Reflection losses at the input and transmissions to every branch of the STV LO splitter.

5.3 STV Front End

All the elements of the STV front end are shown in figure 5.12. Component placement follows the same order as for the Planar Version, shown in figure 4.12, but there are differences. The most important difference is that the microstrip lines are facing to the top of the model (figure 5.12a and 5.12b). This is a consequence of choosing a different connector for the mixers' outputs. The chosen connectors are through-hole coaxial MMCX type (figure 5.12d), which are smaller and are assembled differently than the MCX connectors considered for the Planar Version. These coaxial MMCX connectors also allow to make the electrical contact from the rear part of the microstrips, as shown in figure 5.12c.

5.4 Mechanical Design

The mechanical model of the STV front end is shown in figure 5.13. The metallic sheets that make it have a section of 36×36 mm as seen from either top or bottom (figures 5.13a and 5.13b). Edges of the metallic sheets fit the profile of the WR19 flange (figure 5.13b), making the STV front end a candidate to be implemented as a focal plane array regarding its size. From figures 5.13c and 5.13d it can be seen that the mechanical model is made only from metallic sheets plus the splitblock that makes the WR19 waveguide and flange.

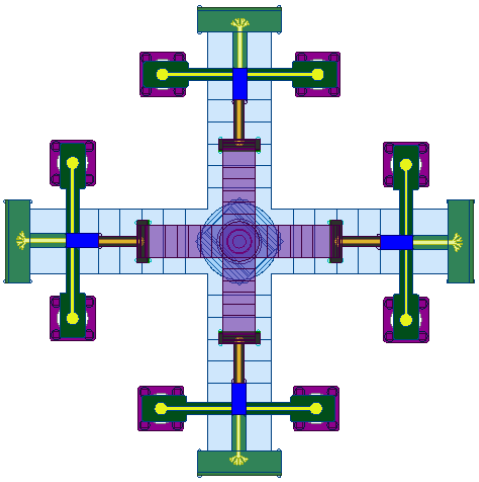

(a) Top view.

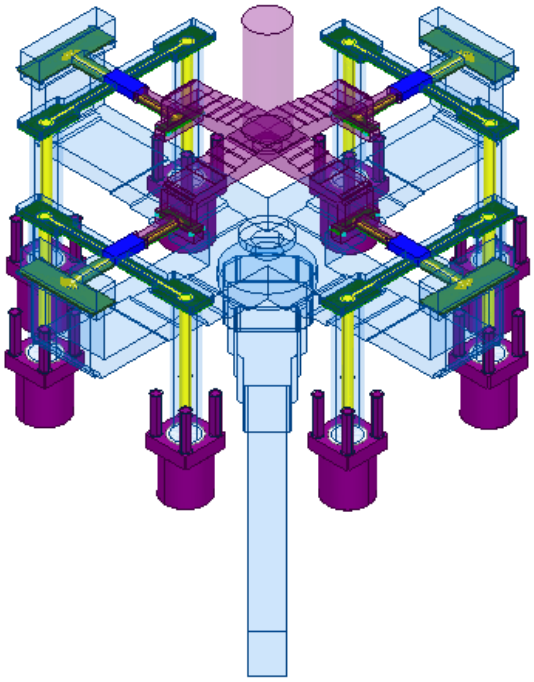

(b) Isometric view.

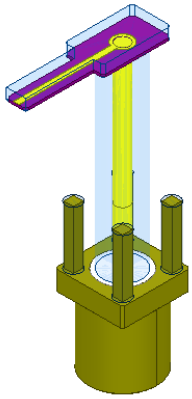

(c) 3D model of MMCX connector. Obtained from manufacturer.

(d) Photograph of the considered coaxial connector.

Figure 5.12: Views of the STV front end's electronics. The OMT is shown in transparent violet and the splitter in light blue. Substrates, microstrip lines and cavities for MMIC mixers are shown in solid green, yellow and blue respectively. Connectors considered for this model are through-hole MMCX. They are inserted from the bottom of the mechanical blocks that build this front end. The pin of the connector goes through the substrate and mixer's I/Q microstrip and is soldered. (a) Top view of the elements of the front end. (b) Isometric view. (c) MMCX connector model with the microstrip that connects to the mixer. (d) MMCX connector photograph. A longer central pin for the conector is only provided on demand by the manufacturer. Source: *https://www.mouser.cl/ProductDetail/Amphenol-RF/908-22106?qs=LgeqI7%252B1o3WnCXNTH3Bccg==*.

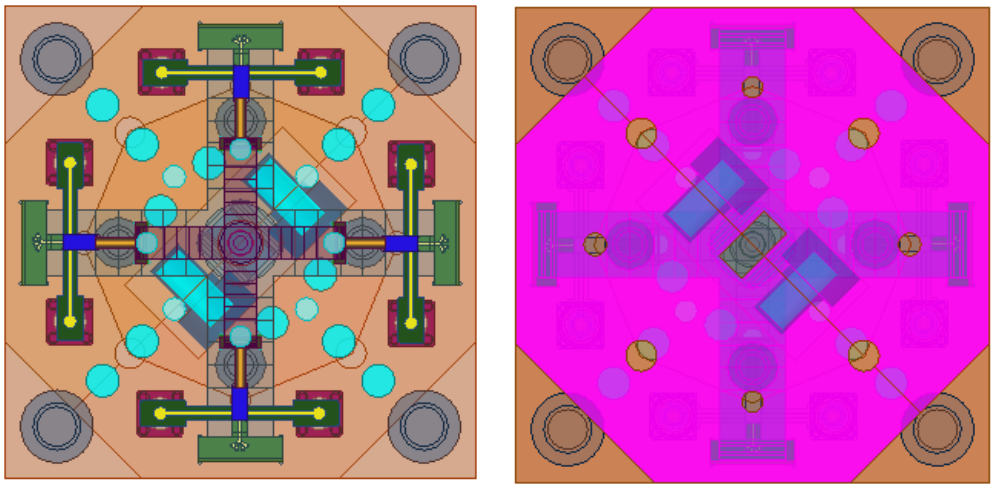

(a) Top View.

(b) Bottom view.

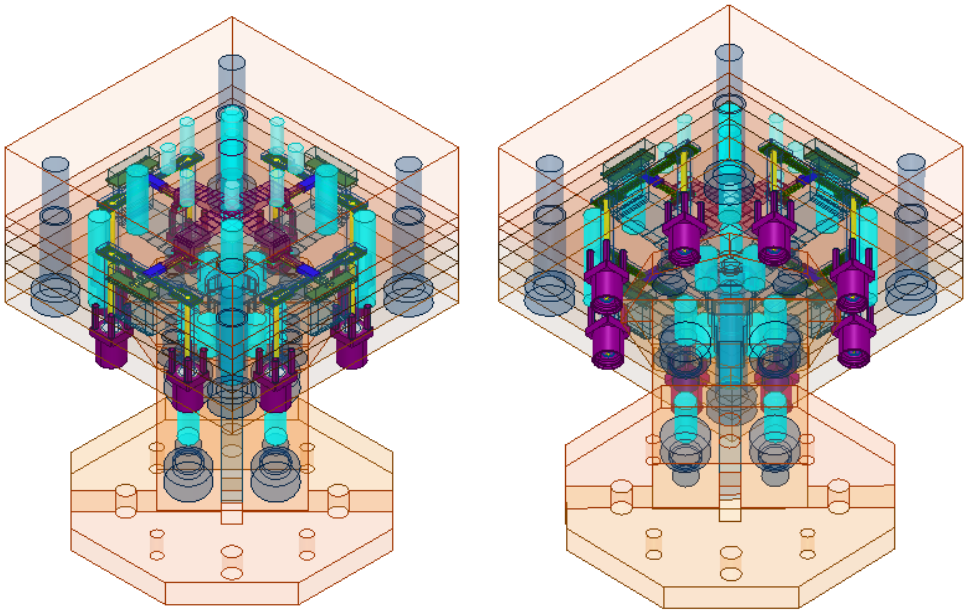

(c) Isometric view.

(d) Bottom-isometric view.

Figure 5.13: Mechanical design of the STV front end. Electronics are enclosed by metallic sheets. Screws and alignment bolts are used to hold all the pieces together. (a) Top view of the design. The profile is a square with edges long 36 mm. From this view, screws and alignment bolts are seen across the diagonals of the block. (b) Bottom view. The highlighted pink octagon is the WR19 waveguide flange considered for the LO. (c) Isometric view of the mechanical design. (d) Isometric view from the bottom of the front end.

5.5 Discussion

The reflection losses of the STV OMT, shown in figure 5.4, accomplish the objective to cover the ALMA band 2+3. Simulations of cross-polar transmissions, isolation and co-polar transmissions surpass the objectives set in section 1.6. In the case of cross-polar and isolation the objectives are exceed by more than 60 dB, giving large margin for performance worsening due to manufacturing errors. The hypothesis of improving cross-polar is fulfilled by moving the probes away from the turnstile junction. The LO splitter shows good performance between 35 and 55 GHz. It would be desirable to show better reflections and transmissions near 33 GHz.

Both the OMT and the LO splitter of the Semi-Turnstile Version are based on the OMT designed in [17]. Therefore, fabrication complexity is not necessarily reduced while comparing the OMTs from table 1.1 to the structures shown in this chapter. However, size reduction is achieved to the point that the proposed front end is feasible for developing focal plane arrays.

5.6 Summary and Conclusions

The second version of the front end is presented in this chapter. Designs of the OMT and LO splitter are strongly based on the OMT reported in [17] while adding dendritic transitions to microstrip lines [48]. Simulation results meet all the objectives set prior to the design. Operating bandwidth reached 54%, with cross-polarization transmissions and isolation below -130 dB, and co-polar transmissions of -1 dB. Mechanical design considers the manufacturing of more detailed features as compared to the Planar Version of the front end. Thus, fabrication complexity is not necessarily reduced. However, the size of the STV OMT as compared to the waveguide OMT that originates this design is considerably reduced.

Chapter 6

Analysis of Results

In this chapter, further analysis of the simulation results shown in chapters 4 and 5 is carried out. The emphasis is on the results of the OMTs, being the most critical structure inside the designed front ends.

The level of cross-polarization is important to evaluate the performance of an OMT because it means the quality of the polarization split that the OMT accomplishes. For the proposed receiver in this work, signal recombination is performed in the back end. As a consequence of this feature, cross-polar levels must be maintained under a threshold that the back end can use. Results of the proposed designs are compared to reported OMTs' results, and a cross-polarization tolerance analysis is performed simulating different loads connected to the OMT.

Other analyses are included in this chapter. An isolation tolerance analysis is carried out considering phase imbalances between the V and H polarization pairs of branches of the OMTs. A fabrication analysis is carried out and a study on the current distribution on the microstrip probes of the OMTs is included.

6.1 Cross-polarization analysis

6.1.1 Comparison between OMTs

Given the simulation results for the reflection losses and cross-polar transmissions of the PV and STV OMTs, it is simple to compare them to other reported OMTs. In figure 6.1, reported OMTs from table 1.1 are plotted in a fractional bandwidth versus rejection to cross-polarization space. Not every reported OMT is included in the graph because some reports didn't include simulation results. The values for the x-axis are the absolute value of the cross-polar figure of merit. Thus, for a given bandwidth, an OMT with a higher value along the x-axis is better than one closer to the origin. A dotted line breaks up the plane separating those OMTs whose performance privilege the fractional bandwidth over the cross-polar rejection.

From figure 6.1, and by not considering the STV OMT, the four best OMTs regarding

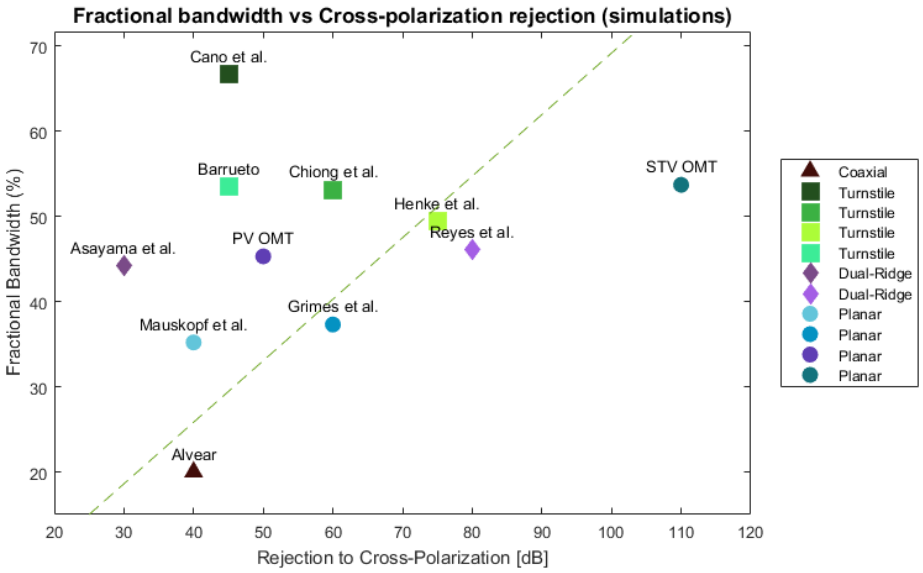

Figure 6.1: Comparison of the simulated fractional bandwidth and cross-polar transmissions for reported OMTs. Over each point of the graph, the main author is mentioned. On the legend, the type of OMT is shown.

fractional bandwidth are waveguide based [10, 15, 16, 17]. They are followed by a dual-ridge OMT [12], which is the best regarding cross-polarization. Otherwise, the reported planar OMTs [23, 13] are among the worst designs regarding fractional bandwidth and [23] is among the worst considering cross-polarization as well.

The PV OMT shows a fractional bandwidth similar to both the reported dual-ridge designs [12, 22], but shows a cross-polar level around the middle between them. On the other hand, the STV OMT shows a fractional bandwidth as good as the waveguide OMTs from [16] and [17], and the best cross-polarization of the graph. Regarding fractional bandwidth, the STV OMT is only surpassed by the OMT from [15], which in turn has a figure of cross-polarization even worse than the PV OMT. In sum, a general comparison between OMTs show that both PV and STV designs have competitive performance to reported OMTs with larger footprints and more complicated structures.

6.1.2 Cross-polarization tolerance to load mismatches and imbalances

The simulation results from chapters 4 and 5 consider loads perfectly matching the output ports of the designed OMTs. However, in these designs of front ends, MMIC mixers are connected to each probe of the OMT. MMIC mixers could have different impedances associated to different desings or manufacturing differences, leading to different levels of reflections at the OMT planar ports. Furthermore, a low noise amplifier (LNA) could be connected to the probes of the OMTs in a different front end that would consider the use of an OMT designed in this work. That being said, there are different scenarios where there might be more or less reflected waves from the output ports of the OMT back into it. These internal reflections would surely degrade the performance of the OMT, especially with regard to the

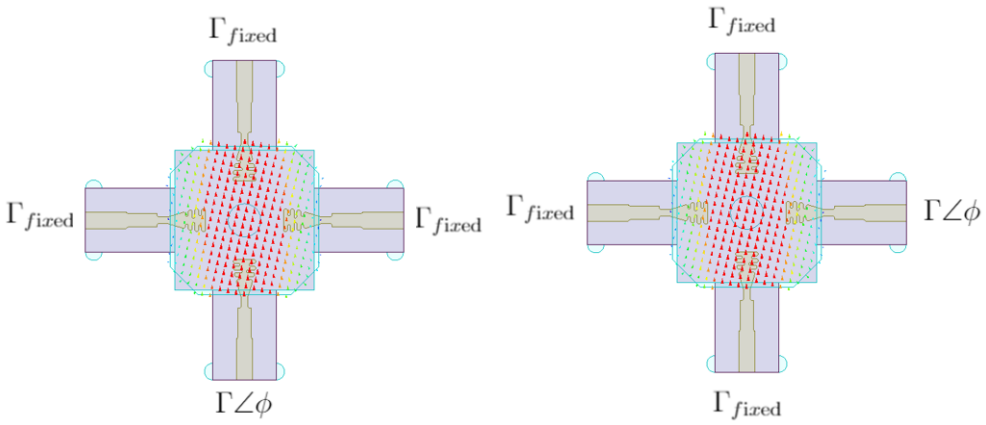

(a) Test 1.

(b) Test 2.

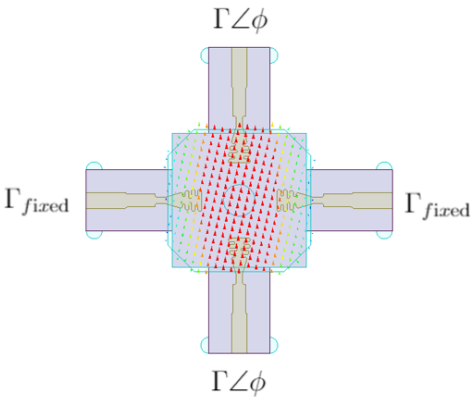

(c) Test 3.

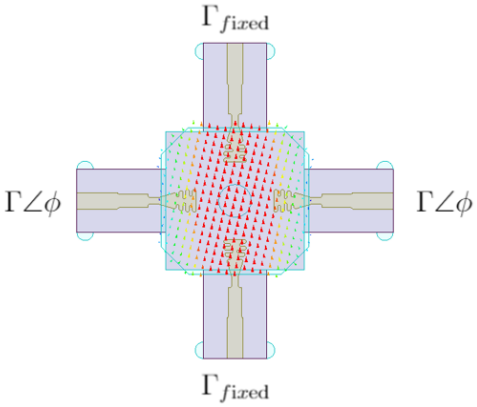

(d) Test 4.

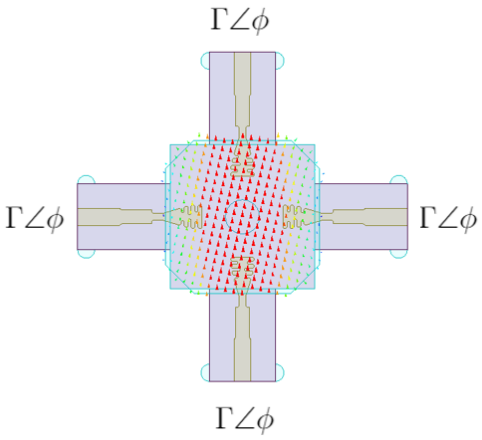

(e) Test 5.

Figure 6.2: Graphic description of tests carried out to evaluate impairment of the cross-polarization figure of merit by connecting imperfectly-matching-loads at the planar ports of the OMT. Vertical red arrows in each figure indicate the orientation of the excitation of the simulations. For all tests, cross-polarization is evaluated as the transmissions to the horizontal probes while a vertical excitation enters the OMT. In each test, the reflection coefficient varies at (a) one co-polar port; (b) one cross-polar port; (c) both co-polar ports; (d) both cross-polar ports; (e) all ports of the OMT. Without loss of generality, the graphic example is shown using only a figure of the PV OMT. Tests for the STV OMT are analogous.

Scenario	Γ_{fixed} [dB]	Γ_{min} [dB]	Γ_{max} [dB]	ϕ [deg]
1	$-\infty$	$-\infty$	0	0 - 357.5
2	-10	-12	-8	0 - 357.5
3	-6	-7	-5	0 - 357.5
4	-3	-3.5	-2.5	0 - 357.5

Table 6.1: Definition of scenarios for the cross-polarization tests. Sets of fixed and variable values for the reflection coefficients Γ at the ports of the OMTs vary from one scenario to another.

cross-polarization.

A set of different tests were carried out to evaluate the variation of the OMTs' cross-polarization levels when different loads are connected to their ports. Five tests were defined and are described in figure 6.2. If Γ_{fixed} is written next to a port, the reflection coefficient is set to a single value for that port in that test. Where $\Gamma\angle\phi$ is written, the reflection coefficient in that port varies in magnitude and phase for that test. Tests 1 and 2 (figures 6.2a and 6.2b) exemplify a dramatic case where one load differs drastically from the others. However, loads to be used are expected to be comparable to each other. Therefore, different symmetric tests are carried out as well (figures 6.2c, 6.2d and 6.2e).

The fixed values and the ranges where reflection coefficients vary change between different scenarios that represent different loads connected to the OMT. The values for the fixed and variable ports in the different scenarios are shown in table 6.1. These scenarios try to emulate the connection of different loads, depending on the reflections set at the ports of the OMT:

- Scenario 1: any load, as an overview of the behavior of the OMT against mismatched ports.
- Scenario 2: the connection of an MMIC mixer.
- Scenario 3: the connection of an LNA.
- Scenario 4: the connection of an LNA with poor reflections at its input.

A total of 20 tests are performed for each designed OMT. Results are shown in Appendix A for the PV OMT and in Appendix B for the STV OMT. Figures have reflection coefficient values (Γ) in the vertical axis and phase values (ϕ) in the horizontal axis, defining a $\Gamma - \phi$ space. Plotted are the contours of the regions of reflection coefficients ($\Gamma\angle\phi$) values that yield a certain cross-polarization value for each test, indicated on each curve. The area under each curve corresponds to the cross-polarization transmissions indicated on each contour line. For each figure, the best cross-polar levels are plotted at the lower part of the graph.

There are patterns that can be observed from the results for either the Planar or the Semi-Turnstile versions of OMTs. Test 1 shows the most abrupt decay among the performed tests as expected. Increasing the reflections at one of the ports that would couple most of the incoming power will naturally force power to transmit towards the cross-polar ports. Additionally, in Test 1 the co-polar ports are asymmetrical. Therefore, internally reflected waves do not cancel each other due to their opposite phase, worsening the cross-polarization even further. Test 2 creates an asymmetry similar to the one of Test 1, but it implicates the

	Scenario 1	Scenario 2	Scenario 3	Scenario 4
Test 1	-25 (*)	-15	-10	-5
Test 2	-45	-45	-45	-45
Test 3	-40	-45	-45	-40
Test 4	-45	-45	-45	-45
Test 5	-40	-45	-40	-40
Figure	A.1	A.2	A.3	A.4

Table 6.2: Worst case results for the PV OMT cross-polarization analysis.
(*) Variation of Γ was restricted for this particular test in Scenario 1: $\Gamma \in [-\infty, -19]$ dB

reflection of less power than the ideal case to the cross-polar port. Therefore, detriment of the cross-polarization figure is expected to be minor to the one of Test 1.

In Test 3, the reflections from the co-polar to the cross-polar ports are minor to the ones of Test 1. This is due to the symmetry of the test. Cancellation per phase of reflected waves inside the OMT that would travel towards the cross-polar ports occurs, different to Test 1. However, standing waves into the OMT are created, which is also true for Tests 4 and 5. This way, cross-polarization levels are worsened but always in a minor amount as compared to Test 1. It is important to point out that Test 5 is the most representative test because all the connected loads are expected to be comparable to each other, regardless of whether they are all amplifiers or all mixers.

The contour lines plotted for the cross-polarization tests follow 5 dB steps for the PV OMT and 10 dB steps for the STV OMT. This is because variances of cross-polar levels are more pronounced for the STV design. The worst results for every test in every scenario are shown in table 6.2 for the PV OMT and in table 6.3 for the STV OMT. Values included in these tables are those that would contain all the plotted contour lines, thus one step worse than the plotted curves for each figure off Appendix A and B.

For both OMTs, Test 1 is the most undesirable situation and means the absolute failure of one connected load. It is to consider that, in time, Test 1 can be Test 2 and vice versa due to the rotating nature of polarized waves. The rest of the tests are encouraging. In the case of the PV OMT, cross-polarization levels do not fall into a point that the OMT is unable to be calibrated by the back end. This effect would occur at -23 dB [8]. For the STV OMT, cross-polar levels never fall from -100 dB, which in turn cannot be improved by digitally calibrating the OMT. As a conclusion, the cross-polarization performance for both OMTs is maintained usefully functional as long as the loads connected to each port have similar impedances.

6.2 Isolation analysis

The OMTs designed in this work do not perform power combination per polarization, and such task is left to the back end of the radio astronomy receiver to develop. In the back end, this operation is carried out after the digital calibration of the OMT in every frequency channel that the operating bandwidth is divided into [8]. Phase imbalances between signals

	Scenario 1	Scenario 2	Scenario 3	Scenario 4
Test 1	-50	-70	-70	-50
Test 2	-100	-105	-100	-100
Test 3	-100	-105	-110	-100
Test 4	-100	-105	-100	-100
Test 5	-100	-115	-105	-100
Figure	B.1	B.2	B.3	B.4

Table 6.3: Worst case results for the STV OMT cross-polarization analysis.

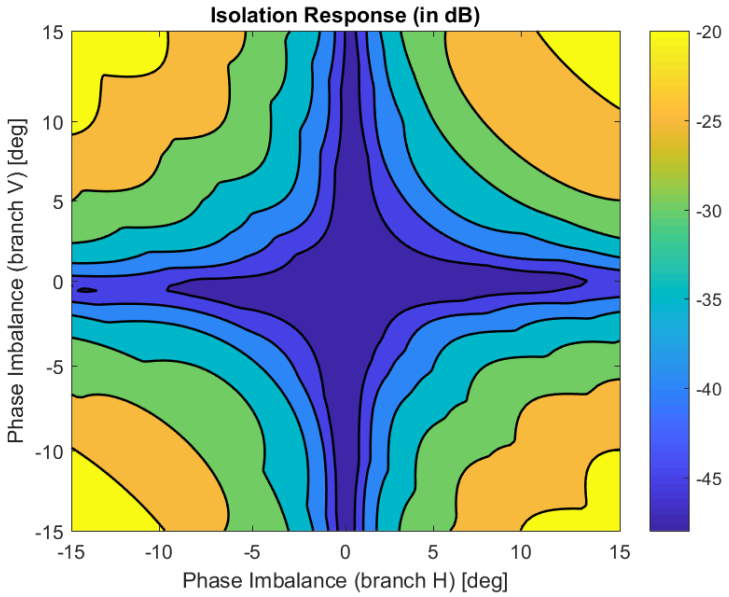

Figure 6.3: Test for isolation detriment of the PV OMT. Phase shifting is included into the digital power combination per polarization.

due to asymmetries along the interface between the front and the back end are also calibrated. However, a study is carried out on how much of this imbalance is tolerated by each OMT by itself before degrading the isolation levels drastically.

The following test consists of finding out how much phase imbalance between signals from a single polarization is tolerated by the designed OMTs. Considering figure 4.7, a phase shift of φ is varied before signal recombination. Therefore, a phase shift different to 180 degrees is maintained between signals of each polarization. This way, isolation figure of merit is worsened because interference between combined signals is not totally constructive anymore. There would be some degree of destructive interference between them.

The phase shift φ varies from -15 to 15 degrees. Results for this test applied to the PV OMT are shown in figure 6.3. The graph indicates that as long as there's a phase shift in either the vertical or horizontal polarization, isolation levels are maintained acceptable and close to the optimum of the design. When both polarizations have internal phase shifts, isolation levels decay abruptly. The STV OMT results for this test are shown in figure 6.4. Behavior of the STV OMT is identical to the PV OMT for this test. However, the worst

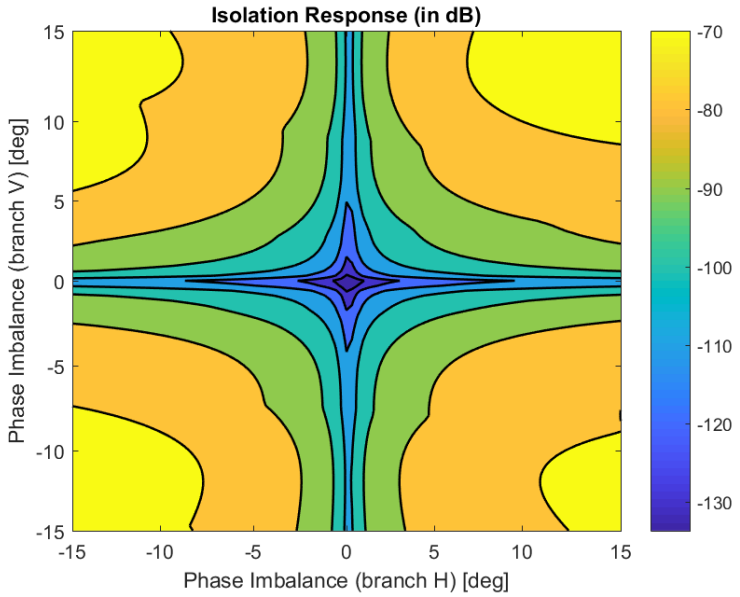

Figure 6.4: Test for isolation detriment of the STV OMT. Phase shifting is included into the digital power combination per polarization.

case scenario for the STV version is still better than the optimum for the PV version.

6.3 Fabrication tolerance analysis

The study of fabrication tolerances is a very computationally intensive process. Any combination of altered design parameters can be put together to address their effects on the figures of merit of the OMTs or LO splitters designed in this work. The PV OMT has a total of 19 parameters of design; the Semi-Turnstile Version has 30 parameters. In order to carry out this analysis in an optimum way, parameters and variations must be restricted. Otherwise, it would require an extremely large amount of computational processing to complete the analysis.

The simulated S parameters can be defined as functions of both the frequency and the geometrical parameters of the design. The partial derivatives of the S parameters against a design parameter p_k can in turn be described as a function of frequency [49],

$$S_{ij}(p_1, \ldots, p_n, f); \frac{\partial S_{ij}}{\partial p_k}(f), \tag{6.1}$$

giving the partial derivatives a quantitative meaning proportional to their magnitudes. The greater the magnitude of the partial derivative of one parameter, the more sensitive to physical variations it is. This type of analysis can be done directly in Ansys HFSS. However, for this analysis to be reliable it must be performed in several frequency points and gather as many design parameters as possible. The computational processing for this partial-derivative tolerance analysis grows exponentially as reliability of the analysis is pursued.

The tolerance analysis performed in this study followed a more conventional procedure. Variations to the nominal value of several parameters were simulated. Variations of $\pm 50\ \mu m$

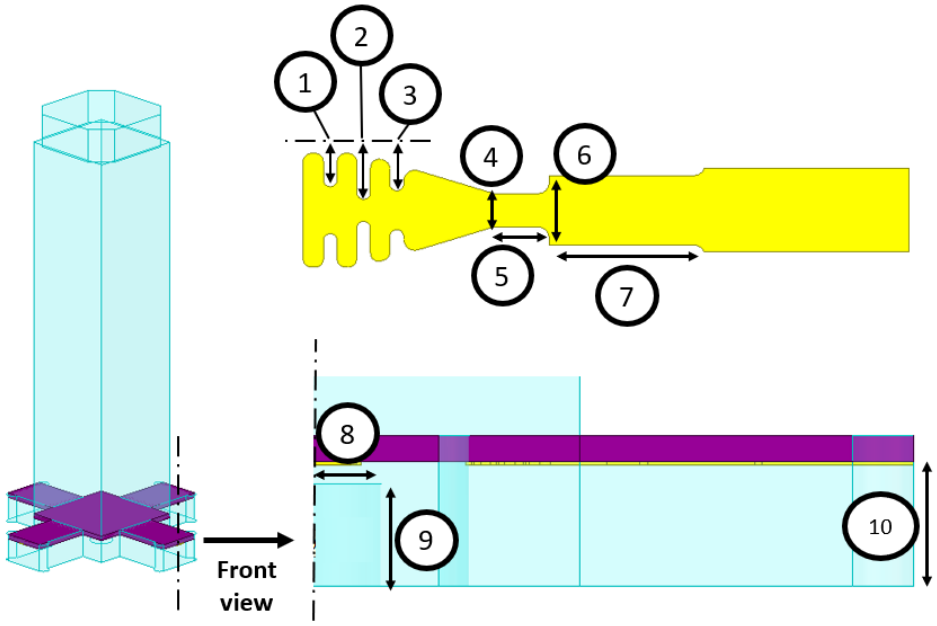

Figure 6.5: Design parameters of the PV OMT considered for the fabrication tolerance analysis. (1 - 3) Length of the engravings or slits on the radiating area of the microstrip probes; (4 - 7) Widths and lengths of the microstrip impedance matching section. (8) Radius of the tuning stub; (9) Height of the stub. (10) Height of the air backshort.

were considered for the waveguide tolerances and of $\pm 10\ \mu m$ for the microstrip tolerances, corresponding to the manufacturing error of the equipment available at the MWL. In order to reduce computational processing, the parameters included in this analysis were selected according to three criteria:

1. Those that implied greater variances, particularly to the insertion losses along the design process.
2. The last parameters to be optimized: those whose optimization managed to reach the required or optimized reflection losses and bandwidth.
3. The depth or height of the steps included for the bends or staggered sections of the designs.

The tolerance analysis is focused on the variation of reflection losses of each design (OMT and LO Splitter, PV and STV). The results of the analyses show the differences between the reflection losses of a design by increasing and decreasing a parameter according to the manufacturing error. Differences are calculated as linear power, while the results are shown in a logarithmic scale. Let us consider the parameters $p_1, ..., p_k$ of a design. On one hand, reflection losses are obtained with a parameter p_i incremented by the manufacturing error ε_{fab}, and on the other hand reflection losses are simulated by decreasing such parameter p_i by ε_{fab}. The obtained S parameters are converted to linear power, subtracted, and then turned back into dB. For all frequencies and varied parameters, the differences between these reflection losses are calculated as

$$10\log_{10}\left(10^{(S_{11}(p_1,\ldots,(p_\mathrm{i}+\varepsilon_{fab}),\ldots p_n)/10)} - 10^{(S_{11}(p_1,\ldots,(p_\mathrm{i}-\varepsilon_{fab}),\ldots p_n)/10)}\right), \tag{6.2}$$

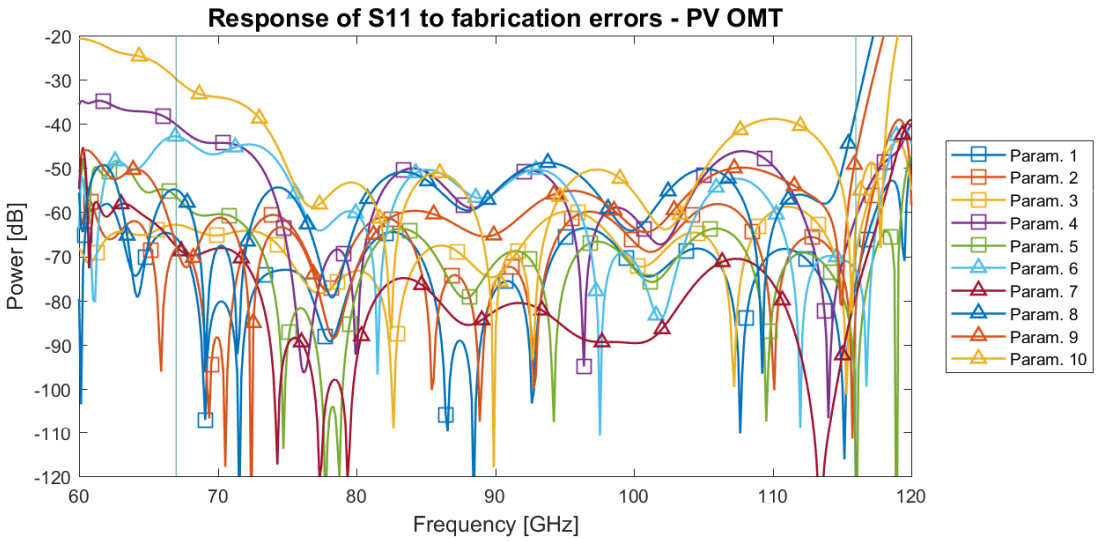

Figure 6.6: Differences of the reflection losses resulting from the tolerance analysis for the PV OMT.

and are plotted in the following subsections for each analyzed parameter of each design. By showing the differences of reflection losses using equation 6.2, intuitive-to-read plots can be generated. The higher curves account for those parameters that are more sensitive to manufacturing variations. Additionally, the percentage variations of power for each parameter can be obtained directly.

6.3.1 Tolerance analysis: PV OMT

The PV OMT design parameters to be included in the tolerance analysis are shown in figure 6.5, which were chosen by the criteria previously mentioned in this section. The results for the analysis are shown in figure 6.6. Vertical markers highlight the band of interest. Parameters of high sensitivity are number 4, 6, 8, and 10. Those parameters are, respectively, the width of each step of the microstrips impedance matching section, the radius of the OMT tuning stub, and the backshort height of the PV OMT. The greatest power differences are found towards the limits of the band of interest. In the case of the air backshort, differences of reflection losses at 67 GHz are of -30 dBW and around 110 GHz reach -40 dBW. Such values accoun for variations of less than a 5% of power across the frequency band. Figures of the variability of reflection losses for each individual parameter are shown in Appendix C.

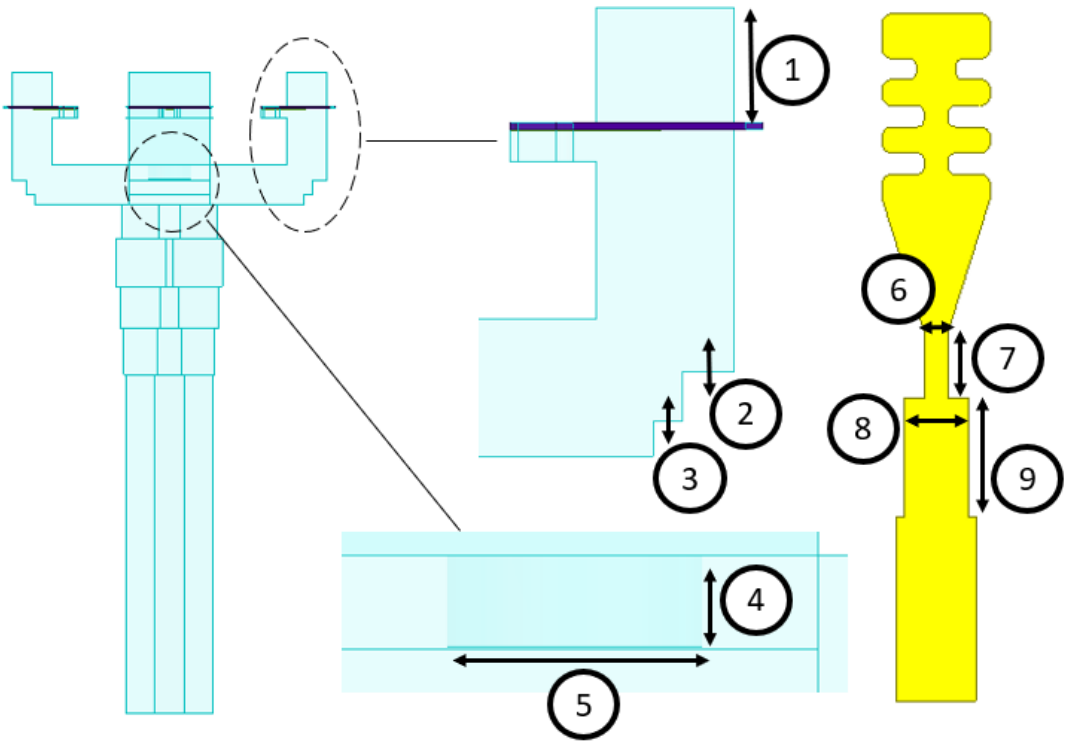

Figure 6.7: Design parameters of the PV LO splitter considered for the fabrication tolerance analysis. (1) Height of the backshort. (2, 3) Depth of bend steps. (4) Height of tuning stub. (5) Radius of tuning stub. (6 - 9) Widths and lengths of the microstrips impedance matching section steps.

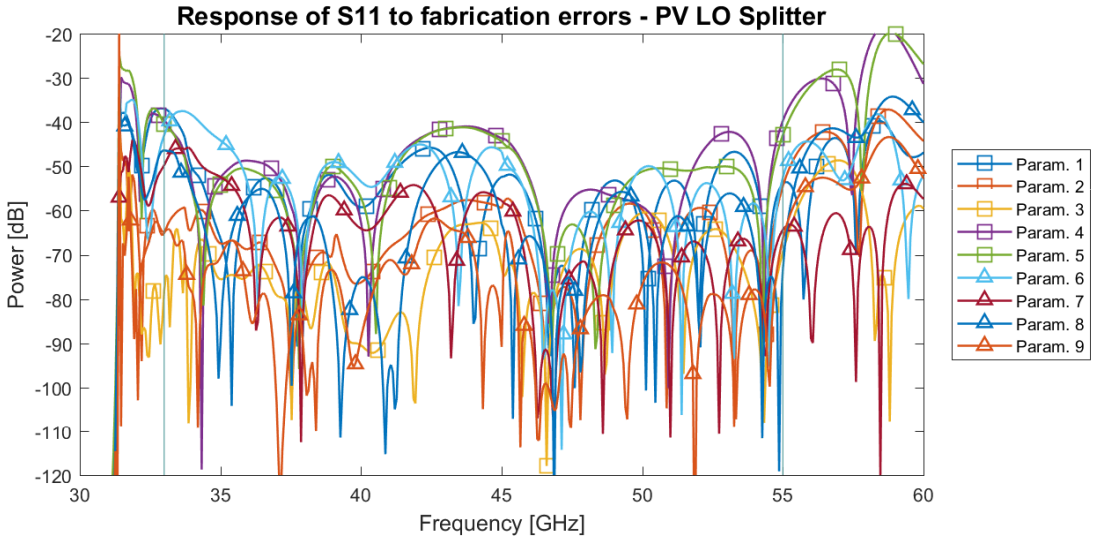

Figure 6.8: Differences of the reflection losses resulting from the tolerance analysis for the PV LO Splitter.

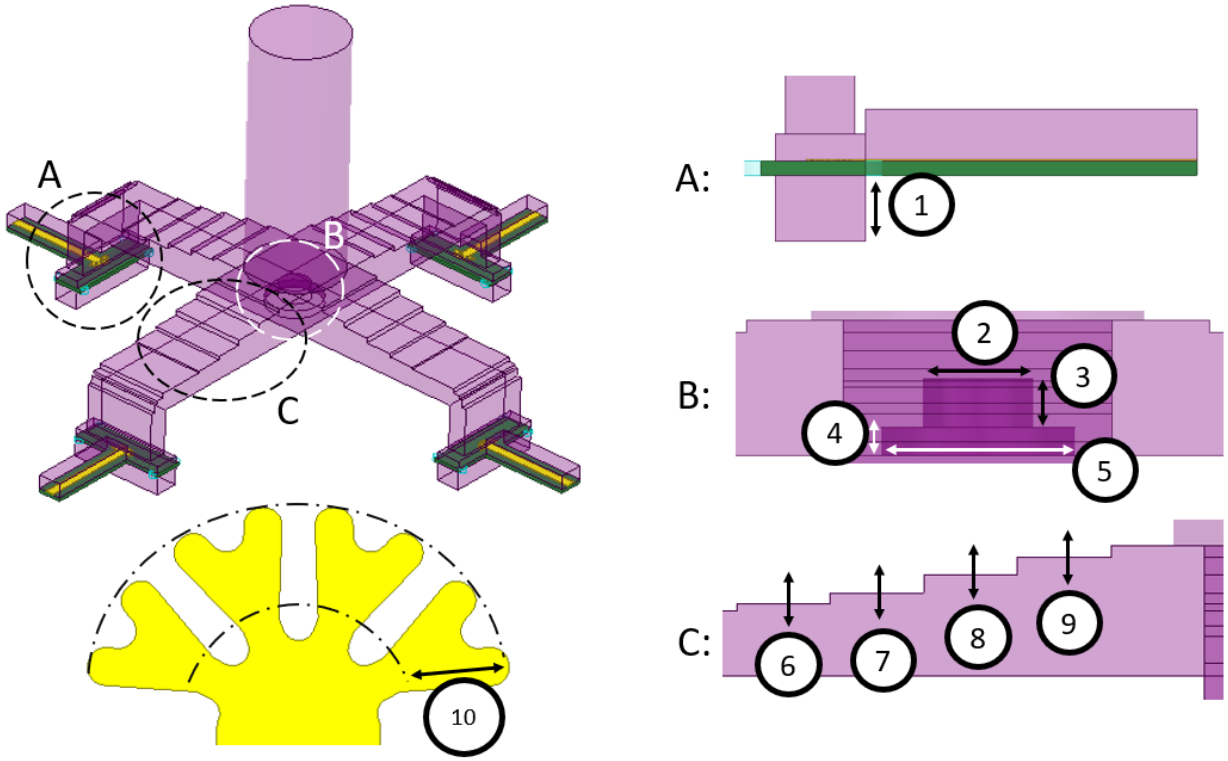

Figure 6.9: Design parameters of the STV OMT considered for the fabrication tolerance analysis. (1) Height of the backshort. (2 - 5) Radii and heights of both steps of the tuning stub. (6 - 9) Depth of the steps from the staggered waveguide section. (10) Length of the outer branches from the dendritic microstrip probe.

6.3.2 Tolerance analysis: PV LO Splitter

The PV LO splitter parameters varied for the tolerance analysis are shown in figure 6.7. Results of the analysis are shown in figure 6.8. Most sensitive parameters are 1, 4, 5, 6, and 8. Respectively, these parameters are the backshort for the media transition, the tuning stub height and radius, and the width of the steps of the microstrips impedance matching section. As in figure 6.6, the greatest power differences are found outside the band of interest, but the peak values are lower. A local maximum is found between 40 and 46 GHz, where parameters 4 and 5 (tuning stub height and radius) show the highest differences in power while physically varying such parameters. Such peak reaches -40 dBW, accounting for a 2% power variation. Figures of the variability of reflection losses for each parameter are shown in Appendix D.

6.3.3 Tolerance analysis: STV OMT

Parameters considered for the tolerance analysis of the STV OMT are shown in figure 6.9. Results for the tolerance analysis are shown in figure 6.10, with vertical markers highlighting the band of interest. In contrast to figures 6.6 and 6.8, power differences towards the outer parts of the band of interest are more similar to those at the inner part. Additionally, curves that show the greatest differences to fabrication errors do so in narrower frequency regions, reaching values between -30 and -40 dBW. That is, power variations between 2% and 4% of the input power. Of particularly high power differences are parameters 1, 6, 7, 8 and

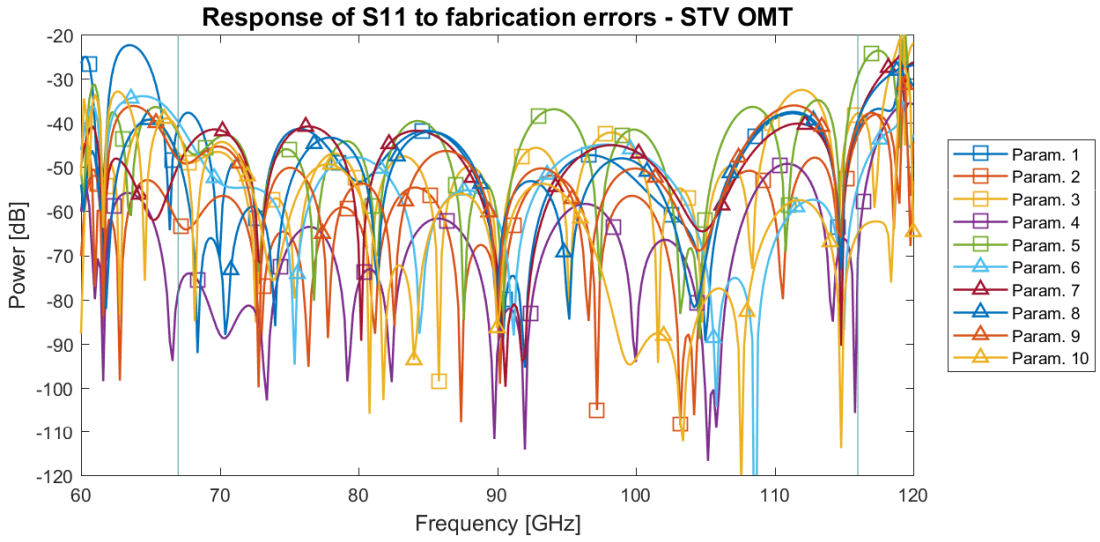

Figure 6.10: Differences of the reflection losses resulting from the tolerance analysis for the STV OMT.

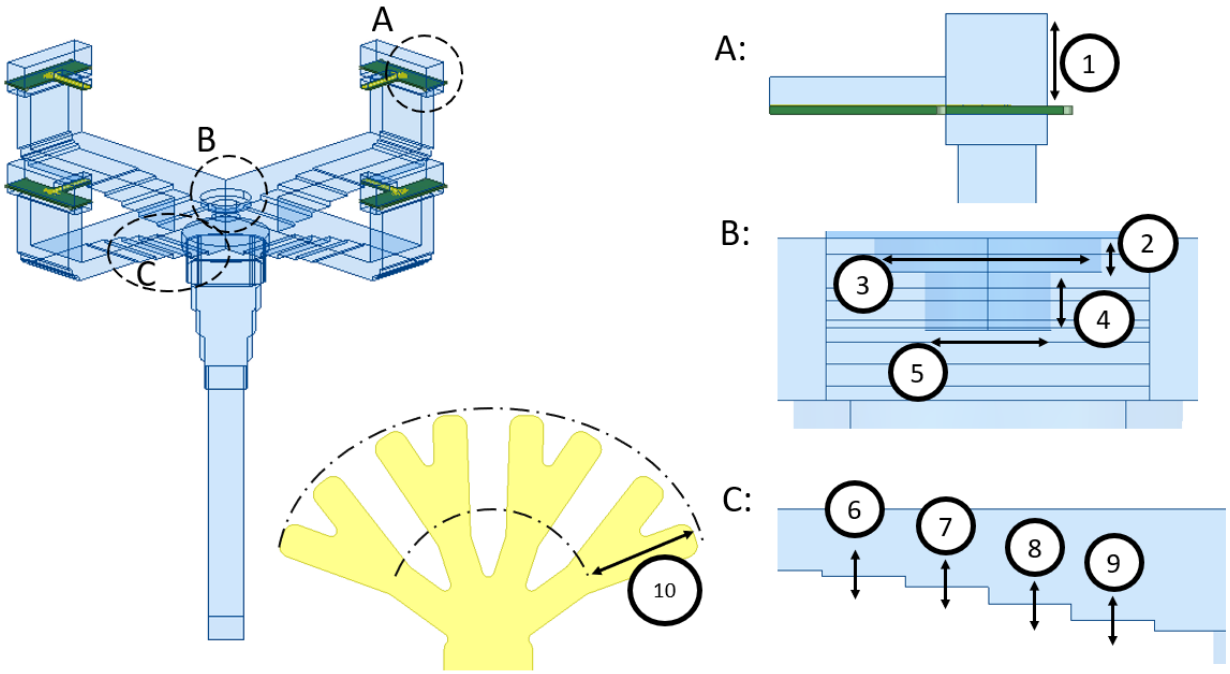

Figure 6.11: Design parameters of the STV LO splitter considered for the fabrication tolerance analysis. (1) Backshort height. (2 - 5) Radii and heights of both steps of the tuning stub. (6 - 9) Depth of the steps from the staggered waveguide section. (10, 11) Lengths of branches from the dendritic microstrip probe.

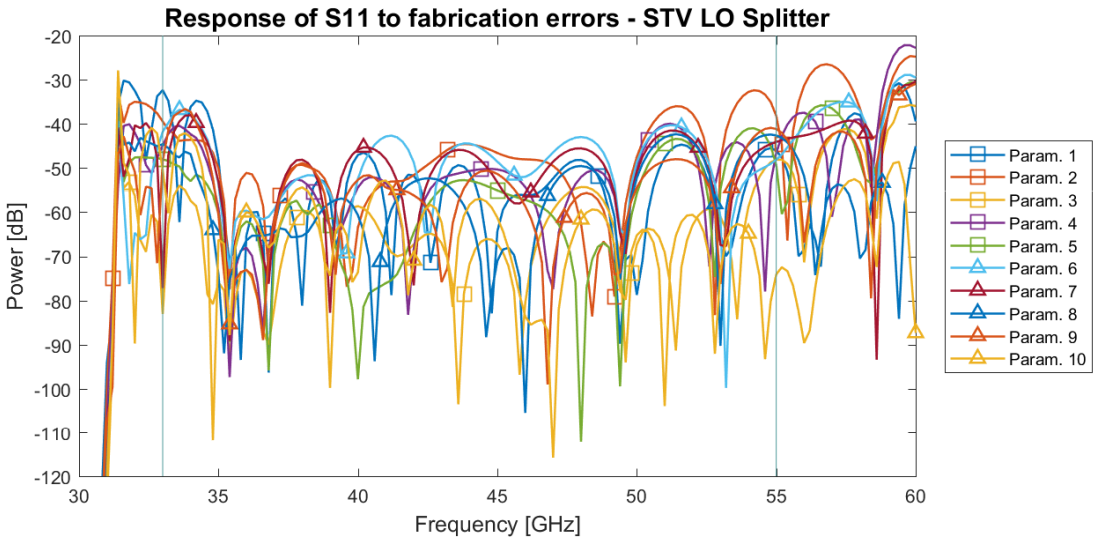

Figure 6.12: Differences of the reflection losses resulting from the tolerance analysis for the STV LO Splitter.

9, which are the height of the backshort and heights of the waveguide steps that exit the turnstile junction of the OMT. Figures of the variability of reflection losses for each individual parameter are shown in Appendix E.

6.3.4 Tolerance analysis: STV LO Splitter

Figure 6.11 shows the STV LO splitter parameters included in the tolerance analysis. Results of the tolerance analysis for the reflection losses are shown in figure 6.12. The behavior of curves is similar to those of figures 6.6 and 6.8, showing lower values around the central frequency of the band. Curves with greater power differences are those of parameters 2, 6, 7 and 8, which correspond to the height of the inner tuning stub, and the last three waveguide steps at the output of the splitter. The height of the inner tuning stub is particularly sensitive to fabrication errors, especially at the higher end of the frequency band. The highest values reached are -30 dBW, which means that power differences across the frequency band are equal or smaller than 4%. Figures of the variability of reflection losses for each parameter are shown in Appendix F.

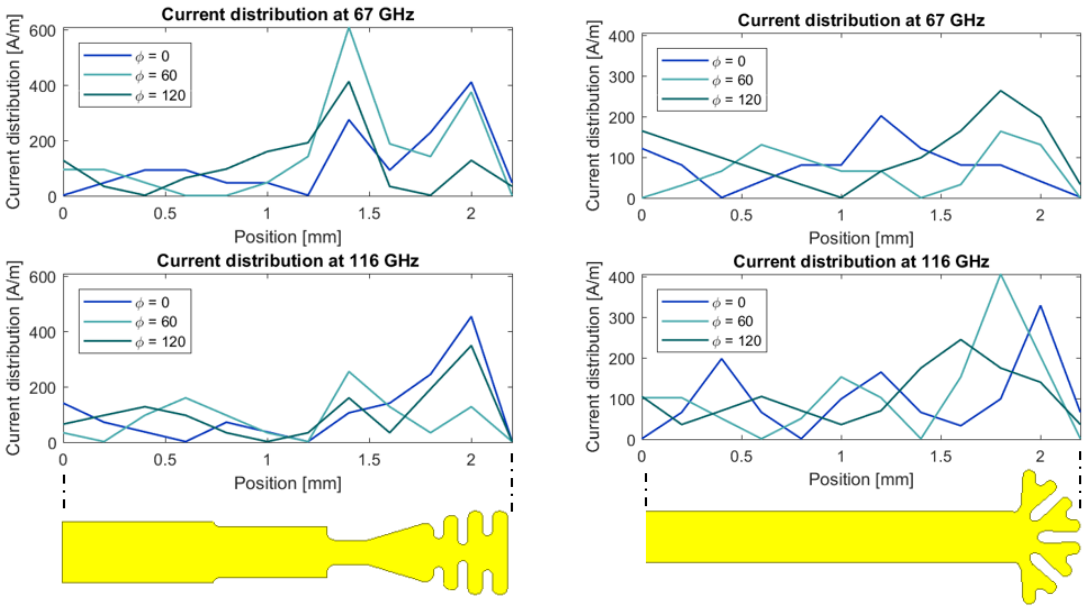

(a) PV OMT.

(b) STV OMT.

Figure 6.13: Surface current distributions versus position along the edges of the probes for an arbitrary input power. Magnitudes of the current distributions are obtained equidistantly along the edges of the microstrip probes at 67 and 116 GHz for different phases.

6.4 Current distribution on probes

In this section, the current distribution on the microstrip probes for both PV and STV OMTs is analyzed. This analysis has two objectives. First, to try to classify the probes in some kind of antennas (resonant, travelling wave or small, for instance). In the second place, to better understand the effect that the slits, or engravements on the radiating surface, of the PV OMT probes have on its performance.

6.4.1 What types of antennas are the designed microstrip probes

In [39], the current distribution on a circular monopole antenna is studied. If maxima of current distribution stay on one particular region of the antenna for different phases, a resonant antenna behavior is identified. Otherwise, if the maxima of current move through the antenna while changing the phase, a travelling wave antenna is identified. An analogous study is carried out considering the PV and STV OMT probes, with results shown in figure 6.13. Additional graphic support is included in Appendix G; current distribution plots are shown for the PV and STV OMT probes. The current distributions are studied at 67 and 116 GHz, considering different phases in each plot.

The current distribution along the edge of the PV OMT probe is shown in figure 6.13a. Note that, for all phases and in both frequencies, the peaks of current accumulation are found either in the narrowest section of the impedance transformer or between the slits. Even if there are peaks of current in two points of the PV probe regardless of the phase of

the incoming wave, there are also peaks of minor magnitude moving through the probe as phase increases. Thus, the probe has a travelling wave antenna behavior. This effect is also observed in [42]. Even if there's an accumulation of current around features on the surface of an antenna, it does not necessarily mean that current is not allowed to circulate on the radiating surface. The travelling wave nature of the PV probe can also be inferred from wave propagation as a function of phase from figures G.1 and G.2 from Appendix G.

That the PV probe is a traveling wave antenna is consistent with the required inclusion of an impedance transformer section. Travelling wave antennas typically have impedances between 200 and 300 Ω, which in this design has to fit with broad bandwidth a 50 Ω transmission line. However, the geometrical shape of the probe would be best characterized as a fat monopole, also consistent with the impedance differences with the transmission line.

The results of the surface current distribution study for the STV OMT probes are shown in figure 6.13b. Unlike the PV probe current distribution, the STV probe shows more intuitively a travelling wave antenna behavior, having peaks of current moving along its surface by increasing the phase of the propagating wave. Results are corroborated by plots of figures G.3 and G.4 from Appendix G. However, a travelling wave antenna would have a high impedance, contrary to the transmission line. This phenomenon could be explained by the metamaterial structure that the STV probe constitutes [48]. The equivalent circuit of the dendritic probe could be seen differently by the incoming microwaves, allowing the propagation of different resonant modes as shown in figure 2.14. Therefore, the dendritic probe would be resonant to a wide band of frequencies yet allowing the coupled waves to travel though the probe.

In conclusion, designed probes for both the PV and STV OMTs operate mostly as travelling wave antennas. Nevertheless, it is not possible to classify these probes only as one type of antenna. Both antennas show a resonant antenna behavior and have the geometries of resonant antennas to some degree, while the travelling wave behavior is mostly clear by the results of figure 6.13.

6.4.2 Study of the influence of slits

The inclusion of slits and other features on the radiating surface of planar antennas is a technique commonly used to modify the antenna performance. Band rejection can be achieved by properly inserting slits on the antenna [40, 41]. On the other hand, modifications of gain can be obtained as well as bandwidth enhancement [42]. In any reported case, the effects of the slits are conveniently claimed to enhance the expected phenomenon. In this section, an effort to explain the behavior of the slits of the PV OMT probes is carried out. This is done by comparing the current distribution on the probe's surface without the slits, and the reflection losses of the PV OMT without the slits on its probes.

An alternative version of the PV OMT was simulated with the only difference that the slits are removed from the microstrip probes as shown in figure 6.14a. The current distribution along the edge of the slitless probe is shown in figure 6.14b for different phases and frequencies. As compared to the current distribution for the original PV OMT probe (figure 6.13a), current does not concentrate at the beginning of the impedance transformer section. Of course there are no slits to accumulate current density around them. According to the discussion of previous section, the patterns described by these curves correspond clearly to a travelling

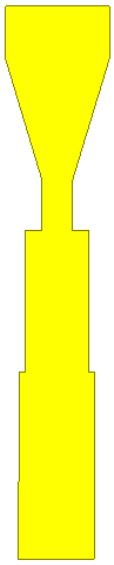

(a) PV OMT probe without slits.

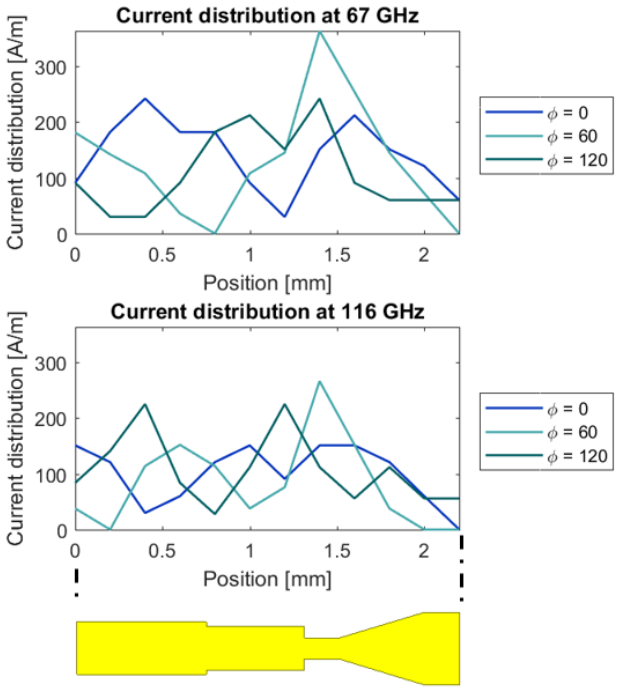

(b) Current distribution.

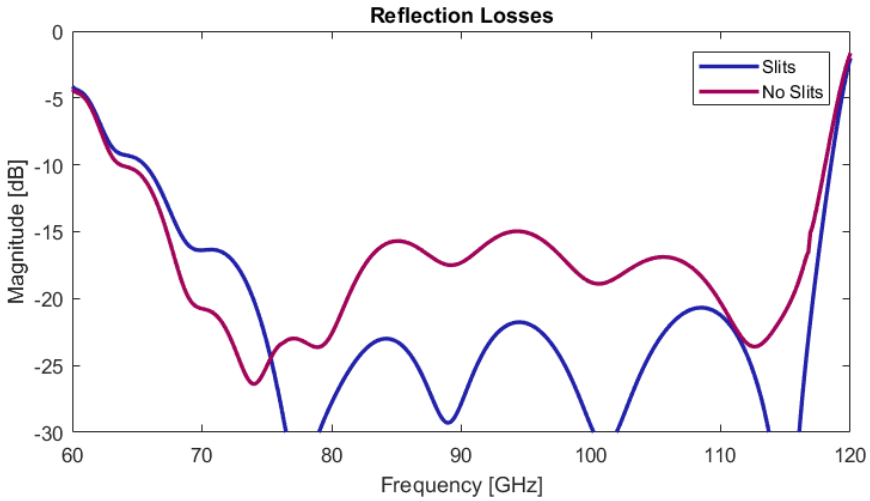

(c) PV OMT reflection losses with and without slits on the probes.

Figure 6.14: Analyses of the effects of removing slits from the PV OMT probe.

wave antenna behavior. In Appendix G, additional figures of the current distribution for different phases are shown in figures G.5 and G.6 for 67 and 116 GHz respectively.

Even if current seems to travel along the new probe unrestricted by structures that would concentrate current density regardless of the phase of the wave, this alternative OMT does not perform as expected. Reflection losses of the no-slit-probes-PV-OMT are shown in figure 6.14c and compared to the PV OMT reflection losses at the input. By removing the slits, bandwidth is widen but reflections worsen up to -15 dB at the input of the OMT.

While comparing the Planar Version of the OMT and the lately simulated alternative

version with slitless probes, the inclusion of slits appears as an improvement to the OMT performance. One explanation to this phenomenon could be found in the solution of Maxwell's equations for radiation problems. The antenna problem described in [34] consists of solving the Maxwell equations for fields **E** and **H** that are created by a current distribution **J** on an antenna surface. In this case, the surface is that of the probes of the OMTs.

Derived from the Maxwell equations, the **H** field can be represented by the curl of an arbitrary vector as:

$$H = \frac{1}{\mu}\nabla \times A \tag{6.3}$$

which is in turn related to the electric field vector as

$$\nabla \times (E + j\omega A) = 0 \tag{6.4}$$

Definitions 6.3 and 6.4 are used together with the Maxwell equations to solve for the potential vector **A** as a source in a volume v':

$$A = \iiint_{v'} \mu J \frac{\mathrm{e}^{-j\beta R}}{4\pi R} \mathrm{d}v' \tag{6.5}$$

The fields **E** and **H** generated by a current distribution **J** can then be found. First, **A** is found from 6.5. Then, the **H** field is found from 6.3. The field **E** can be found from

$$E = \frac{1}{j\omega\varepsilon}(\nabla \times H - J) \tag{6.6}$$

in the source region. If the source is removed in distance from the source, the term **J** in 6.6 is removed [34].

The radiated fields are strongly dependant of the current distribution on a source along the previous analysis, which is also true by the received fields from an antenna (or probe). Modifying the surface current distribution on the antenna will modify the solutions of the wave equation. This would possibly yield a different radiation pattern but most importantly, different frequencies could couple differently to the antenna.

As studied in [40, 41, 42] and in this work, slits and other features on the radiating surface of the antenna strongly modify the current distribution on its surface. This effect can be used to modify the solutions of the equations previously stated. However, there is no explicit analytical behavior of changes to the wave equation solutions by changing the current distribution on an antenna. The antenna performance can be improved by the addition of slits, but it is only found by numerical solutions. The surface current distribution is certainly modified, and it can be taken advantage of until the simulated radiation (and then reception) is adequate to the problem in study. As a conclusion, the addition of slits has a direct effect on the radiation of the antenna but the behavior of this effect must be simulated or studied numerically.

6.5 Summary

Different analyses were performed in this chapter. First, a comparison between reported OMTs and those designed in this work is carried out, considering cross-polarization levels and fractional bandwidth. The performance of the designed planar OMTs can be compared to dual-ridge-type or even turnstile-junction OMTs. An analysis on the detriment of the cross-polarization by connecting mismatching loads to the ports of the OMTs indicates that, as long as the connected loads are similar to each other, degradation of the cross-polar figure is not critical. A study on the isolation of the OMT shows that some degree of phase shifting along the interface is tolerated before signal recombination per polarization. A fabrication tolerance analysis shows which are the most critical parameters of the OMTs and LO splitters to their performances. The current distribution on the probes of the designed OMTs is analyzed, indicating that the antennas have mostly a travelling wave type of antenna behavior. Lastly, a study on the effects of the slits engraved in the PV OMT probes is carried out by solving the Maxwell equations for a radiating antenna.

Chapter 7

Comparison of Results

In this chapter, results from chapters 4 and 5 are compared and additional evaluations are pondered upon the designed receivers. Comparison of electromagnetic figures of merit is purely quantitative. Other aspects, such as the difficulties of fabrication for the PV versus STV front ends, are part of a rather qualitative discussion.

7.1 Electromagnetic performance comparison

In this section, electromagnetic results from simulations of the PV and STV front ends are compared, separated by OMT comparison and LO splitter comparison.

7.1.1 Comparison of OMTs

Comparing two different OMTs is rather direct from their figures of merit. However, the context or technology that the OMT will be used with must be taken into account. Table 7.1 summarizes the reported simulation results for the PV and STV OMTs. Other than the fractional bandwidth of the PV OMT, all the simulated figures of merit accomplish the objectives set in section 1.6.

The designed OMTs in this work are supposed to be operated as digital OMTs, where output signals from the MMIC mixers are combined in the back end of a receiver. In this procedure, signals coming from the OMTs are calibrated to improve their cross-polarization levels to obtain a pure polarization split. As studied in section 6.1, both OMTs have cross-polarization levels better than -23 dB under different tests, theoretically making them feasible to be calibrated by the back end studied in [8]. However, according to the simulation results the only OMT that could possibly benefit from a digital calibration is the PV OMT. The cross-polarization of the STV OMT is so low that the digital calibration would most likely leave the output signals from the STV OMT unmodified. Furthermore, cross-polarization of the STV OMT is lower than any measurable level of this figure of merit. However, digital implementation offers noise reduction due to image rejection via 2SB technique and the STV OMT would anyway benefit from its application [7].

Figure of Merit	PV OMT	STV OMT
Fractional Bandwidth (Reflection Losses under -20 dB)	44.5 %	54 %
Cross-Polar Transmissions	-50 dB	-110 dB
Isolation	-47 dB	-120 dB
Co-Polar Transmissions	-3.5 dB	-4 dB
Cross-Polar Transmissions post re-combination	-48 dB	-120 dB
Co-Polar Transmissions post re-combination	-1 dB	-1.2 dB

Table 7.1: Comparison of simulated figures of merit from the PV and STV OMTs.

The isolation is also a figure of interest when the designed OMTs are used digitally. As studied in section 6.2, both OMTs tolerate phase imbalances between pairs of signals from orthogonal polarizations, giving a margin mostly for setup imbalances. On the other hand, Co-polar transmissions are marginally better for the PV OMT. This can be attributed to the electrical length difference between the designed versions.

7.1.2 Comparison of LO splitters

The PV and STV LO splitters are operational between 35 and 55 GHz. For the PV and STV designs, figures 4.11 and 5.11 show the reflection losses at the input the transmissions to output ports. However, there are peaks in between the band that surpass the -20 dB threshold and reflections do not reach the desired performance at 33 GHz. The operation of the LO splitters can be relaxed to the actual performance of both the PV and STV designs for two reasons. First, a minor amount of bandwidth for the LO could be required depending on the bandwidth of the back end to analyze the output signals from the mixers. Secondly, regarding reflections at the input, power from the tone generator instrument could practically be raised. The main drawback of this second condition is that stationary waves can be formed inside the LO splitter. Effects from the stationary waves can vary from being harmless, to reducing the power seen from the LO input of the mixers, or even to moving the mixers out of their operating zone. These effects are strongly dependant of the instrument to be used for the tone generation of the LO.

7.2 Fabrication comparison

In this section, the subject of manufacturing the front ends is discussed. The size reduction is addressed as well as the fabrication complexities of the designed front ends. Specific study of the designed OMTs is also carried out, being the OMT the core element of this study.

7.2.1 OMT fabrication

Two front ends for a radio astronomy receiver were designed in this work. The front ends contain different elements that were discussed along this thesis, but the ones who received more attention along the design process were the OMTs. In fact, the design of a smaller OMT than the designs reported in the literature motivates this research. Thus, a specific study on the fabrication of the orthomode transducer is carried out.

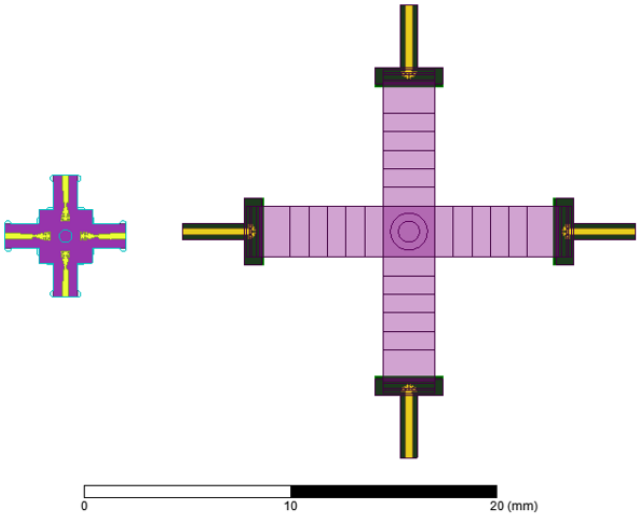

Figure 7.1: Models of the PV and STV OMTs shown under the same metric scale.

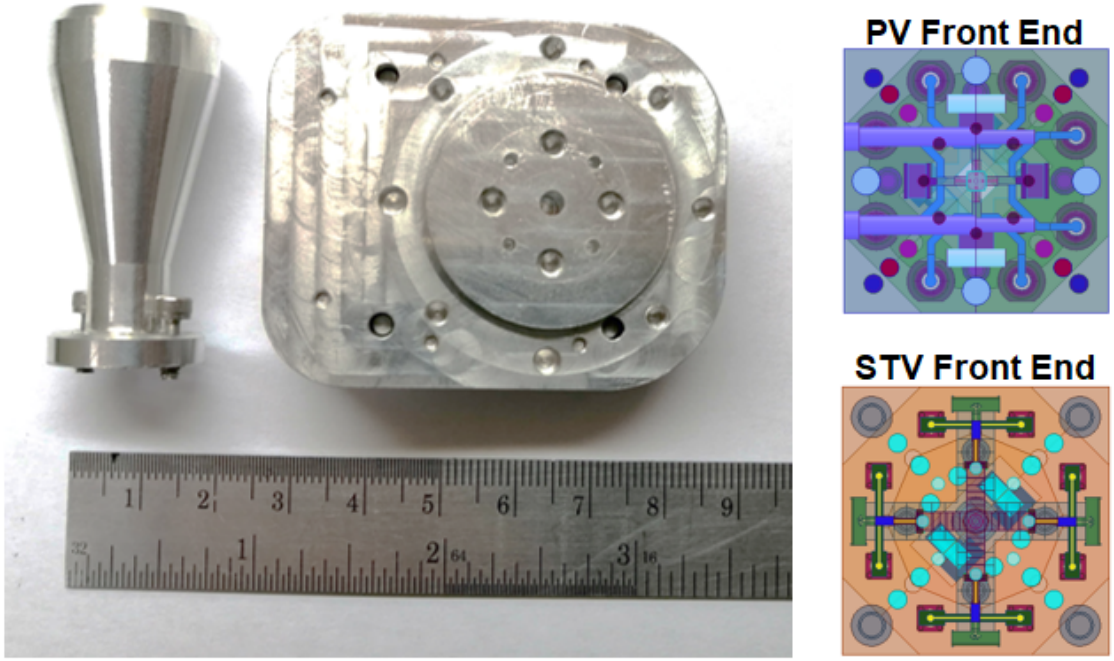

Figure 7.2: Comparison of sizes of OMTs. The fabricated OMT designed by Ignacio Barrueto with the horn antenna used to measure that OMT are shown in the photograph. The models of the two front ends designed in this thesis are shown to scale, and a metric scale is included.

Different views of the PV and STV OMTs are shown in figures 4.1 and 5.2 respectively. These figures do not intend to show the dimensions of each designed OMT, and they rather show their structure and features. In figure 7.1, top views of the PV and STV OMTs are compared under the same metric scale. The PV OMT can be enclosed by a square of 5.8×5.8 mm^2, while the STV OMT is enclosed by a square with edges 22 mm long. The dimensions of the OMTs designed in this work are compared to the OMT developed in [17]. This last OMT is one of the two waveguide OMTs reported in table 1.1 operating at the same frequency

	Radius [mm]	Height [mm]
PV OMT	.29	.50
STV OMT (outer stub)	.90	.26
STV OMT (inner stub)	.51	.45

Table 7.2: Dimensions of the tuning stubs from the designed OMTs.

band of this study, other than [10]. Therefore, size comparison is fair. However, dimensions of the OMT in [10] are not reported. The dimensions of the OMT developed in [17] are $14.4 \times 45 \times 56\ mm^3$, and is shown to scale with the models of the PV and STV front ends in figure 7.2.

7.2.2 Front end fabrication

An overview of the mechanical designs of both the PV and STV front ends are shown in figures 4.13 and 5.13 respectively. As seen from these figures, the footprint of both the PV and STV front ends fit the size of the WR19 waveguide flange. In those figures, there are isometric views of the mechanical blocks that give useful information (figure 4.13c for the PV front end and figure 5.13c for the Semi-Turnstile Version). These mechanical designs consist mostly of metallic sheets that have engraved cavities for the electronics. However, some other blocks are considered. Figure 7.3 shows additional views of the mechanical blocks for the designed front ends. Note that the bottom end for both front ends are made from a splitblock, seen from figures 7.3a and 7.3b. These splitblocks contain the transition from rectangular WR19 waveguide to the turnstile junction of the LO splitter for both the Planar and Semi-Turnstile versions. Up to that point, the mechanical designs are mostly equal.

Above the splitblocks that host the input section of the LO splitters lie the laminated section of the designs, where engraved metallic sheets host the electronic components. A front view of the mechanical designs show clearly the laminated section of the front end blocks. Note that the block for the PV front end (figure 7.3c) has splitblocks that joint perpendicularly to the rest of the metallic sheets. These splitblocks are below the top sheet and make the square waveguide at the input of the PV OMT. Additional alignment bolts and screws are required for these splitblocks, which are placed perpendicularly to the rest of the screws of the mechanical block. In the case of the STV front end (figure 7.3d) no splitblock for the OMT input waveguide is needed because of its circular shape. Therefore, all the required screws and alignment bolts are parallel to each other and only sheets are considered for this section. This simplifies the fabrication of the STV front end as compared to the Planar Version regarding the direction of bolting and assembly of the pieces.

Additional structures must be considered to evaluate the difficulties of fabrication for the Planar and Semi-Turnstile versions of the front end. Tuning stubs were used for the OMTs and LO splitters of both versions for bandwidth enhancement. Figure 7.4 shows the PV and STV OMTs from an angle where their tuning stubs can be seen clearly. In the case of the PV OMT (figure 7.4a), the tuning stub consists of a cylindrical protrusion into the backshort. For the STV OMT, the tuning stub consists of a two-step cylindrical feature at the center of its turnstile junction.

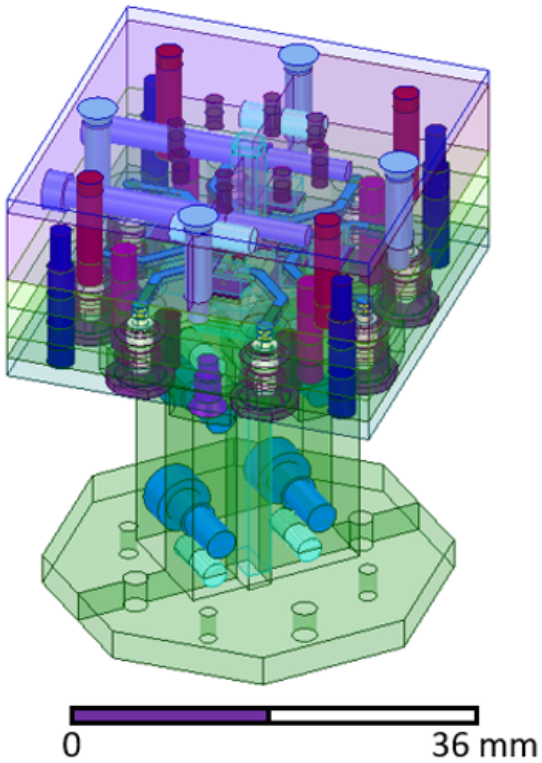

(a) PV front end, trimetric view.

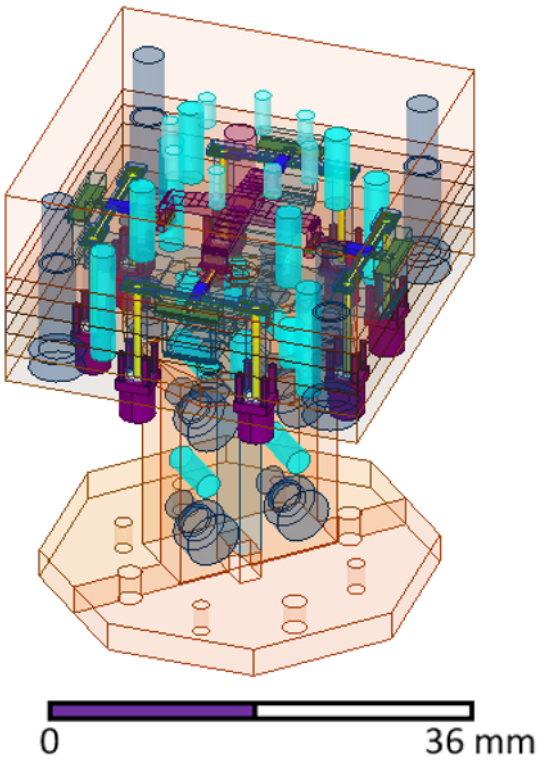

(b) STV front end, trimetric view.

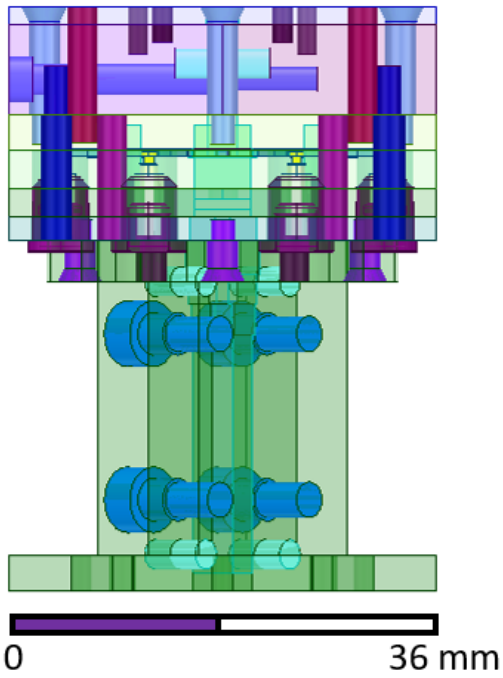

(c) PV front end, front view.

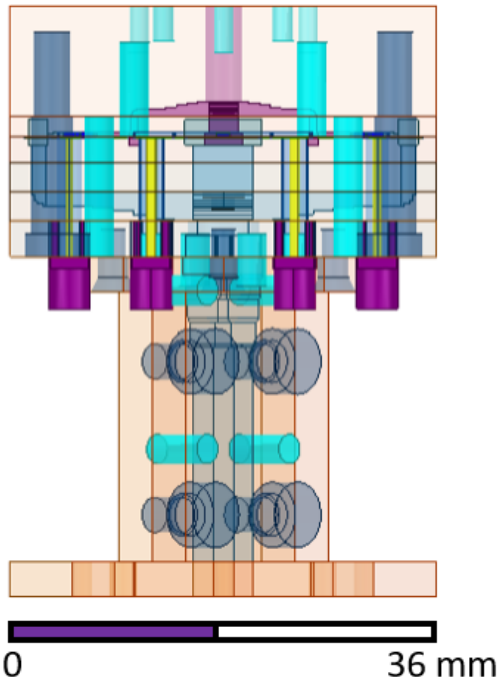

(d) STV front end, front view.

Figure 7.3: Trimetric and front views of the mechanical blocks for the designed front ends.

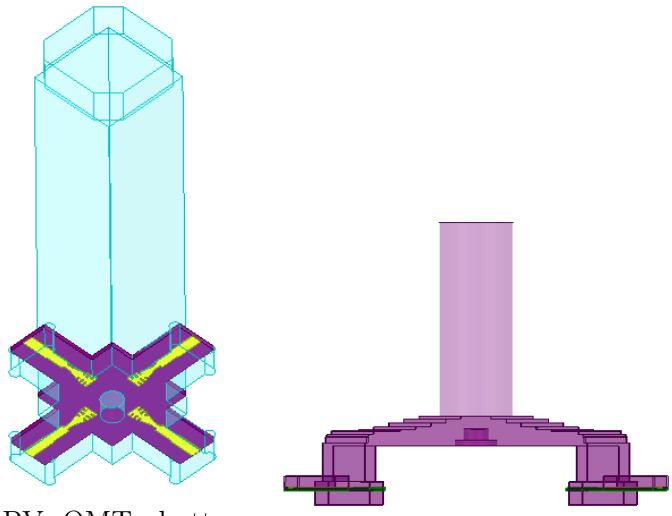

(a) PV OMT, bottom-isometric view.

(b) STV OMT, front view.

Figure 7.4: Views of the designed OMTs where the tuning stubs are clearly seen.

For the current state of the mechanic designs, the inclusion of this stubs imply the milling of one metallic sheet, of the ones discussed above, for both sides. This procedure could possibly create a misalignment of the millings on each sides of the sheet that would have the stubs. On the other hand, the stubs are very thin structures. Table 7.2 shows the radii and heights of the stubs from the OMTs. The stubs from the LO splitters are twice as big as the OMT stubs, with slight modifications after an optimization process. These elements are as thin as wires, and must be handled with care. The stub from the STV OMT is the one who requires more care because it is made from two concentric stubs that are higher than the PV OMT stub, thus more fragile considering its radii.

The last feature to take into account by evaluating the fabrication of the designed front ends are the steps of the staggered sections of the waveguides and the bends. The PV front end has one bend for each output branch of the LO splitter (figure 4.10). These steps are 0.61 mm deep, which is a dimension far from the tolerance error of the considered equipment to fabricate the instruments. Both the STV OMT and LO splitter have each bends and staggered waveguide sections (figures 5.2 and 5.10). The steps of the OMT bends, which are the smallest, are 0.1 mm deep and the steps from the staggered sections vary from 0.06 to 0.17 mm of depth. These dimensions are much closer to the fabrication resolution of the fabrication milling machine than for the Planar Version. The tolerance analysis of section 6.3 indicates that the variation on errors for each step are to be taken into account. Variances of 50 μm of depth for these steps can cause variations in the reflection losses on the order of 10 dB. On top of it, it must be considered that the fabrication errors of the steps can accumulate, especially for the STV designs where the steps are more than those of the PV front end.

7.3 The verdict

The electromagnetic comparison shows objectively that the STV OMT overcomes the performance of the PV OMT by a tremendous margin. The STV OMT is the only one that satisfies the ALMA Band 2+3 requirements. On the other hand, the comparison regarding the fabrication aspects is fuzzier. Considering only the OMTs, the PV OMT is a much simpler structure than the STV OMT. Nevertheless, its fabrication implies difficulties when implementing the PV OMT as part of a front end, as seen in section 7.2.2. The STV front end has a much more straight forward assembly as part of an instrument, but its overall structure has more features than the Planar Version of the designed front end. This could lead to propagation of errors if it is not fabricated with the required precision. Concluding, the mechanical comparison indicates that even though the PV OMT is a simple structure by itself, the STV front end is actually simpler to be fabricated if the correct equipment is considered to manufacture it.

7.4 Conclusions

This chapter summarizes results and observations made across the previous chapters to make comparison between the PV and STV designs and its components. The electromagnetic results are quantitatively compared for the OMTs and LO splitters. The mechanical aspects of each design are discussed addressing different difficulties that would be found along the fabrication of each front end. A final evaluation is given considering the previously stated comparisons.

Conclusion

The objectives set for this research were accomplished. This study demonstrated that the simulated OMTs based on planar structures can perform as good as larger and more complex designs. Other than achieving competitive performance, the use of planar structures can reduce the size of an OMT up to 51.4% of a waveguide OMT. This is also achieved by transferring the operation of signal recombination to the back end of the receiver. This way, the planar OMT architecture becomes feasible for developing focal plane arrays.

The Planar Version of the OMT did not accomplish all the objectives set for its performance. It lacks of operational bandwidth by a fractional 9%. Regarding the rest of the figures of merit, the objectives are accomplished. Even if the PV OMT is not suitable for an ALMA application for band 2+3, its performance makes it competitive to other OMTs, reaching the level of dual-ridge examples reported in the scientific literature. The STV OMT excels in all the evaluated figures of merit, surpassing every objective set for its performance. It performs as good as reported waveguide OMTs. Both the Planar and Semi-Turnstile versions have a footprint equal to 51.4% of a waveguide OMT operating at the same frequency band.

The designs of either the PV or STV front ends show mechanical difficulties of different kinds, which condition the manufacture of these instruments to high precision equipment. In any case, size reduction is achieved up to the point that the electronics can be enclosed by a structure with a footprint equal to the size of a WR19 waveguide flange. In other words, the designed front ends' footprints are as small as their largest non-reducible component, considering standard dimensions.

Future work should explore the possibility of including a low noise amplifier between the OMT outputs and the MMIC mixers. This would face the difficulties of fitting more electronic elements inside a rather reduced space, while also considering the use of a biasing network. Further study of the LO splitters is suggested to avoid stationary waves inside them, particularly due to reflections at the input. A simplification of the STV OMT and LO splitter designs in terms of amount of features would also be useful to potentially increase the robustness of these designs to manufacturing errors.

Bibliography

[1] A. Gonzalez, V. Tapia, N. Reyes, F. P. Mena, R. Nesti, F. Villa, F. Cuttaia, A. De Rosa, A. M. Di Giorgio, A. Morbidini, and P. Yagoubov. ALMA band 2+3 (67-116 GHz) optics: Design and first measurements. *2016 IEEE Antennas and Propagation Society International Symposium, APSURSI 2016 - Proceedings*, pages 1195–1196, 2016.

[2] Matthew A Morgan and J Richard Fisher. Next Generation Radio Astronomy Receiver Systems. *Time*, 2009.

[3] Daniel V. Cotton, Jeremy Bailey, Ian D. Howarth, Kimberly Bott, Lucyna Kedziora-Chudczer, P. W. Lucas, and J. H. Hough. Polarization due to rotational distortion in the bright star Regulus. *Nature Astronomy*, 1(10):690–696, 2017.

[4] A Richard Thompson, J.˜M. Moran, and George W Swenson. *Interferometry and Synthesis in Radio Astronomy Astronomy and Astrophysics Library.*

[5] Goutam Chattopadhyay and David Miller. A dual-polarized quasi-optical SIS mixer at 550 GHz. *IEEE Transactions on Microwave Theory and Techniques*, 48(10):1680–1686, 2000.

[6] Ronald Hesper, Gerrit Gerlofsma, Patricio Mena, Marco Spaans, and Andrey Baryshev. A Sideband-Separating Mixer Upgrade for ALMA Band 9. *20th International Symposium on Space Terahertz Technology*, (April):20–22, 2009.

[7] Ricardo Finger, Patricio Mena, Nicolás Reyes, Rafael Rodriguez, and Leonardo Bronfman. A Calibrated Digital Sideband Separating Spectrometer for Radio Astronomy Applications. *Publications of the Astronomical Society of the Pacific*, 125(925):263–269, 2013.

[8] Andrés Alvear. *Ultra-Pure Digital Detection of Polarization for Radio Astronomy Applications.* Ms. c. thesis, Universidad de Chile, 2018.

[9] Matthew Sieth, Kiruthika Devaraj, Patricia Voll, Sarah Church, Rohit Gawande, Kieran Cleary, Anthony C. S. Readhead, Pekka Kangaslahti, Lorene Samoska, Todd Gaier, Paul F. Goldsmith, Andrew I. Harris, Joshua O. Gundersen, David Frayer, Steve White, Dennis Egan, and Rodrigo Reeves. Argus: a 16-pixel millimeter-wave spectrometer for the Green Bank Telescope. *Millimeter, Submillimeter, and Far-Infrared Detectors and Instrumentation for Astronomy VII*, 9153:91530P, 2014.

[10] Doug Henke and Stéphane Claude. Design of a 70-116 GHz W-band turnstile OMT. *European Microwave Week 2014: Connecting the Future, EuMW 2014 - Conference Proceedings; EuMC 2014: 44th European Microwave Conference*, (c):456–459, 2014.

[11] Giampaolo Pisano, Luca Pietranera, Kate Isaak, Lucio Piccirillo, Bradley Johnson, Bruno Maffei, and Simon Melhuish. A broadband WR10 turnstile junction orthomode transducer. *IEEE Microwave and Wireless Components Letters*, 17(4):286–288, 2007.

[12] Nicolas Reyes, Pablo Zorzi, Jose Pizarro, Ricardo Finger, F. Patricio Mena, and Leonardo Bronfman. A dual ridge broadband orthomode transducer for the 7-mm band. *Journal of Infrared, Millimeter, and Terahertz Waves*, 33(12):1203–1210, 2012.

[13] P. K. Grimes, O. G. King, G. Yassin, and M. E. Jones. Compact broadband planar orthomode transducer. *Electronics Letters*, 43(21):1146–1148, 2007.

[14] C. Baer, C. Schulz, B. Will, I. Rolfes, and T. Musch. A planar orthomode transducer for broadband applications at 25 GHz using a stepped waveguide technique. *Asia-Pacific Microwave Conference Proceedings, APMC*, 1(3):373–375, 2012.

[15] Juan L. Cano and Angel Mediavilla. Quasi-octave bandwidth in-phase three-layer platelet orthomode transducer using improved power combiners. *IEEE Microwave and Wireless Components Letters*, 28(12):1086–1088, 2018.

[16] Chau Ching Chiong, Chen Chien, Chih Cheng Chang, Yau De Huang, and Yuh Jing Hwang. Cryogenic 29-50 GHz orthomode transducer for radio astronomical receiver. *Asia-Pacific Microwave Conference Proceedings, APMC*, 2018-Novem:1271–1273, 2019.

[17] Ignacio Barrueto G. *Development of Microwave Devices for Millimeter and Sub-Millimeter Receivers*. Ms. c. thesis, Universidad de Chile, 2017.

[18] Alessandro Navarrini and Renzo Nesti. Symmetric reverse-coupling waveguide orthomode transducer for the 3-mm band. *IEEE Transactions on Microwave Theory and Techniques*, 57(1):80–88, 2009.

[19] G. Virone, O. A. Peverini, G. Addamo, Z. Farooqui, and R. Tascone. Platelet Orthomode Transducer (OMT) for millimeter-wave applications. *Proceedings of the 2013 International Conference on Electromagnetics in Advanced Applications, ICEAA 2013*, pages 394–395, 2013.

[20] F. Del Torto, M. Bersanelli, C. Franceschet, O. A. Peverini, A. Simonetto, R. Tascone, and G. Virone. A platelet W-band feed horn-OMT assembly. *Proceedings of the 2013 International Conference on Electromagnetics in Advanced Applications, ICEAA 2013*, pages 939–941, 2013.

[21] Oscar Antonio Peverini, Riccardo Tascone, Augusto Olivieri, Massimo Baralis, Renato Orta, and Giuseppe Virone. A microwave measurement procedure for a full characterization of ortho-mode transducers. *IEEE Transactions on Microwave Theory and Techniques*, 51(4 I):1207–1213, 2003.

[22] Shin'ichiro Asayama and Taku Nakajima. Development of a Smooth Taper Double-Ridge Waveguide Orthomode Transducer for a New 100 GHz Band Z-Machine Receiver for the NRO 45-m Radio Telescope. *Publications of the Astronomical Society of the Pacific*, 125(924):213–217, 2013.

[23] Philip Mauskopf, Peter Ade, Stafford Withington, Jin Zhang, and Paul Grime. Clover polarimetric detector - A novel design of an ortho-mode transducer at 150 and 225 GHz. *Progress in Electromagnetics Research Symposium*, 1:164–167, 2008.

[24] Wenlei Shan, Shohei Ezaki, Keiko Kaneko, Akihira Miyachi, and Takafumi Kojima. Experimental Study of a Planar-integrated Dual-Polarization Balanced SIS Mixer. *IEEE Transactions on Terahertz Science and Technology*, PP(X):1, 2019.

[25] David Monasterio. *Development of Compact Heterodyne Downconverters for the Extended W-Band*. Thesis proposal, Universidad de Chile, 2020.

[26] R. Gawande, R. Reeves, L. Samoska, K. Cleary, A. C. Readhead, T. Gaier, P. Kangaslahti, M. Varonen, S. Church, K. Devaraj, M. Sieth, and M. Morgan. W-band IQ sub-harmonic mixers with low LO power for cryogenic operation in large arrays. *European Microwave Week 2014: "Connecting the Future", EuMW 2014 - Conference Proceedings; EuMIC 2014: 9th European Microwave Integrated Circuits Conference*, pages 301–304, 2014.

[27] D.M. Pozar. *Microwave Engineering, Fourth Edition Wiley E-Text Reg Card*. John Wiley & Sons, Incorporated, 2013.

[28] James Clerk Maxwell. *A Treatise on Electricity and Magnetism*, volume 2 of *Cambridge Library Collection - Physical Sciences*. Cambridge University Press, 2010.

[29] Oliver Heaviside. *Electromagnetic Theory*, volume 2 of *Cambridge Library Collection - Technology*. Cambridge University Press, 2011.

[30] IEEE Standard 145-1983. Standard Definitions of Terms for Antennas. *reprinted in IEEE Trans. Antennas Propagat.*, AP-31, 1983.

[31] José M. Pérez-Escudero, Alicia E. Torres-García, Ramón Gonzalo, and Iñigo Ederra. A simplified design inline microstrip-to-waveguide transition. *Electronics (Switzerland)*, 7(10):1–11, 2018.

[32] Leo G. Maloratsky. Passive RF & Microwave Integrated Circuits. *Passive RF & Microwave Integrated Circuits*, pages 1–368, 2003.

[33] Jianxin Liang. Antenna Study and Design for Ultra Wideband Communication Applications. *Electronic Engineering*, (July), 2006.

[34] Gary A. Thiele Warren L. Stutzman. *Antenna Theory and Design, 3rd Edition*. Wiley, 3rd edition edition, 2012.

[35] L. J. Chu. Physical limiations of omnidirectional antennas. *Journal of Applied Physics*,

19:1163–1175, 1948.

[36] Harold A. Wheeler. Fundamental limitations of small antennas. *Proceedings of the IRE*, 35(12):1479–1484, 1947.

[37] R. C. Hansen. Fundamental limitations in antennas. *Proceedings of the IEEE*, 69(2):170–182, 1981.

[38] A.W. Rudge, K. Milne, A.D. Olver, and P. Knight. *The Handbook of Antenna Design*. Number v. 1 in IEE electromagnetic waves series. P. Peregrinus, 1982.

[39] Foad Fereidoony, Somayyeh Chamaani, and Seyed Abdullah Mirtaheri. Systematic design of UWB monopole antennas with stable omnidirectional radiation pattern. *IEEE Antennas and Wireless Propagation Letters*, 11:752–755, 2012.

[40] Bo Chen, Yongchang Jiao, Fengchao Ren, and Fushun Zhang. Dual wideband open slot antenna with a band-rejected slit for 3.5/5.5GHz WiMAX and 5.2/5.8GHz WLAN applications. *Proceedings - 2011 4th IEEE International Symposium on Microwave, Antenna, Propagation and EMC Technologies for Wireless Communications, MAPE 2011*, pages 113–115, 2011.

[41] N. Rajasekhar, R. Ramana Reddy, and N. K. Darimireddy. V-shaped slits and a slot loaded pentagonal boundary patch antennas for wideband applications. *2017 IEEE International Conference on Antenna Innovations and Modern Technologies for Ground, Aircraft and Satellite Applications, iAIM 2017*, pages 1–5, 2018.

[42] Raj Gaurav Mishra, Ranjan Mishra, Piyush Kuchhal, and N Prasanthi Kumari. Rectangular Microstrip Antenna by Inserting Slots , Notches and Slits. (Icces):650–653, 2017.

[43] Sebastián Sepúlveda. *Diseño y fabricación de antenas planares basadas en estructuras de metamateriales*. Engineering thesis, Universidad de Chile, 2018.

[44] Diego Gallardo. *Diseño, construcción y caracterización de un arreglo de antenas de banda ancha basado en metamateriales*. Engineering thesis, Universidad de Chile, 2020.

[45] D. Schurig, J. J. Mock, and D. R. Smith. Electric-field-coupled resonators for negative permittivity metamaterials. *Applied Physics Letters*, 88(4):1–3, 2006.

[46] X. Zhou and X. P. Zhao. Resonant condition of unitary dendritic structure with overlapping negative permittivity and permeability. *Applied Physics Letters*, 91(18):13–16, 2007.

[47] Matthew A. Morgan and Shing Kuo Pan. Graphical prediction of trapped mode resonances in sub-mm and THz networks. *23rd International Symposium on Space Terahertz Technology 2012, ISSTT 2012*, pages 34–37, 2012.

[48] G. Arun Kumar and D. R. Poddar. Broadband Rectangular Waveguide to Suspended Stripline Transition Using Dendritic Structure. *IEEE Microwave and Wireless Compo-*

nents Letters, 26(11):900–902, 2016.

[49] Cristian Daniel Lopez, Vincent Desmaris, Denis Meledin, Alexey Pavolotsky, and Victor Belitsky. Waveguide to Substrate Transition Based on Unilateral Substrateless Finline Structure: Design, Fabrication, and Characterization. *IEEE Transactions on Terahertz Science and Technology*, (c):1–1, 2020.

Appendices

Appendix A

Results for cross-polarization tests: imperfect matching at the output ports of the PV OMT

Scenario 1, PV OMT.

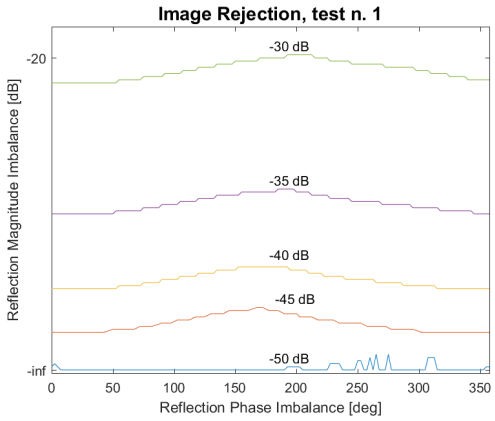

(a) Test 1, scenario 1.

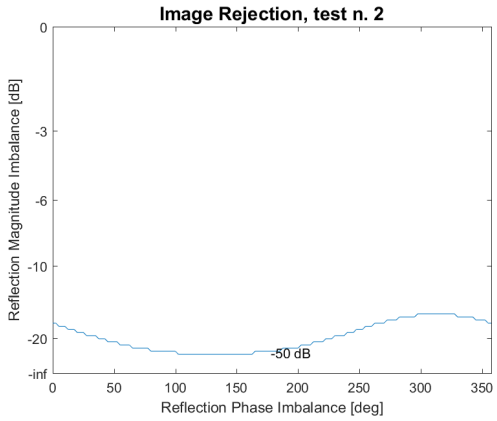

(b) Test 2, scenario 1.

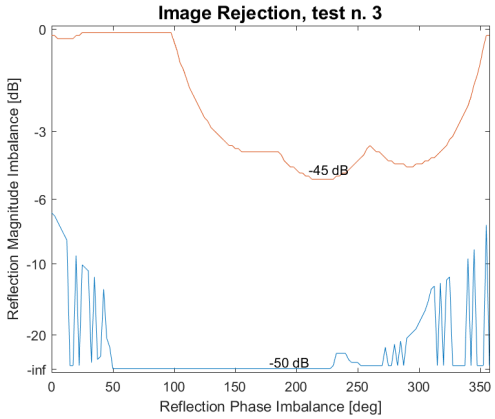

(c) Test 3, scenario 1.

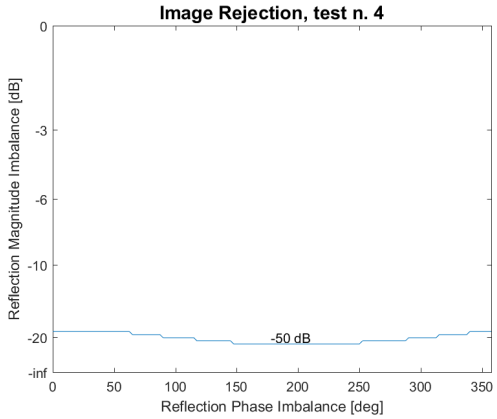

(d) Test 4, scenario 1.

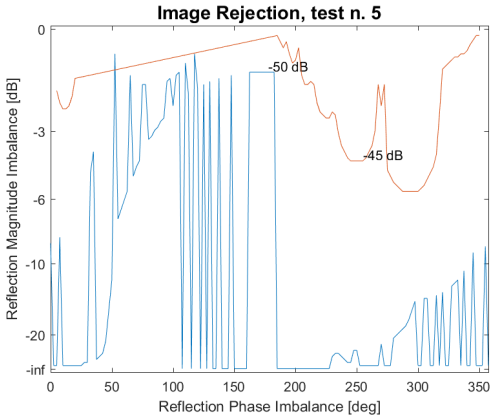

(e) Test 5, scenario 1.

Figure A.1: PV OMT cross-polarization test results using $\Gamma_{fixed} = -\infty$ dB and $\Gamma_{variable} \in [-\infty, 0]$ dB, $\forall\phi$.

Scenario 2, PV OMT.

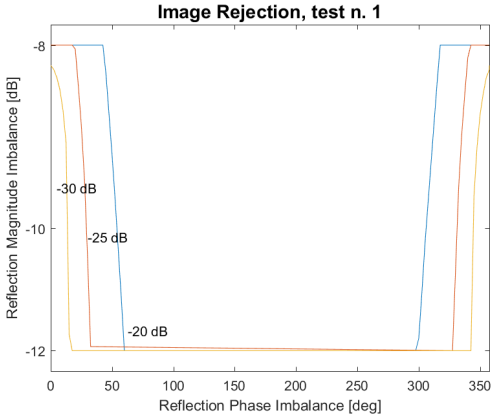

(a) Test 1, scenario 2.

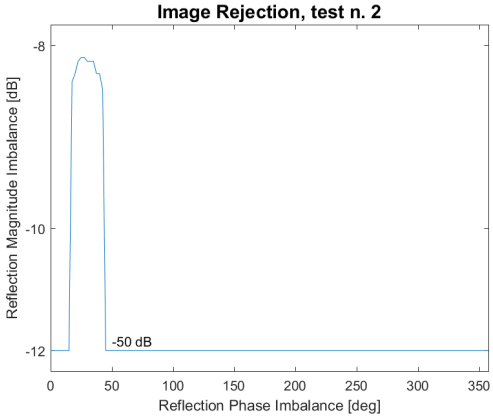

(b) Test 2, scenario 2.

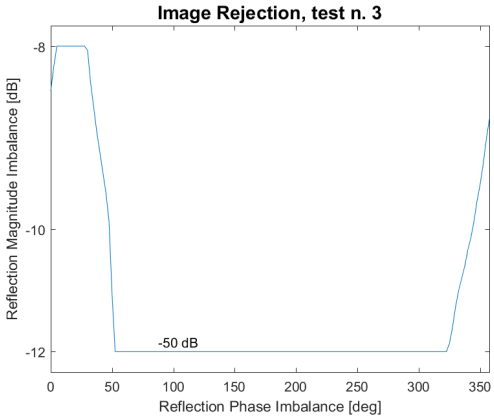

(c) Test 3, scenario 2.

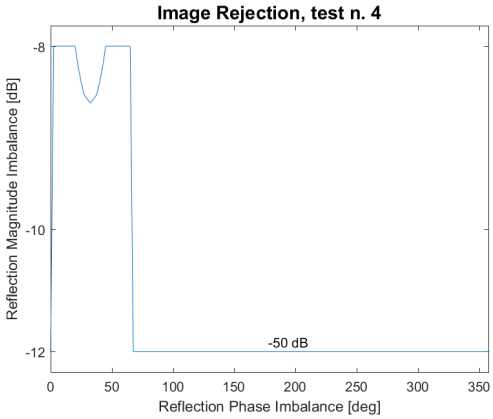

(d) Test 4, scenario 2.

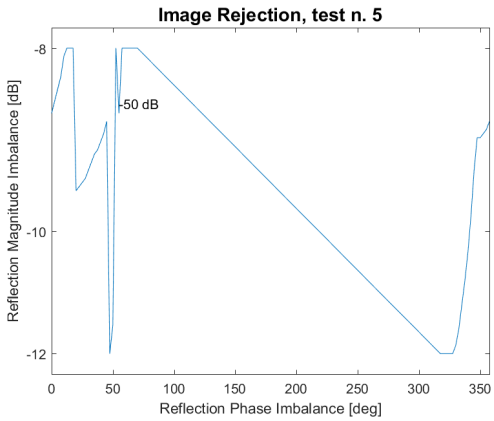

(e) Test 5, scenario 2.

Figure A.2: PV OMT cross-polarization test results using $\Gamma_{fixed} = -10$ dB and $\Gamma_{variable} \in [-8, -12]$ dB, $\forall\phi$.

Scenario 3, PV OMT.

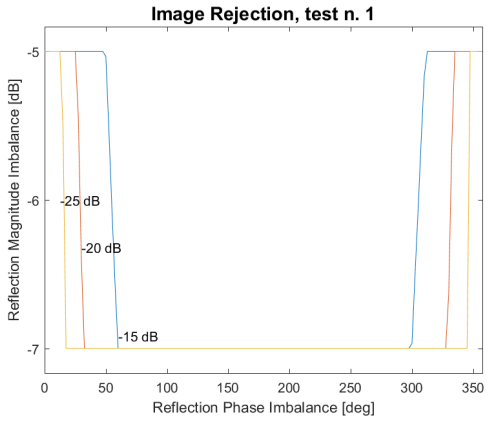

(a) Test 1, scenario 3.

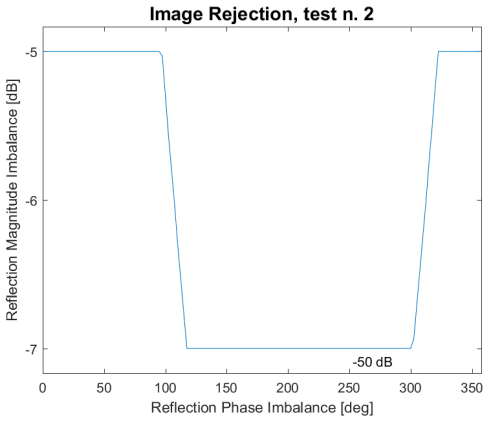

(b) Test 2, scenario 3.

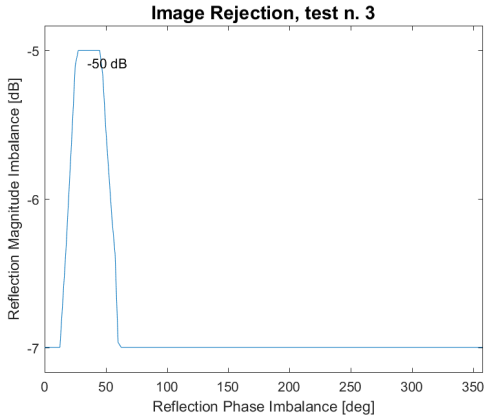

(c) Test 3, scenario 3.

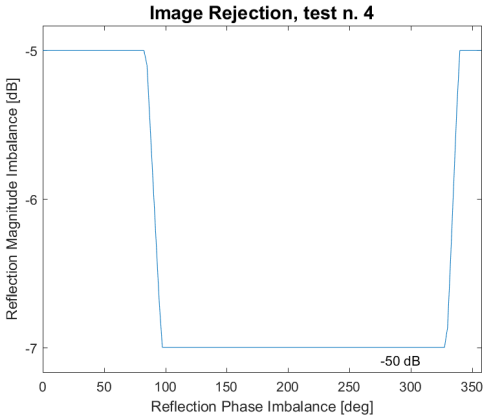

(d) Test 4, scenario 3.

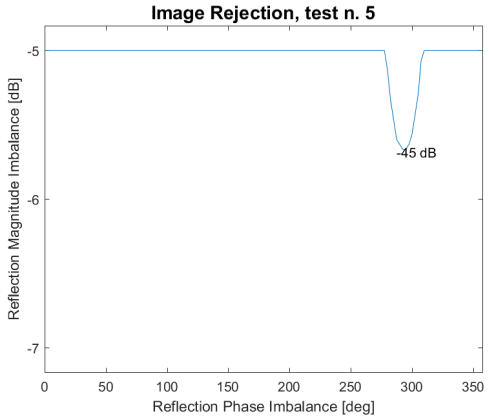

(e) Test 5, scenario 3.

Figure A.3: PV OMT cross-polarization test results using $\Gamma_{fixed} = -6$ dB and $\Gamma_{variable} \in [-7, -5]$ dB, $\forall\phi$.

Scenario 4, PV OMT.

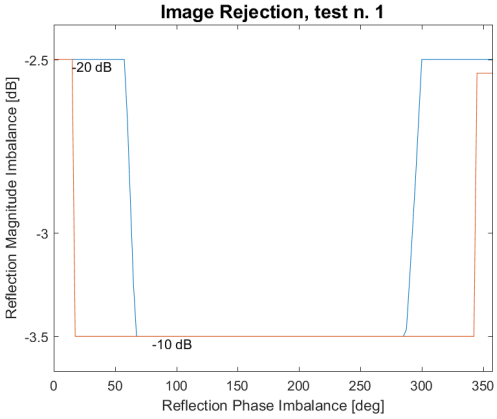

(a) Test 1, scenario 4.

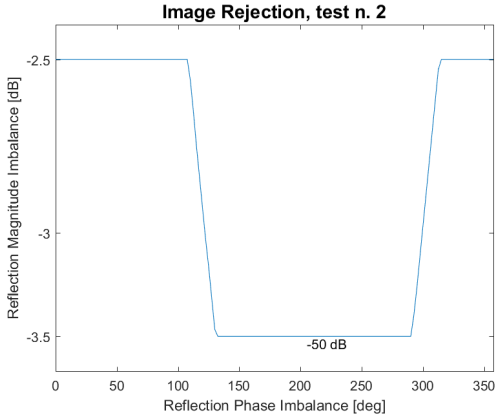

(b) Test 2, scenario 4.

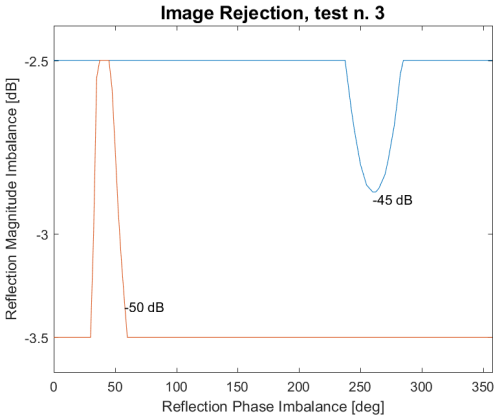

(c) Test 3, scenario 4.

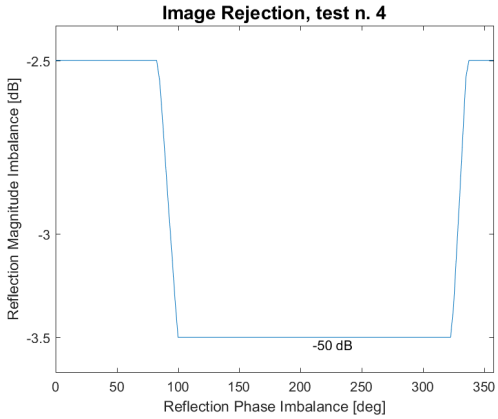

(d) Test 4, scenario 4.

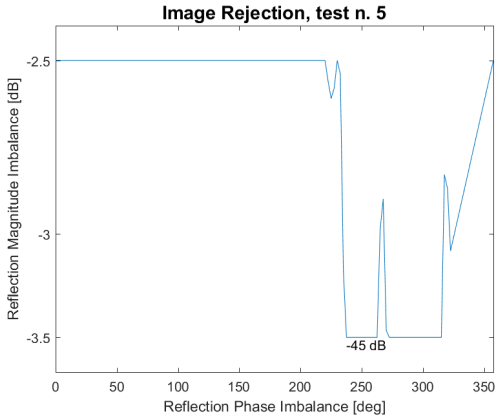

(e) Test 5, scenario 4.

Figure A.4: PV OMT cross-polarization test results using $\Gamma_{fixed} = -3$ dB and $\Gamma_{variable} \in [-3.5, -2.5]$ dB, $\forall\phi$.

Appendix B

Results for cross-polarization tests: imperfect matching at the output ports of the STV OMT

Scenario 1, STV OMT.

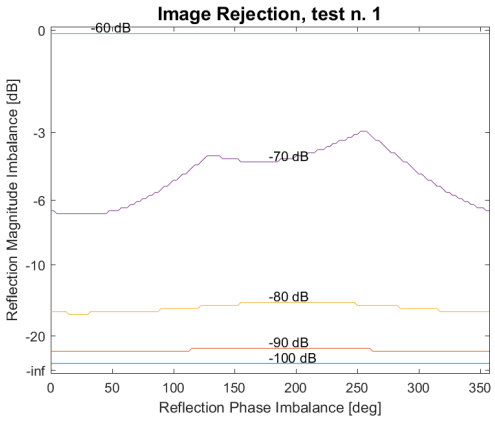

(a) Test 1, scenario 1.

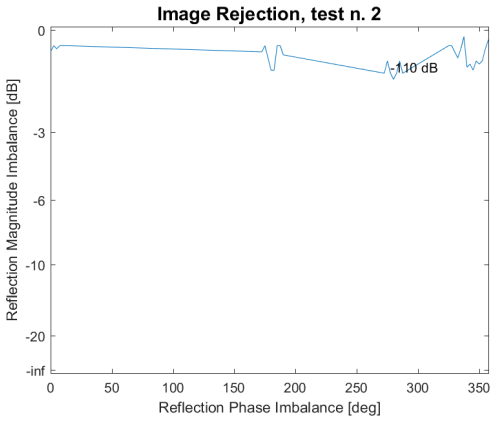

(b) Test 2, scenario 1.

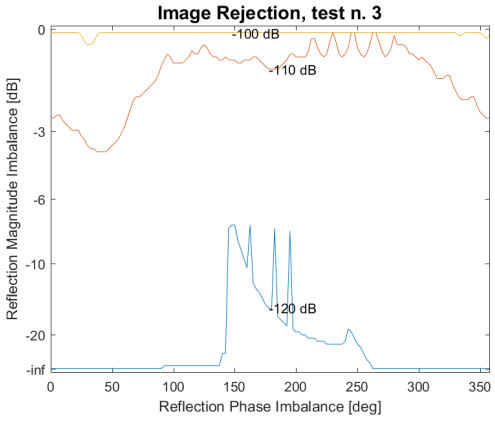

(c) Test 3, scenario 1.

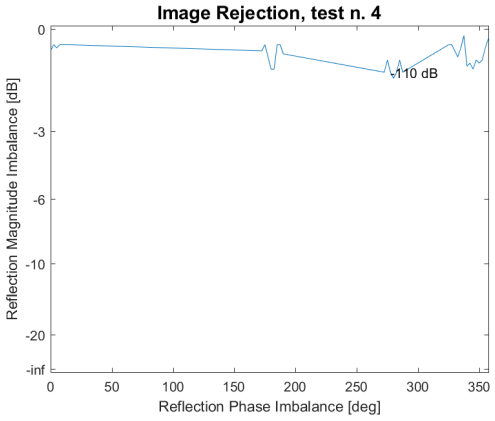

(d) Test 4, scenario 1.

(e) Test 5, scenario 1.

Figure B.1: STV OMT cross-polarization test results using $\Gamma_{fixed} = -\infty$ dB and $\Gamma_{variable} \in [-\infty, 0]$ dB, $\forall\phi$.

Scenario 2, STV OMT.

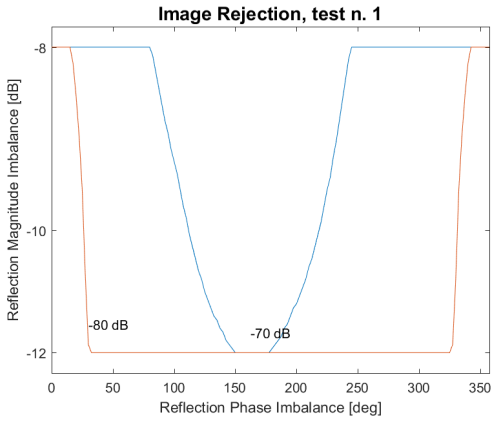

(a) Test 1, scenario 2.

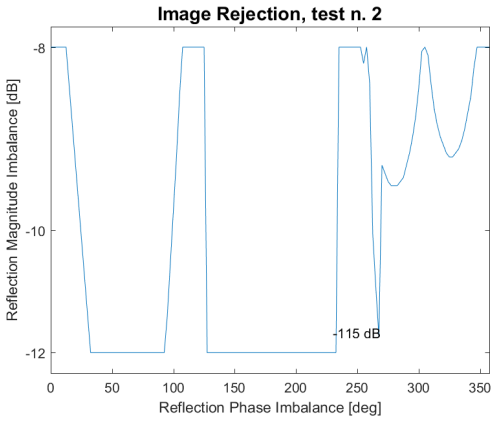

(b) Test 2, scenario 2.

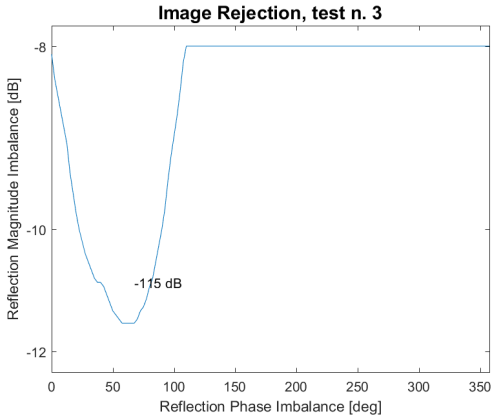

(c) Test 3, scenario 2.

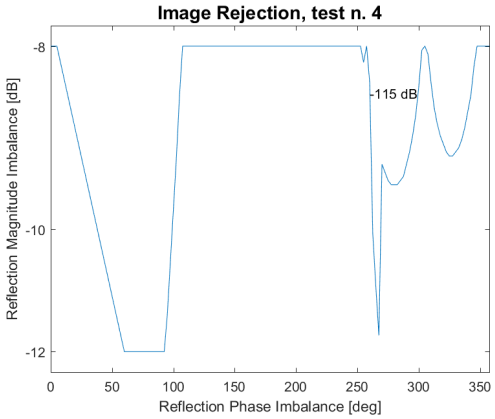

(d) Test 4, scenario 2.

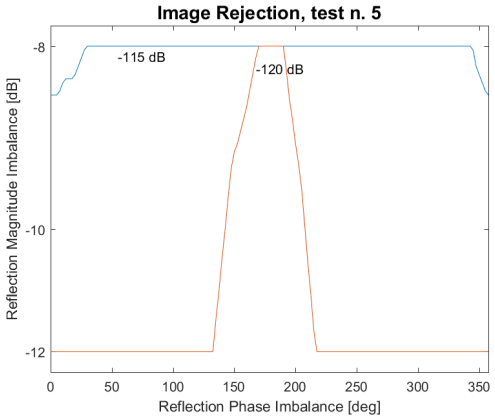

(e) Test 5, scenario 2.

Figure B.2: STV OMT cross-polarization test results using $\Gamma_{fixed} = -10$ dB and $\Gamma_{variable} \in [-12, -8]$ dB, $\forall\phi$.

Scenario 3, STV OMT.

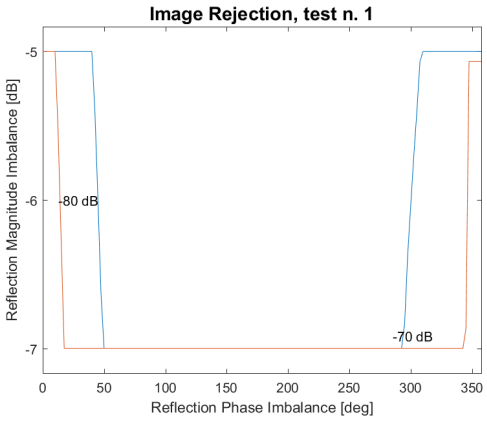

(a) Test 1, scenario 3.

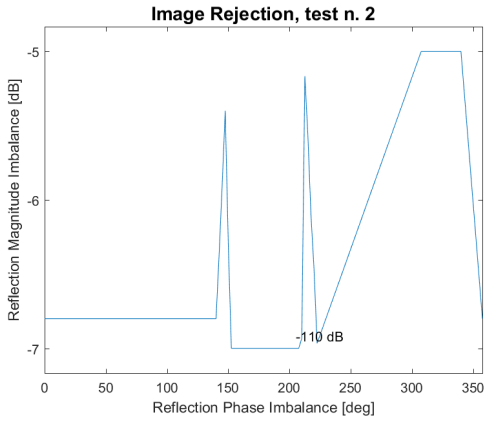

(b) Test 2, scenario 3.

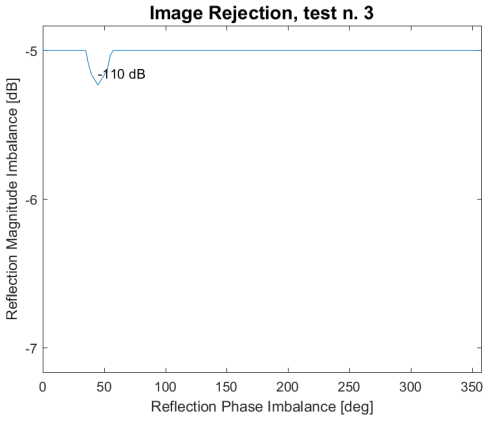

(c) Test 3, scenario 3.

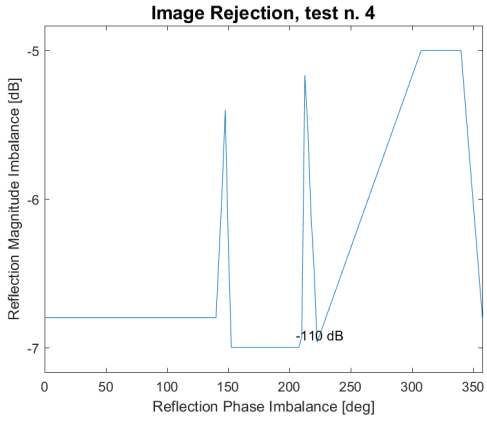

(d) Test 4, scenario 3.

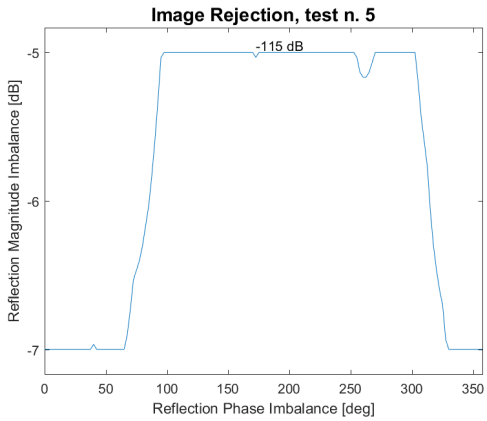

(e) Test 5, scenario 3.

Figure B.3: STV OMT cross-polarization test results using $\Gamma_{fixed} = -6$ dB and $\Gamma_{variable} \in [-7, -5]$ dB, $\forall\phi$.

Scenario 4, STV OMT.

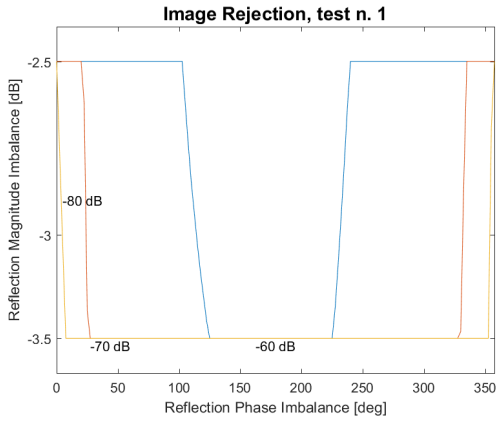

(a) Test 1, scenario 4.

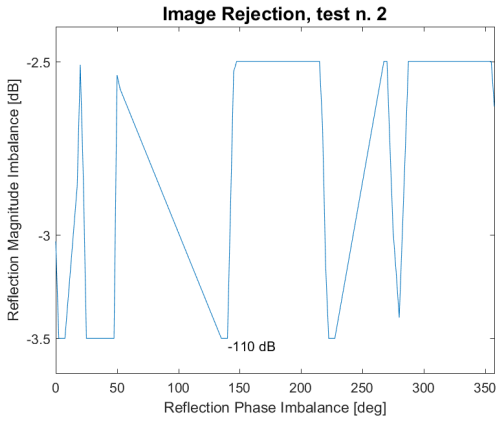

(b) Test 2, scenario 4.

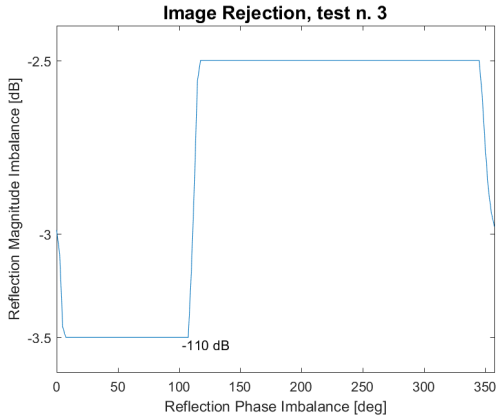

(c) Test 3, scenario 4.

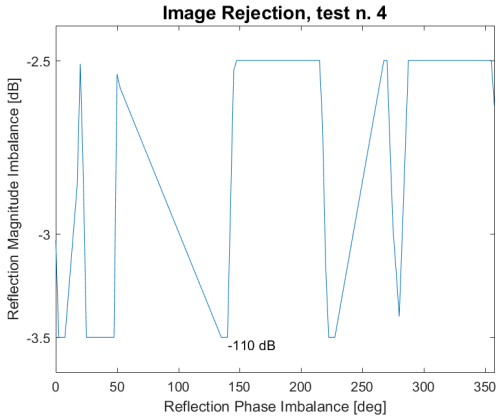

(d) Test 4, scenario 4.

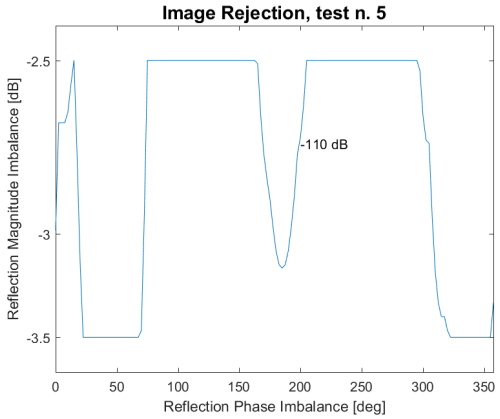

(e) Test 5, scenario 4.

Figure B.4: STV OMT cross-polarization test results using $\Gamma_{fixed} = -3$ dB and $\Gamma_{variable} \in [-3.5, 2.5]$ dB, $\forall\phi$.

Appendix C

Response of reflection losses to manufacturing errors: Planar Version OMT

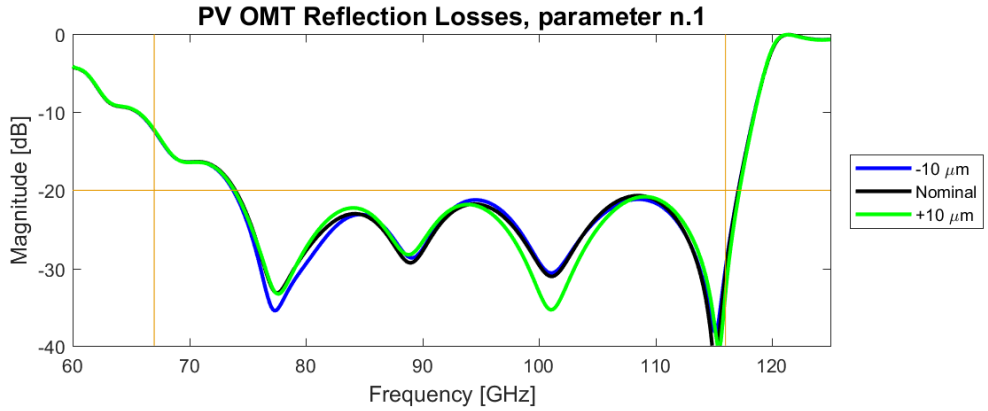

Figure C.1: Response of reflection losses to manufacturing errors. Parameter 1 of the PV OMT - Length of the outer engravement on the microstrip probe.

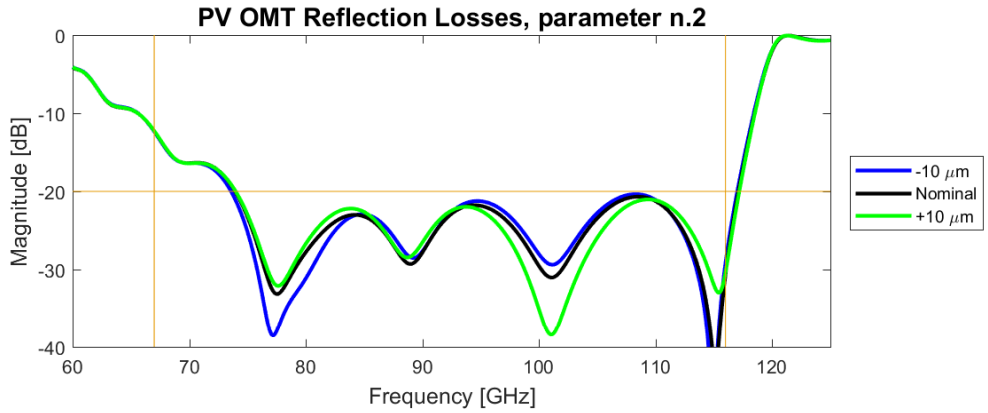

Figure C.2: Response of reflection losses to manufacturing errors. Parameter 2 of the PV OMT - Length of the middle engravement on the microstrip probe.

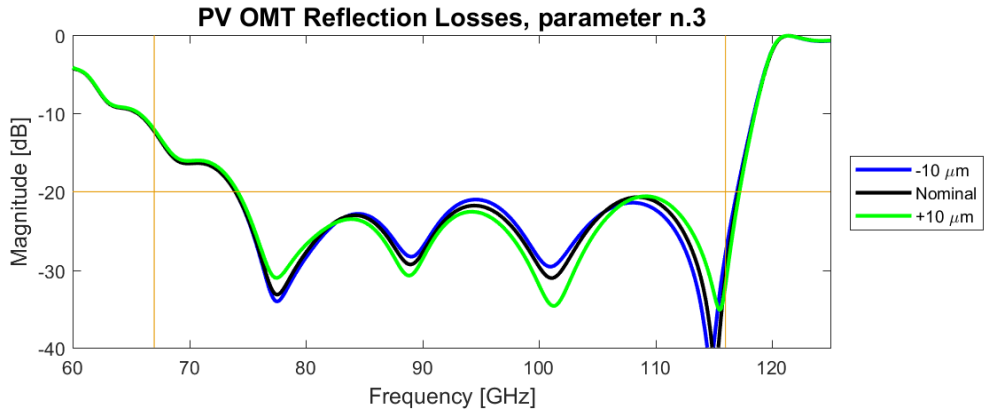

Figure C.3: Response of reflection losses to manufacturing errors. Parameter 3 of the PV OMT - Length of the inner engravement on the microstrip probe.

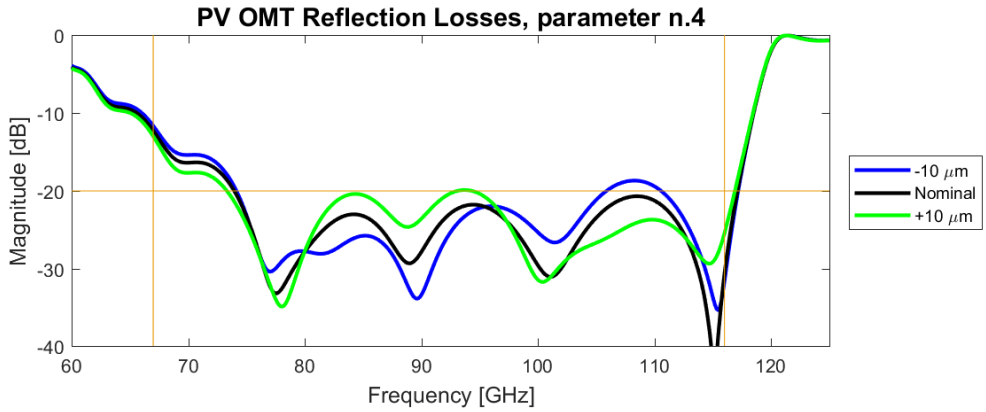

Figure C.4: Response of reflection losses to manufacturing errors. Parameter 4 of the PV OMT - Width of the first microstrip impedance matching section step.

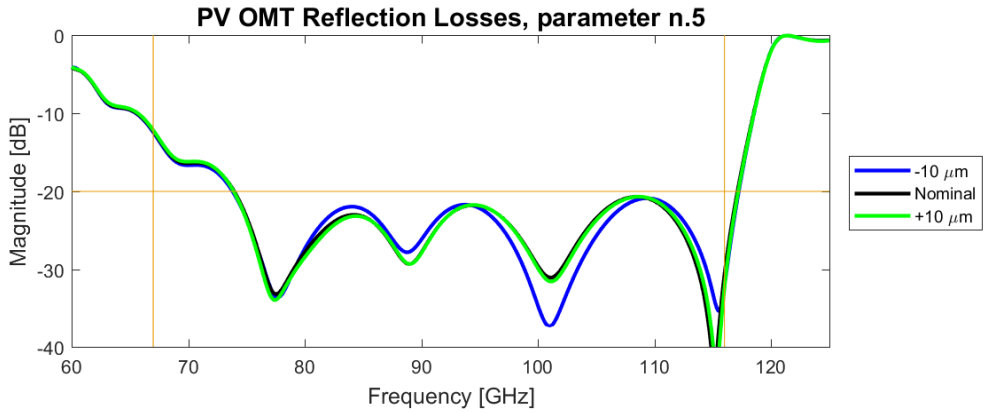

Figure C.5: Response of reflection losses to manufacturing errors. Parameter 5 of the PV OMT - Length of the first microstrip impedance matching section step.

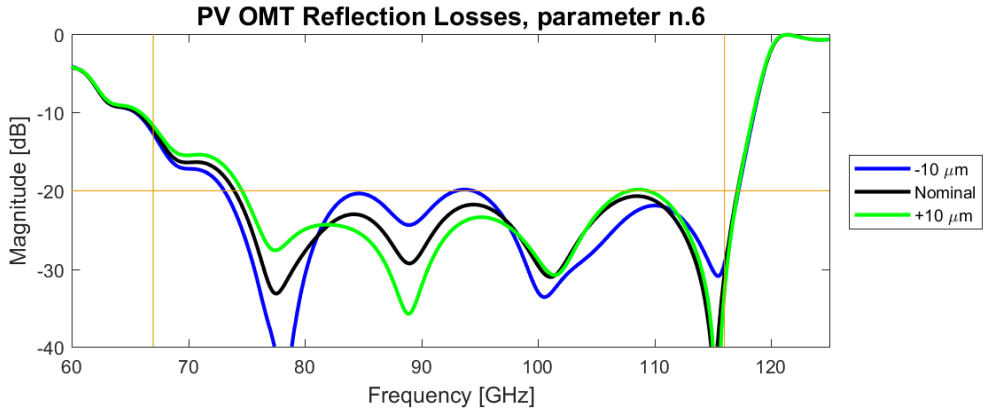

Figure C.6: Response of reflection losses to manufacturing errors. Parameter 6 of the PV OMT - Width of the second microstrip impedance matching section step.

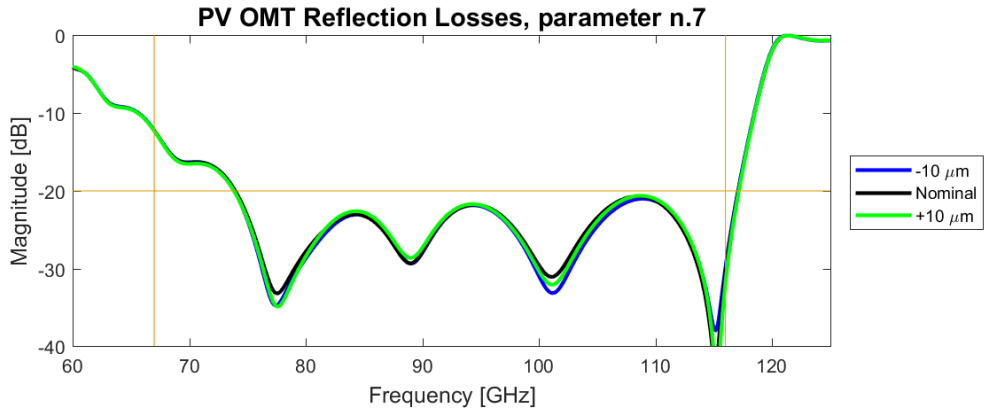

Figure C.7: Response of reflection losses to manufacturing errors. Parameter 7 of the PV OMT - Length of the second microstrip impedance matching section step.

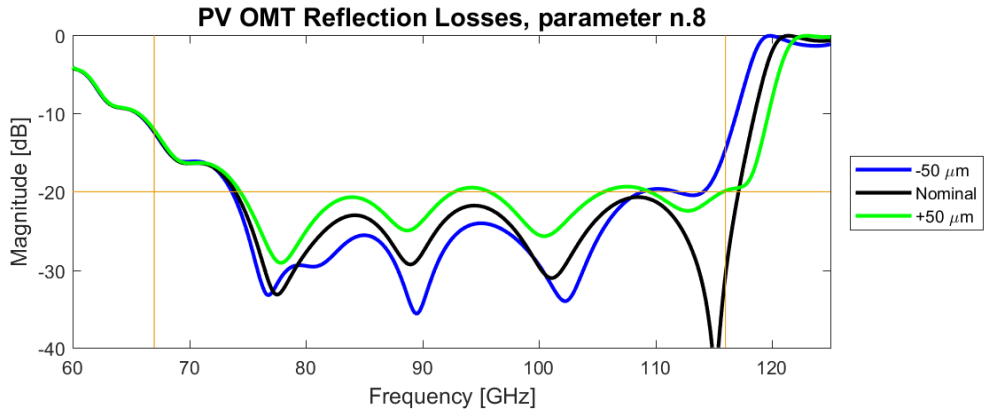

Figure C.8: Response of reflection losses to manufacturing errors. Parameter 8 of the PV OMT - Radius of the tuning stub.

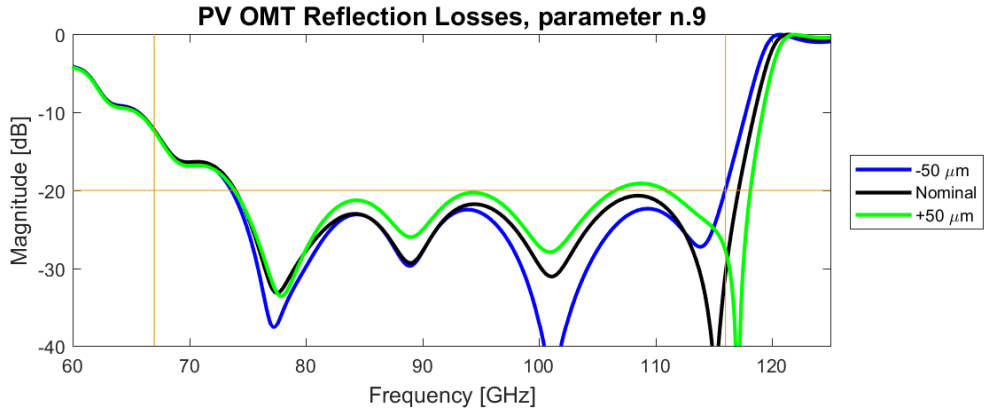

Figure C.9: Response of reflection losses to manufacturing errors. Parameter 9 of the PV OMT - Height of the tuning stub.

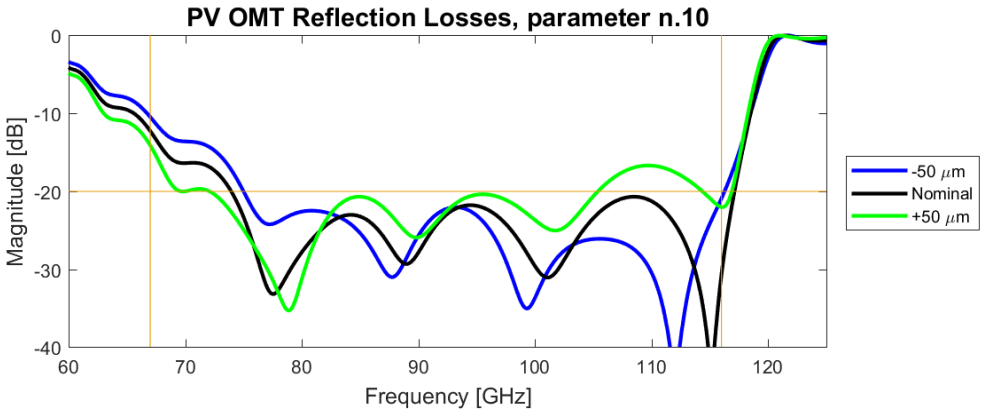

Figure C.10: Response of reflection losses to manufacturing errors. Parameter 10 of the PV OMT - Height of the air backshort.

Appendix D

Response of reflection losses to manufacturing errors: Planar Version LO Splitter

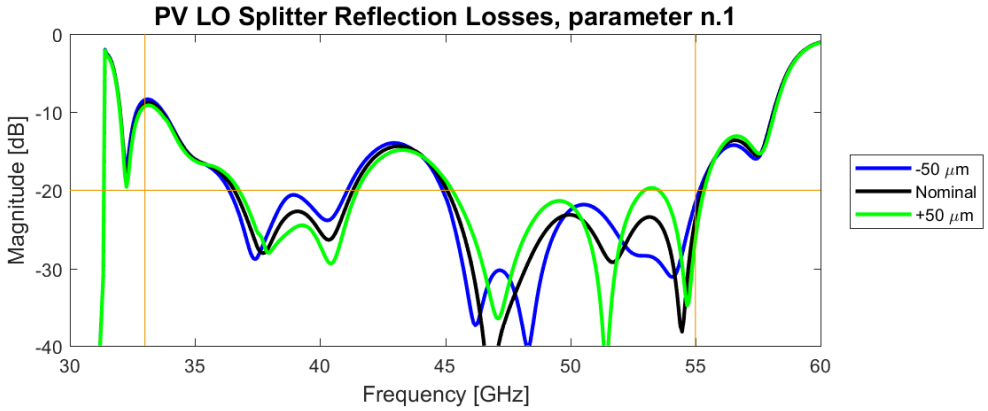

Figure D.1: Response of reflection losses to manufacturing errors. Parameter 1 of the PV LO Splitter - Height of the air backshort.

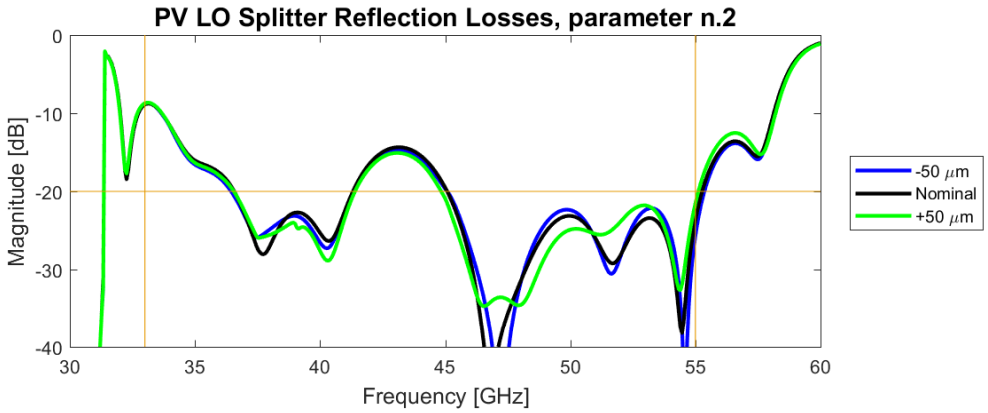

Figure D.2: Response of reflection losses to manufacturing errors. Parameter 2 of the PV LO Splitter - Depth of the first bend step.

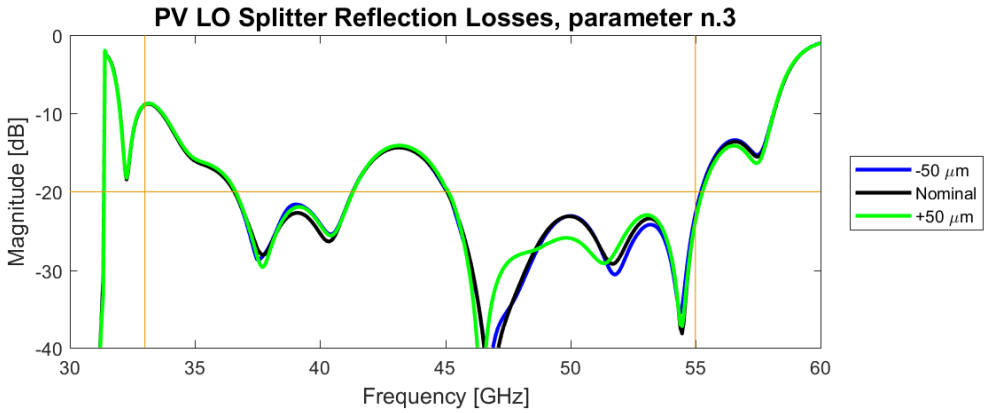

Figure D.3: Response of reflection losses to manufacturing errors. Parameter 3 of the PV LO Splitter - Depth of the second bend step.

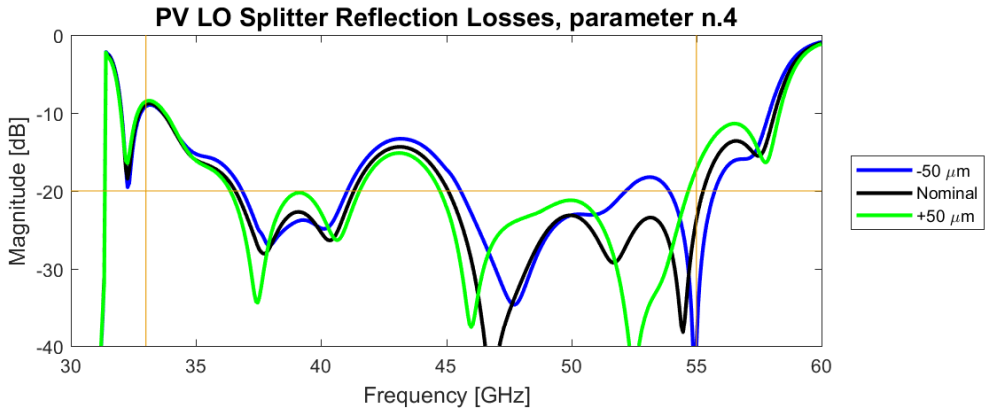

Figure D.4: Response of reflection losses to manufacturing errors. Parameter 4 of the PV LO Splitter - Height of the tuning stub.

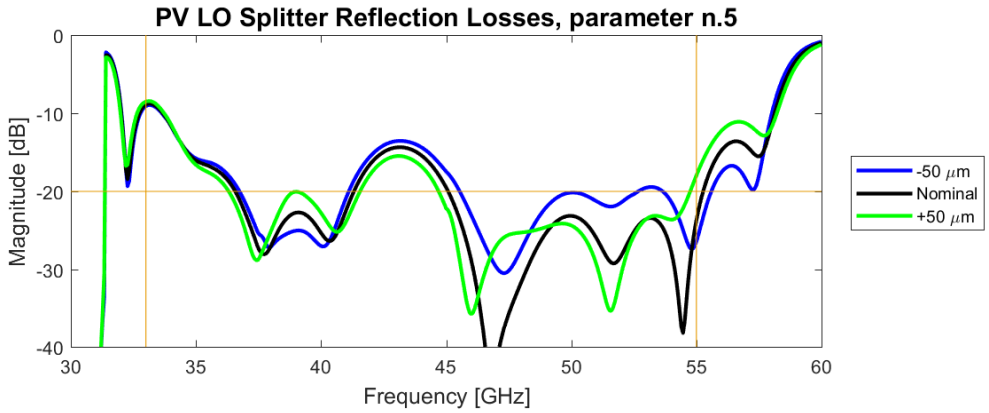

Figure D.5: Response of reflection losses to manufacturing errors. Parameter 5 of the PV LO Splitter - Radius of the tuning stub.

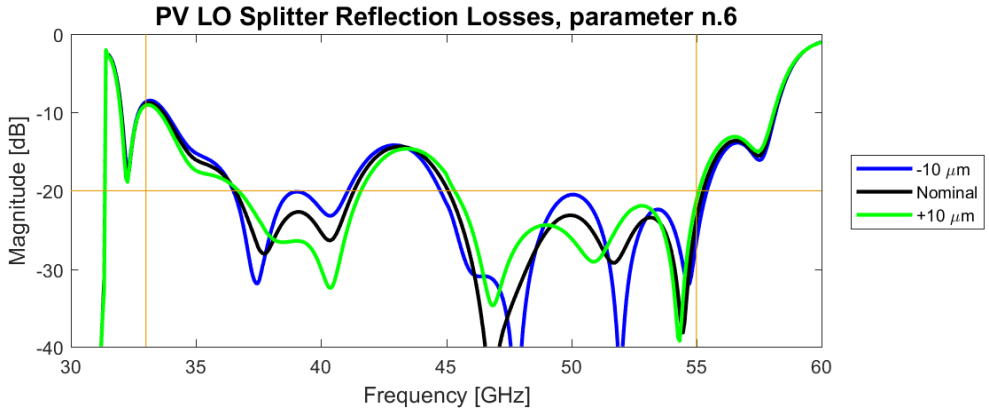

Figure D.6: Response of reflection losses to manufacturing errors. Parameter 6 of the PV LO Splitter - Width of the first microstrip impedance matching section step.

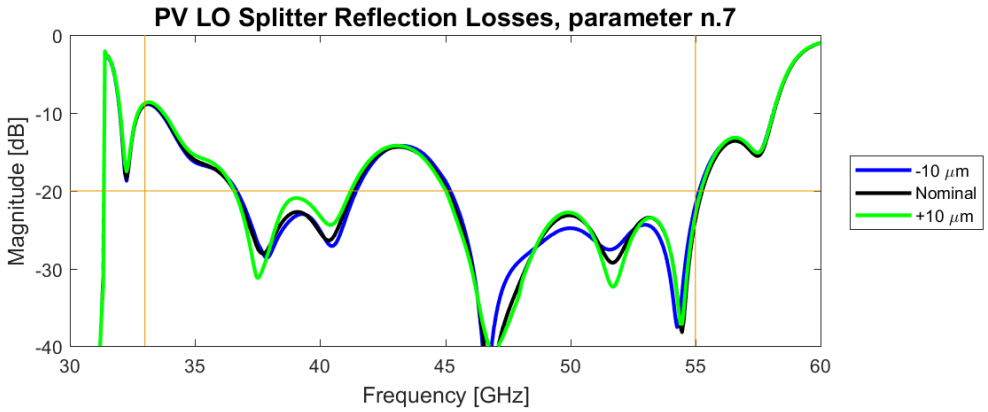

Figure D.7: Response of reflection losses to manufacturing errors. Parameter 7 of the PV LO Splitter - Length of the first microstrip impedance matching section step.

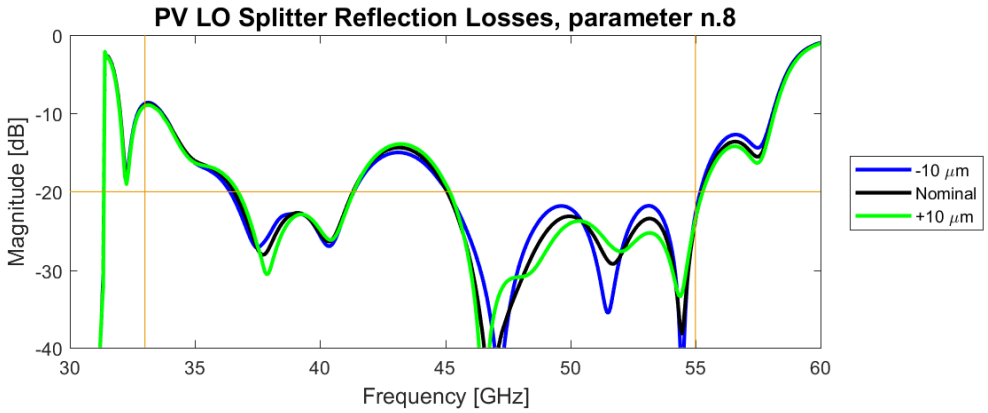

Figure D.8: Response of reflection losses to manufacturing errors. Parameter 8 of the PV LO Splitter - Width of the second microstrip impedance matching section step.

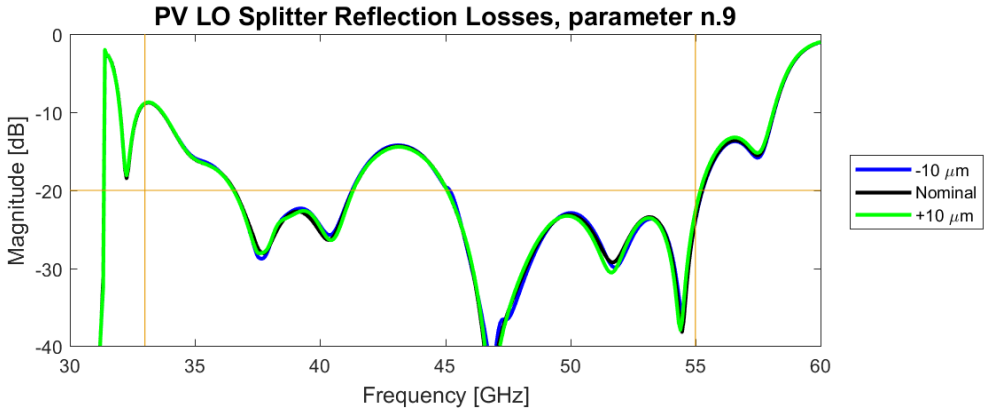

Figure D.9: Response of reflection losses to manufacturing errors. Parameter 9 of the PV LO Splitter - Length of the second microstrip impedance matching section step.

Appendix E

Response of reflection losses to manufacturing errors: Semi Turnstile Version OMT

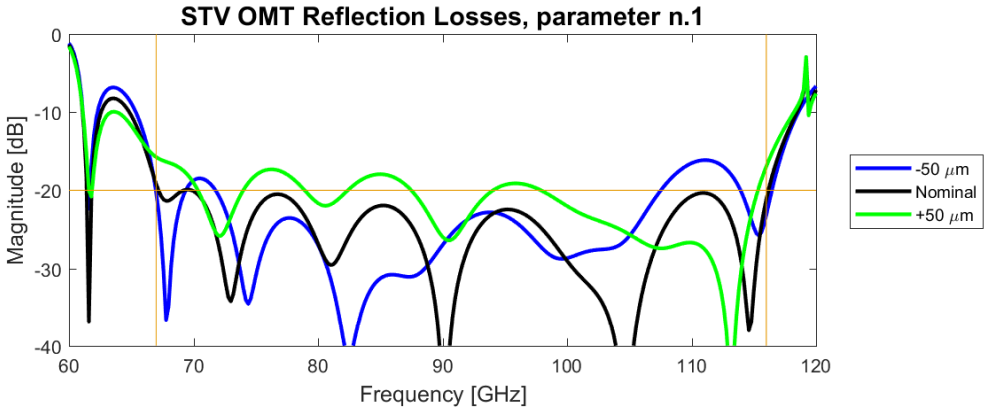

Figure E.1: Response of reflection losses to manufacturing errors. Parameter 1 of the STV OMT - Height of the air backshort.

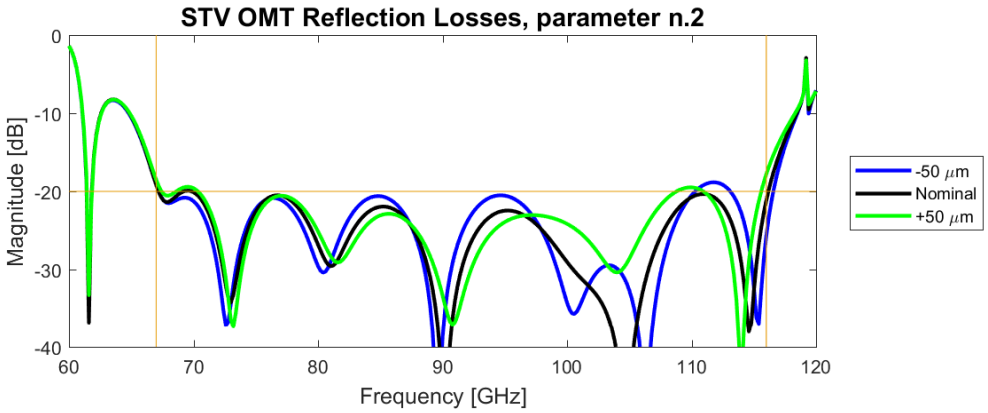

Figure E.2: Response of reflection losses to manufacturing errors. Parameter 2 of the STV OMT - Radius of the inner tuning stub.

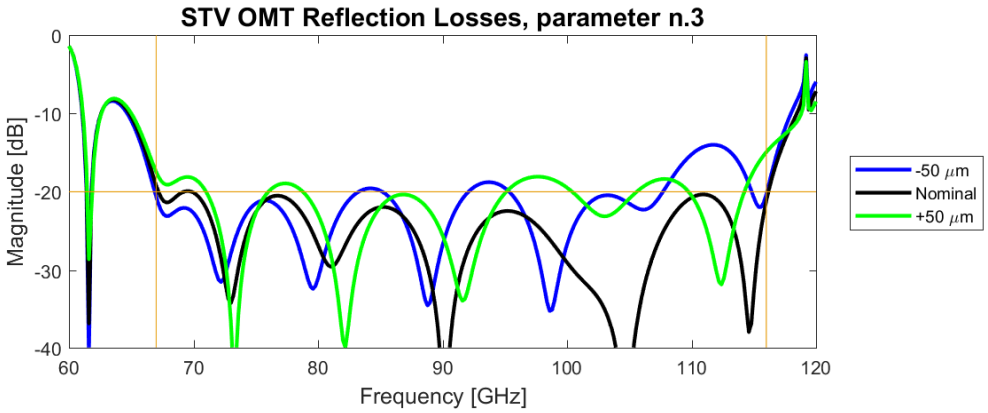

Figure E.3: Response of reflection losses to manufacturing errors. Parameter 3 of the STV OMT - Height of the inner tuning stub.

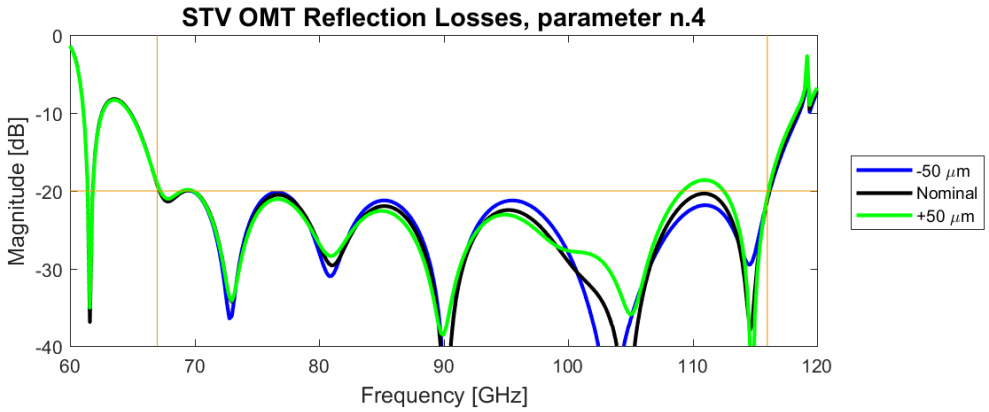

Figure E.4: Response of reflection losses to manufacturing errors. Parameter 4 of the STV OMT - Radius of the outer tuning stub.

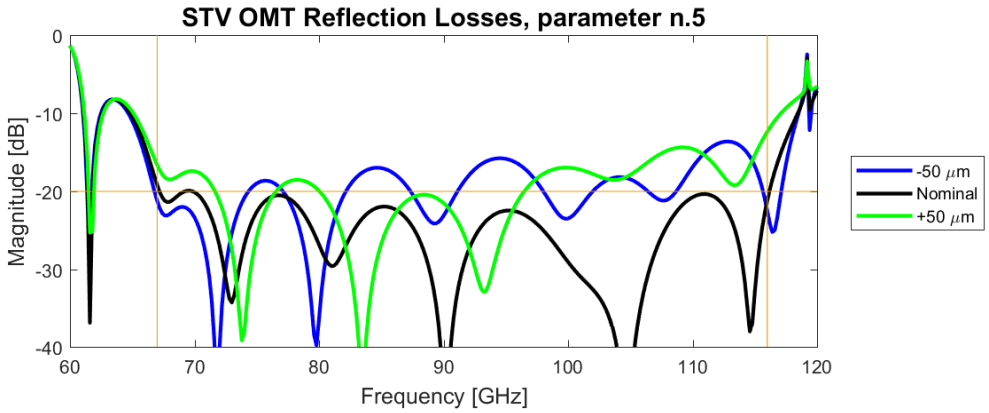

Figure E.5: Response of reflection losses to manufacturing errors. Parameter 5 of the STV OMT - Height of the outer tuning stub.

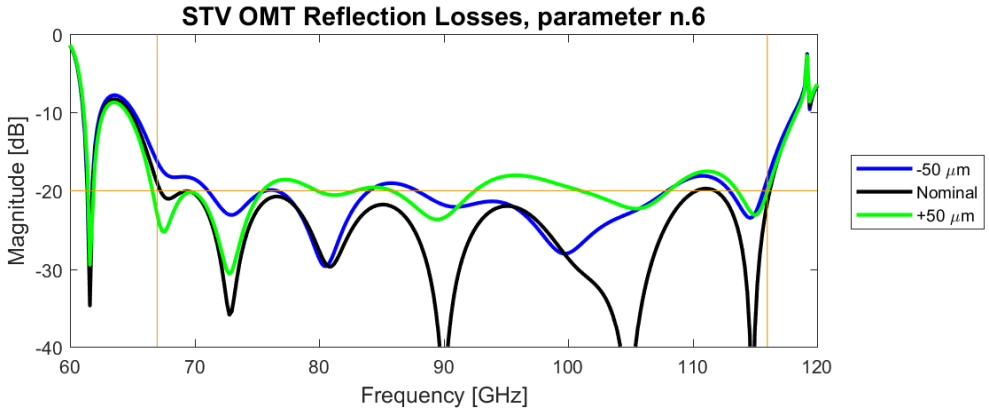

Figure E.6: Response of reflection losses to manufacturing errors. Parameter 6 of the STV OMT - Depth of the first step from the staggered waveguide section.

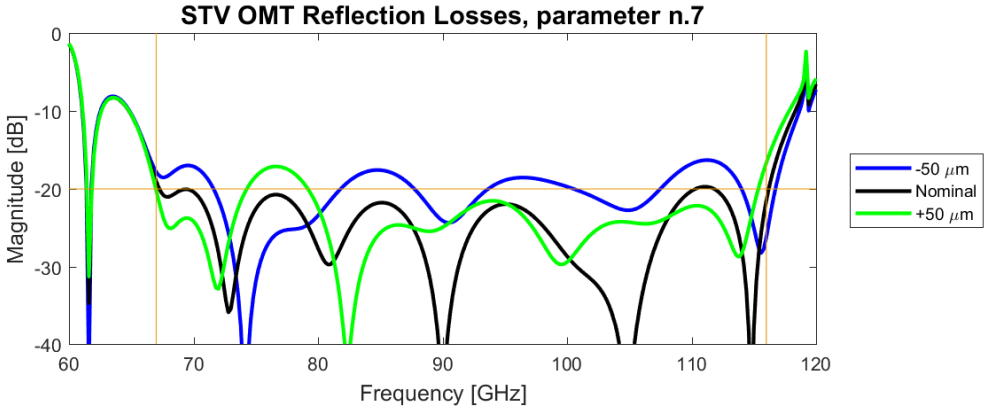

Figure E.7: Response of reflection losses to manufacturing errors. Parameter 7 of the STV OMT - Depth of the second step from the staggered waveguide section.

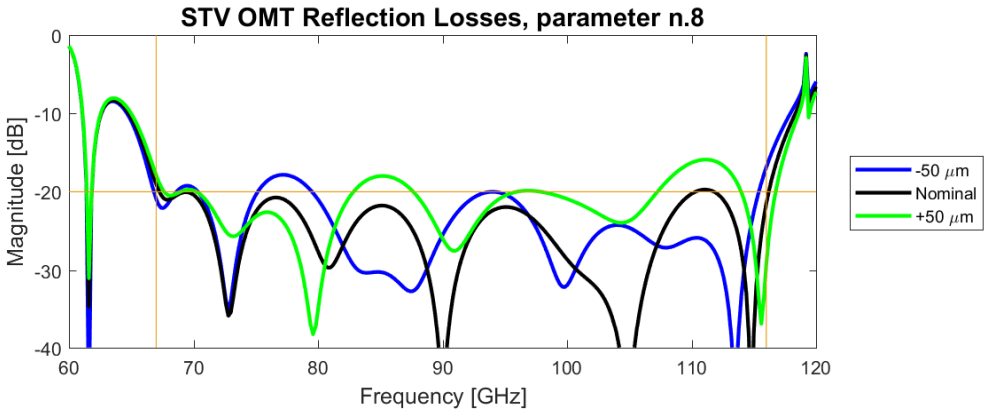

Figure E.8: Response of reflection losses to manufacturing errors. Parameter 8 of the STV OMT -Depth of the third step from the staggered waveguide section.

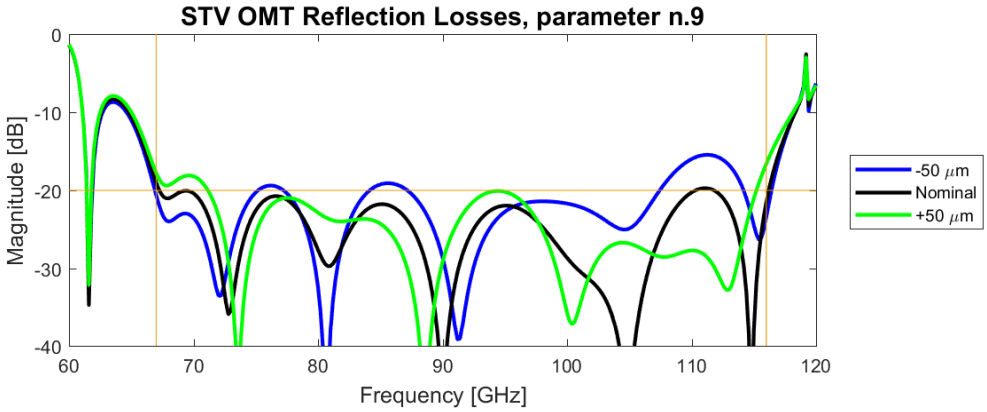

Figure E.9: Response of reflection losses to manufacturing errors. Parameter 9 of the STV OMT - Depth of the fourth step from the staggered waveguide section.

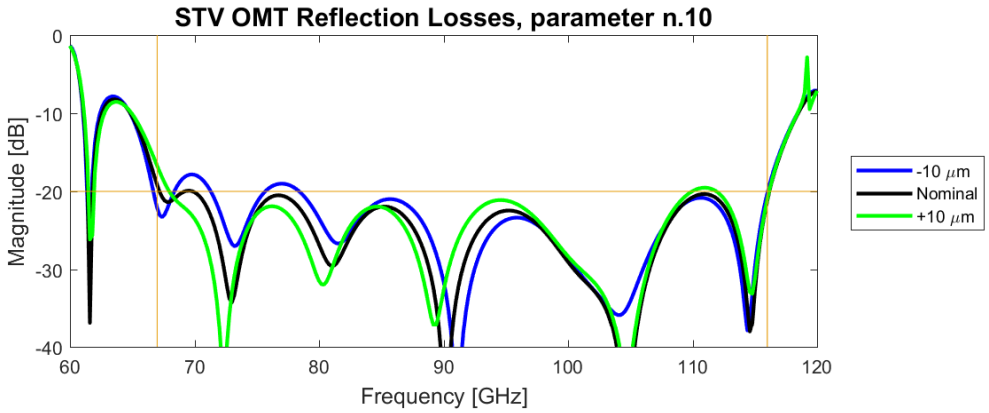

Figure E.10: Response of reflection losses to manufacturing errors. Parameter 10 of the STV OMT - Length of the outer branches from the dendritic microstrip probe.

Appendix F

Response of reflection losses to manufacturing errors: Semi Turnstile Version LO Splitter

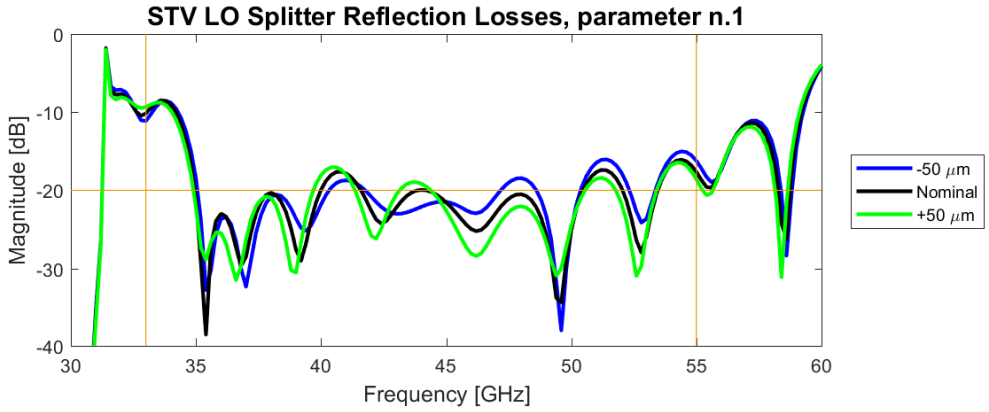

Figure F.1: Response of reflection losses to manufacturing errors. Parameter 1 of the STV LO Splitter - Height of the air backshort.

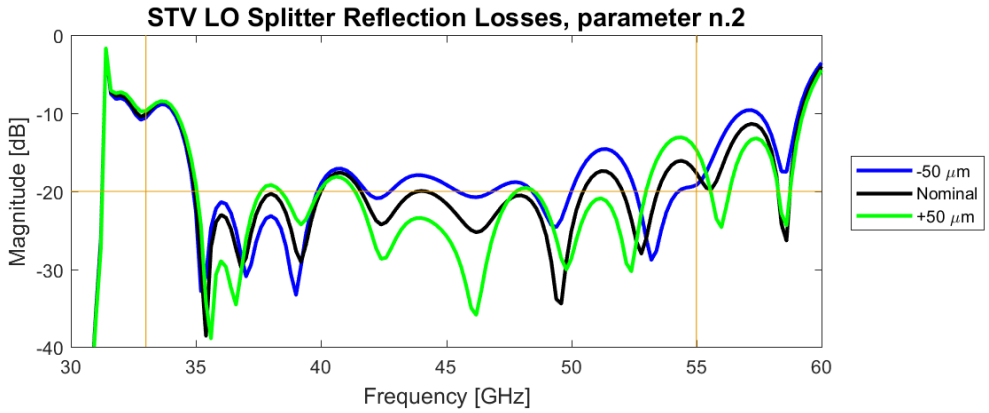

Figure F.2: Response of reflection losses to manufacturing errors. Parameter 2 of the STV LO Splitter - Height of the outer tuning stub.

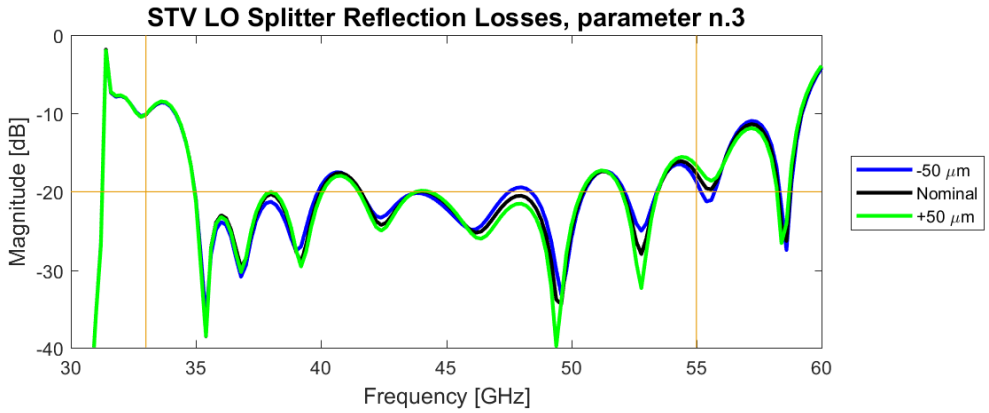

Figure F.3: Response of reflection losses to manufacturing errors. Parameter 3 of the STV LO Splitter - Radius of the outer tuning stub.

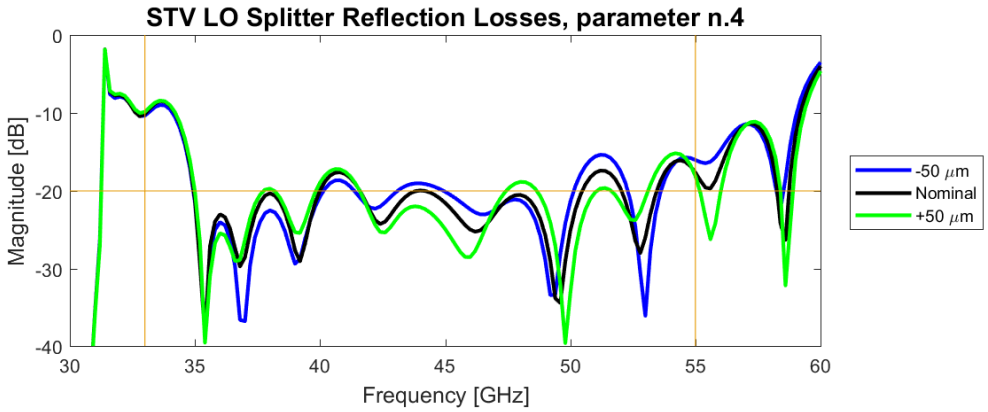

Figure F.4: Response of reflection losses to manufacturing errors. Parameter 4 of the STV OMT - Height of the inner tuning stub.

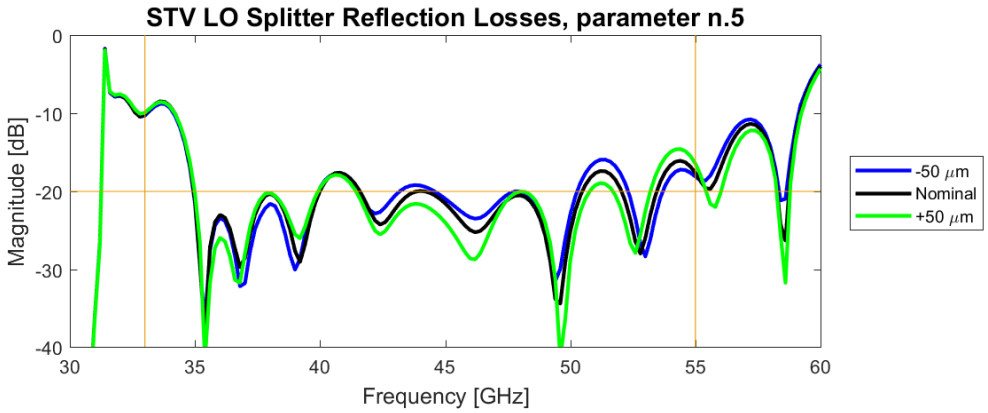

Figure F.5: Response of reflection losses to manufacturing errors. Parameter 5 of the STV LO Splitter - Radius of the inner tuning stub.

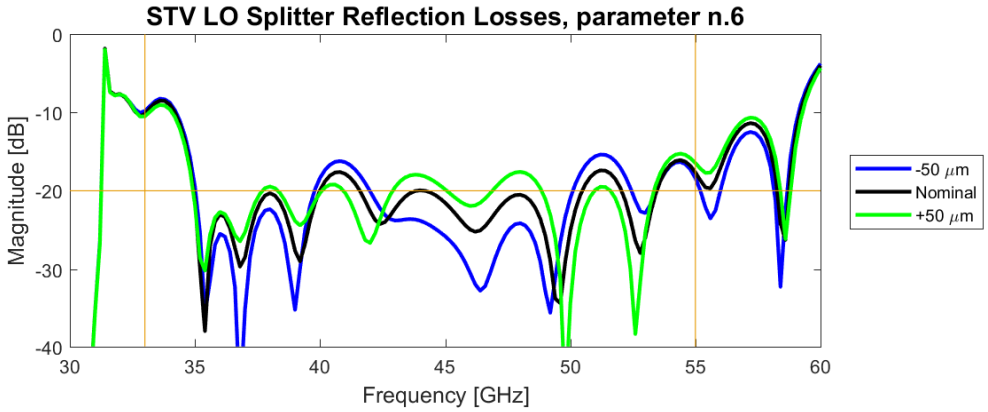

Figure F.6: Response of reflection losses to manufacturing errors. Parameter 6 of the STV LO Splitter - Depth of the first step from the staggered waveguide section.

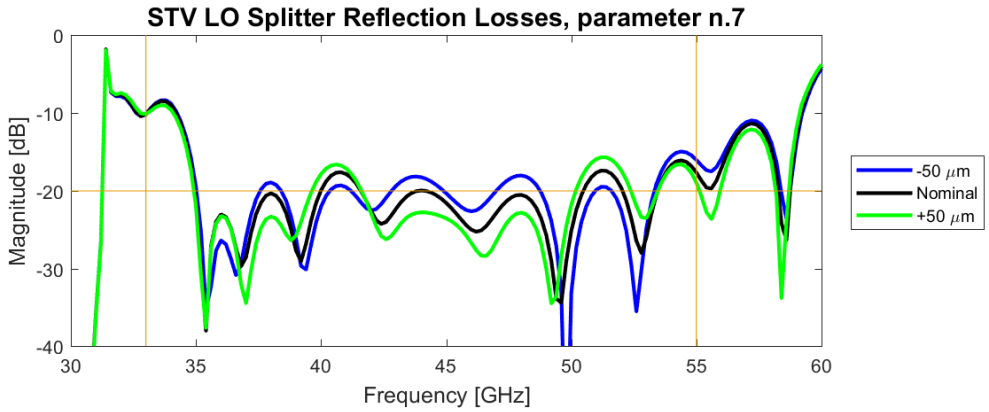

Figure F.7: Response of reflection losses to manufacturing errors. Parameter 7 of the STV LO Splitter - Depth of the second step from the staggered waveguide section.

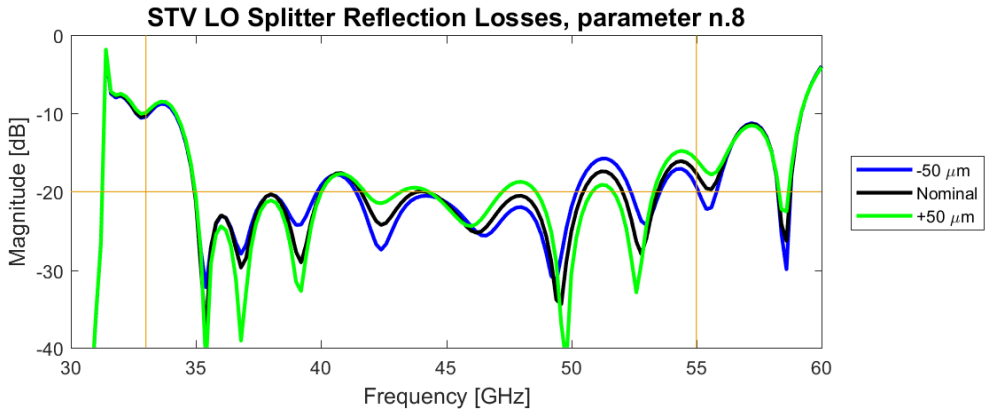

Figure F.8: Response of reflection losses to manufacturing errors. Parameter 8 of the STV LO Splitter -Depth of the third step from the staggered waveguide section.

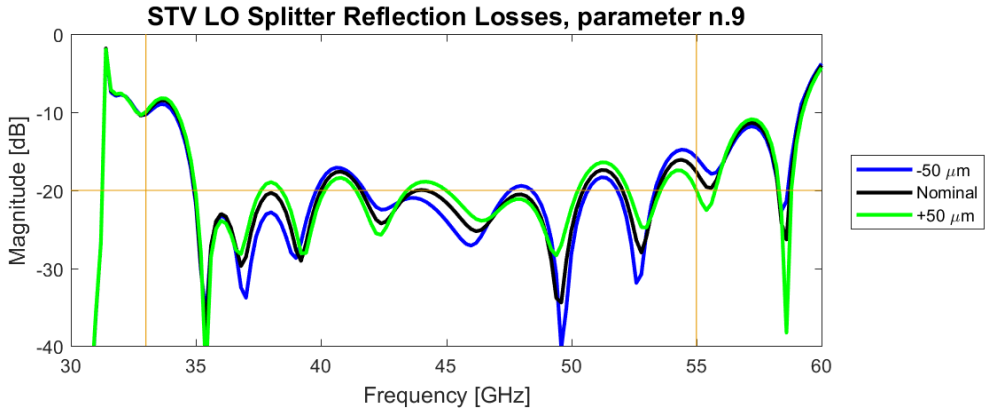

Figure F.9: Response of reflection losses to manufacturing errors. Parameter 9 of the STV LO Splitter - Depth of the fourth step from the staggered waveguide section.

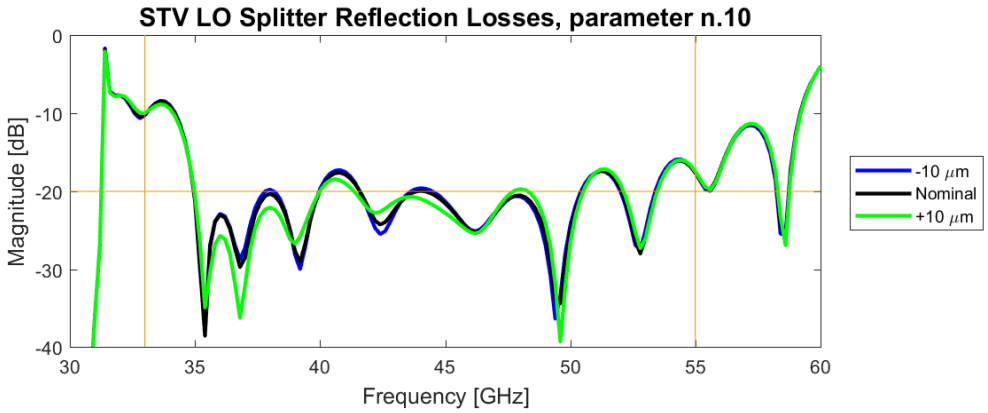

Figure F.10: Response of reflection losses to manufacturing errors. Parameter 10 of the STV LO Splitter - Length of the outer branches from the dendritic microstrip probe.

Appendix G

Figures of current distribution on microstrip probes

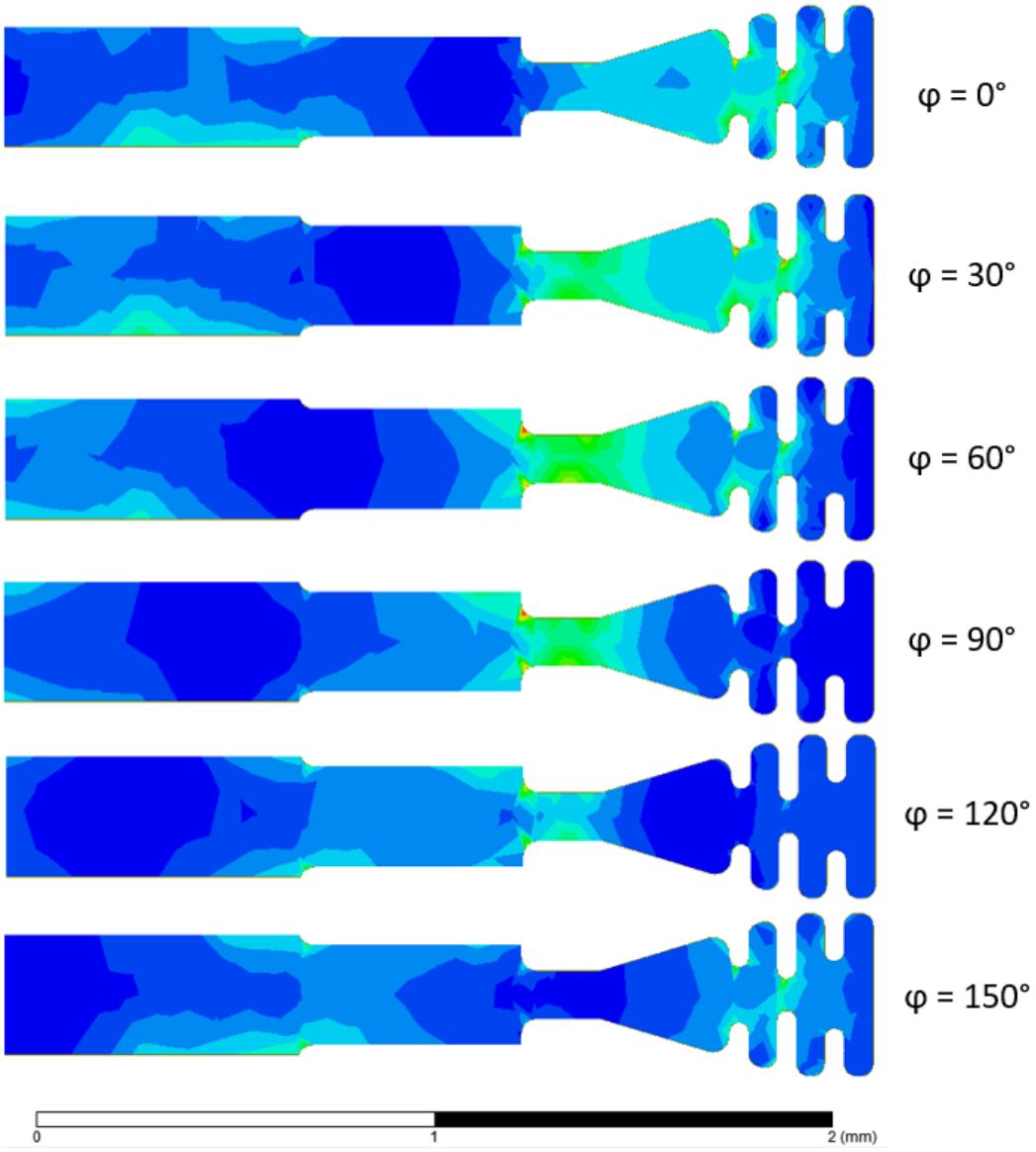

Figure G.1: Current distribution on PV OMT probe at 67 GHz.

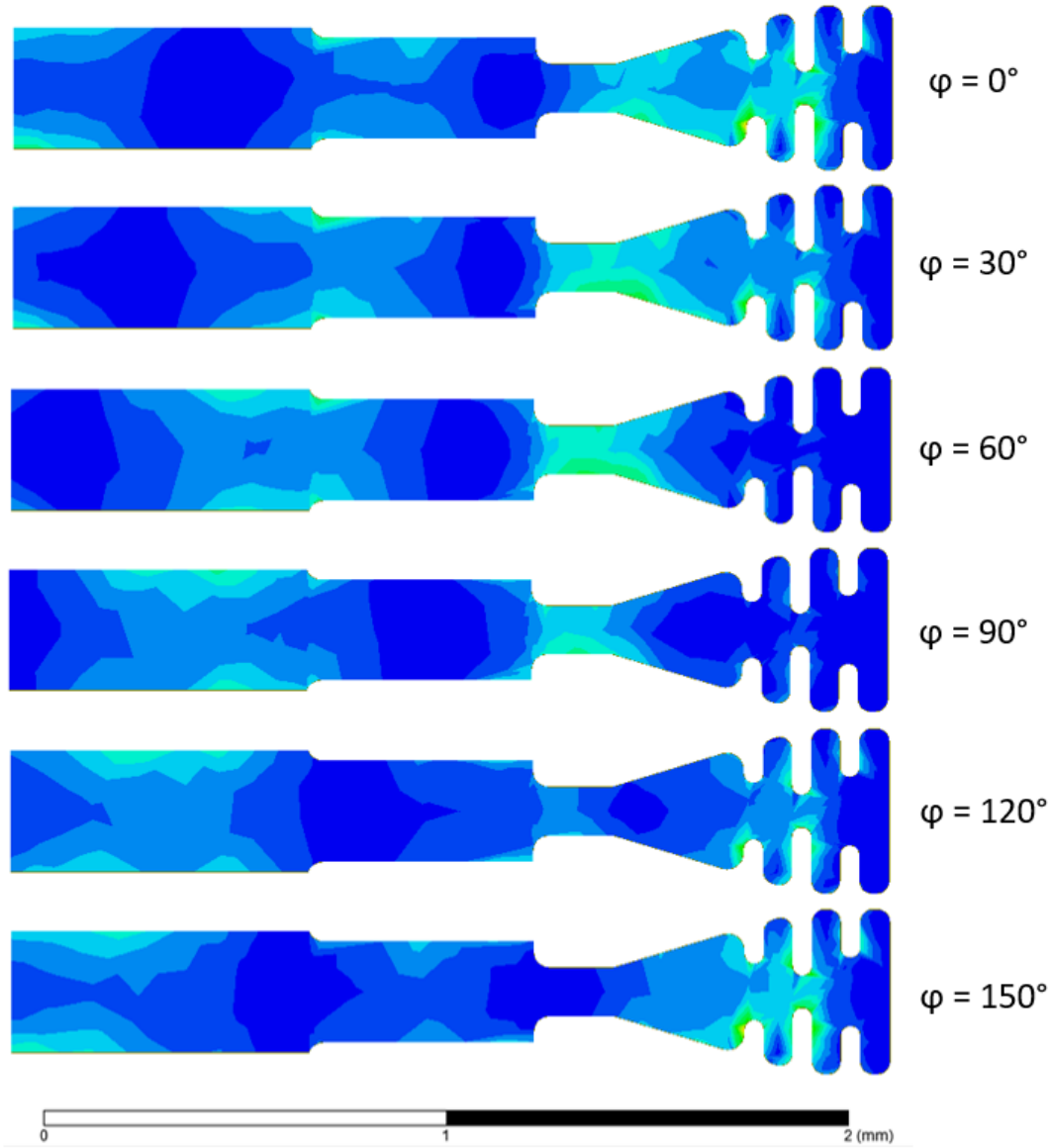

Figure G.2: Current distribution on PV OMT probe at 116 GHz.

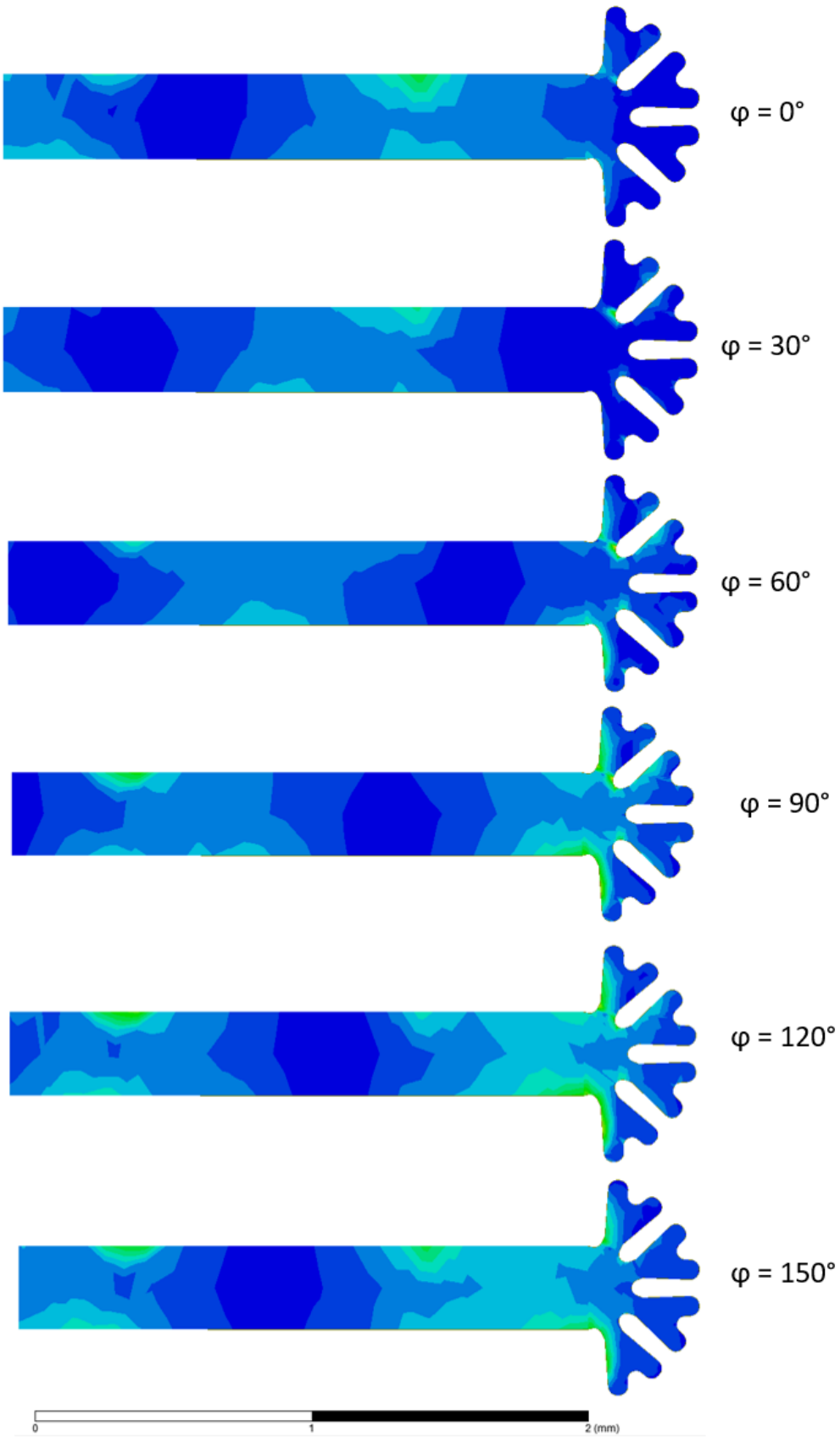

Figure G.3: Current distribution on STV OMT probe at 67 GHz.

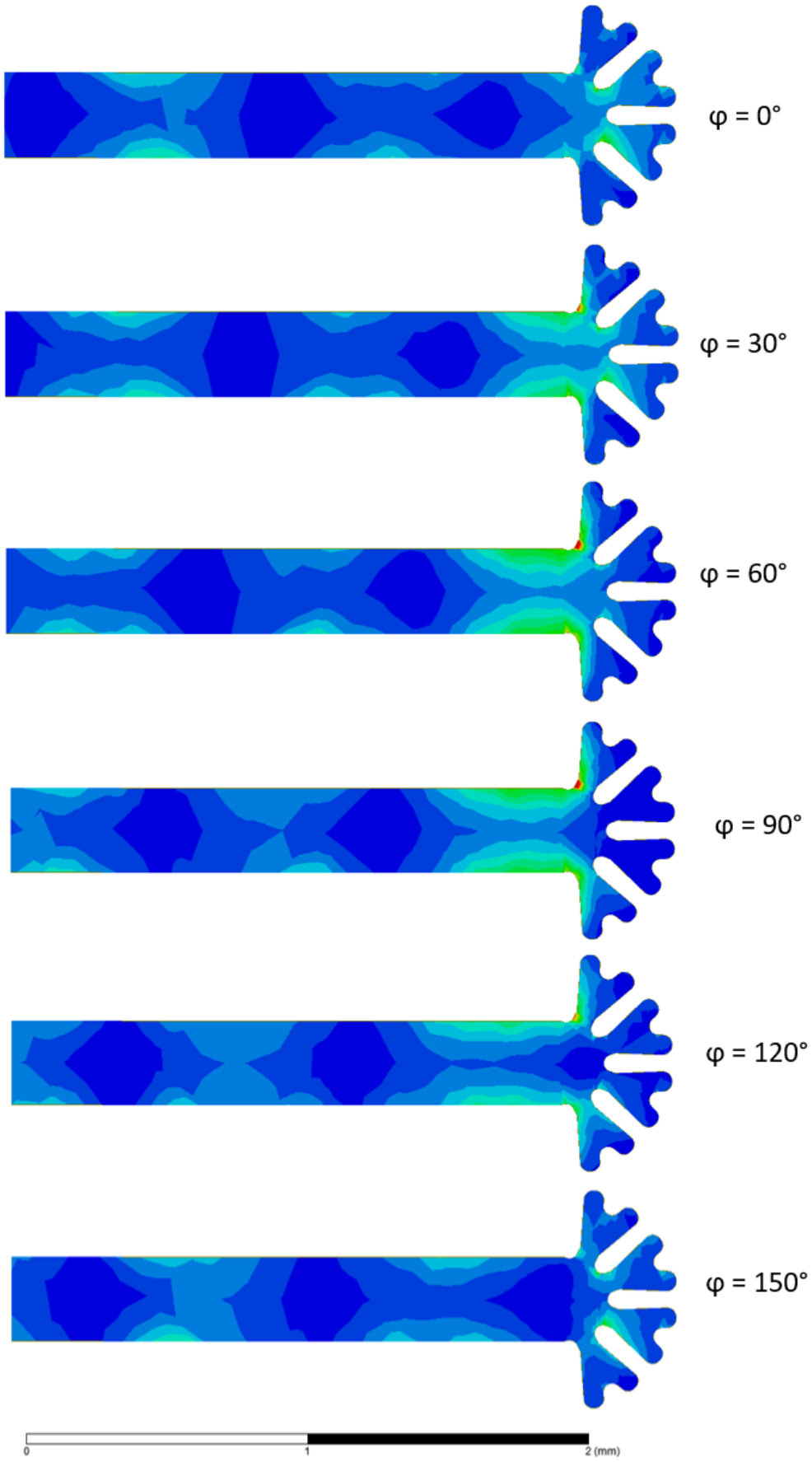

Figure G.4: Current distribution on STV OMT probe at 116 GHz.

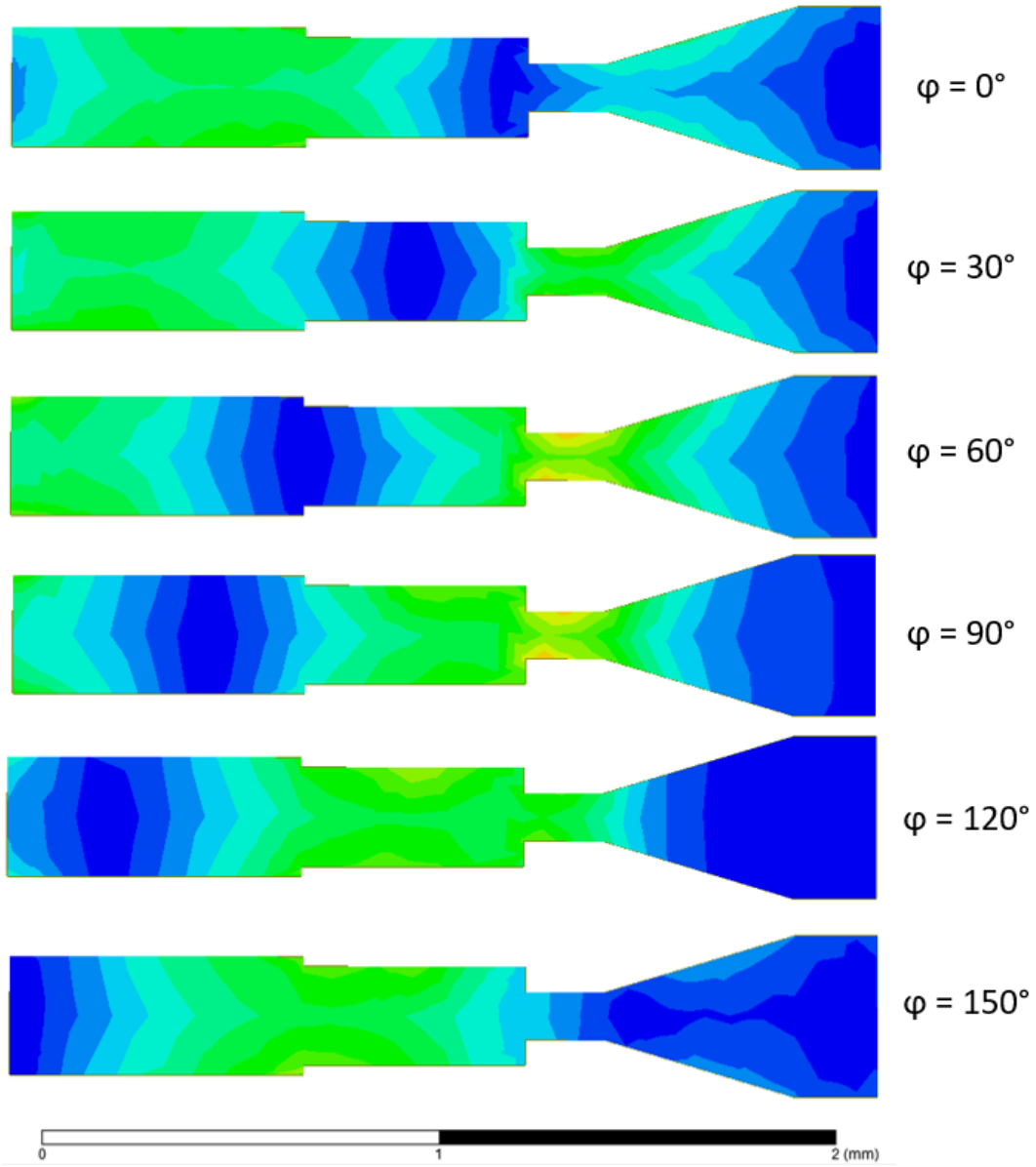

Figure G.5: Current distribution on PV OMT probe without slits at 67 GHz.

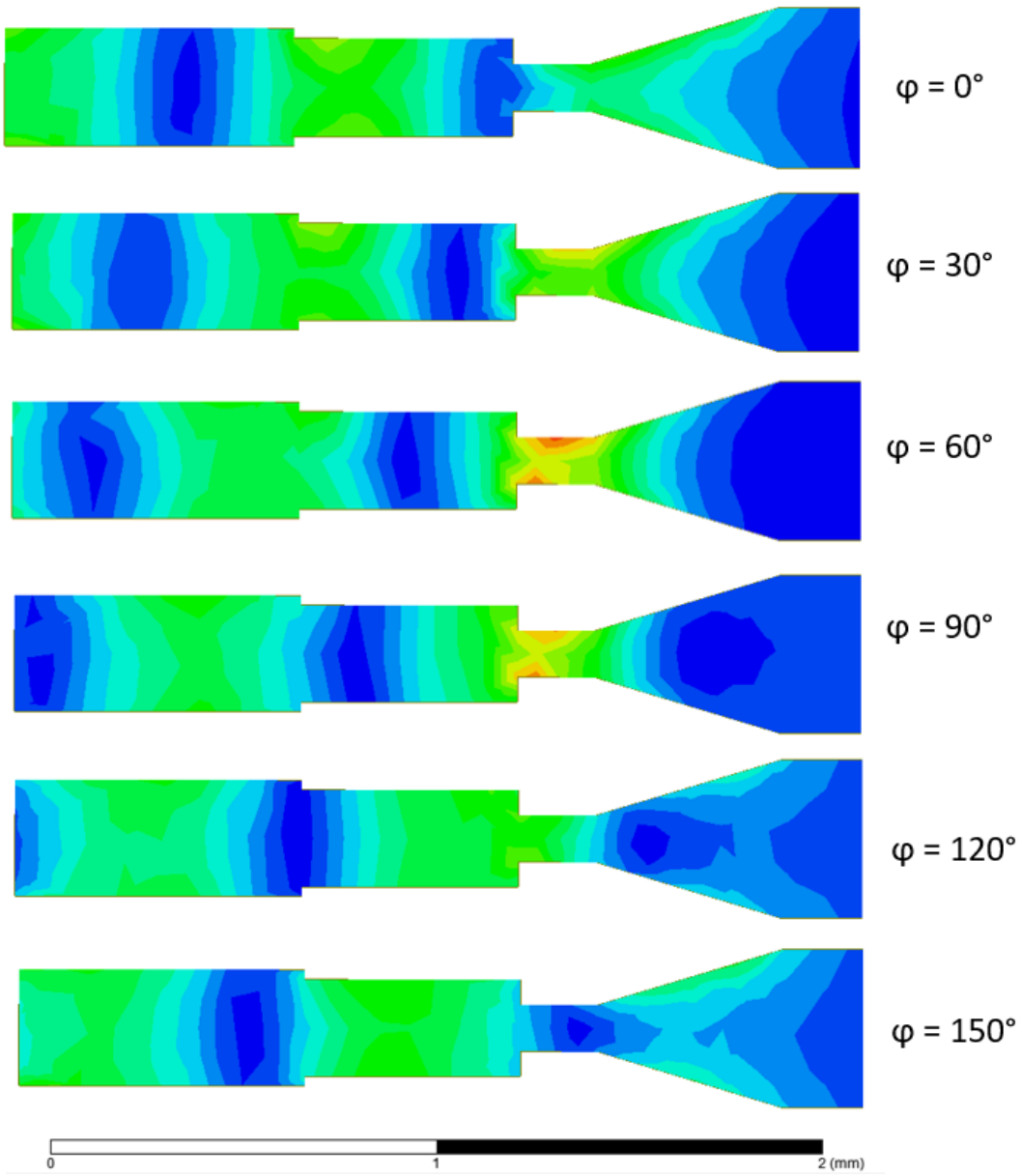

Figure G.6: Current distribution on PV OMT probe without slits at 116 GHz.